

# Relating Metal Binding to DNA Binding in the Nickel Regulatory Protein NikR

by

Christine M Phillips

A.B. Chemistry and Mathematics (2004)  
Vassar College, Poughkeepsie, NY

Submitted to the Department of Chemistry in  
Partial Fulfillment of the Requirements for the Degree of

DOCTOR OF PHILOSOPHY  
in Biological Chemistry

at the

Massachusetts Institute of Technology  
June 2010

© 2010 Massachusetts Institute of Technology. All rights reserved

Signature of Author \_\_\_\_\_  
Department of Chemistry  
February 18, 2010

Certified by \_\_\_\_\_  
Catherine L. Drennan  
Professor of Chemistry and Biology  
Howard Hughes Medical Institute Investigator and Professor  
Thesis Supervisor

Certified by \_\_\_\_\_  
Collin M. Stultz  
Associate Professor of Electrical Engineering and Computer Science  
and Health Sciences Technology  
Thesis Supervisor

Accepted by \_\_\_\_\_  
Robert W. Field  
Chairman, Department Committee on Graduate Studies

This doctoral thesis has been examined by a Committee of the Department of Chemistry as follows:

Professor Barbara Imperiali \_\_\_\_\_  
Committee Chairman  
Class of 1922 Professor of Chemistry and Biology

Professor Catherine L. Drennan \_\_\_\_\_  
Research Supervisor  
Professor of Chemistry and Biology  
Howard Hughes Medical Institute Investigator and Professor

Professor Collin M. Stultz \_\_\_\_\_  
Research Supervisor  
Associate Professor of Electrical Engineering and Computer Science  
and Health Sciences Technology

Professor Thomas U. Schwartz \_\_\_\_\_  
Committee Member  
Pfizer-Laubach Career Development Professor of Biology

# Relating Metal Binding to DNA Binding in the Nickel Regulatory Protein NikR

Christine M. Phillips

Submitted to the Department of Chemistry in January 2010  
In Partial Fulfillment of the Requirements for the Degree of  
Doctor of Philosophy in Biological Chemistry

## ABSTRACT

The concentration of transition metals within the cell must be tightly regulated. If the concentration of a given transition metal is too low the cell may not be able to perform life-sustaining processes, while high levels of metals are poisonous to the cell and can cause cell death. In *Escherichia coli*, NikR regulates nickel uptake by blocking transcription of the genes encoding the nickel uptake transporter, NikABCDE. NikR is a homotetrameric transcription factor with a central metal binding domain (MBD) that includes the tetrameric interface and two flanking dimeric ribbon-helix-helix (RHH) DNA-binding domains. Early work revealed that NikR can bind a variety of transition metal ions and has two binding affinities for the *nik* operon: nM when stoichiometric  $\text{Ni}^{2+}$  binds NikR and  $\mu\text{M}$  when excess  $\text{Ni}^{2+}$  binds. The enhanced DNA affinity suggests the presence of low affinity nickel binding sites on the protein. Recently, it has been shown that NikR also requires  $\text{K}^+$  to bind DNA, suggesting yet another type of metal binding site on the protein.

To understand NikR's ability to bind multiple transition metal ions and how  $\text{Ni}^{2+}$  specifically induces NikR-DNA binding, we solved the crystal structures of the apo-MBD and BMD bound to  $\text{Zn}^{2+}$  and  $\text{Cu}^{2+}$ . Comparing these structures to the previously published  $\text{Ni}^{2+}$ -MBD structure, we noted that when the proper metal binds to NikR it utilizes H76 of alpha helix 3 as a ligand. This, in turn, orders helix  $\alpha 3$ , and we propose this conformational stabilization is a key step in the NikR-DNA binding mechanism.

Electrostatic free energy calculations and thermodynamic integration were used to study which metal prefers to bind at a site between the MBD and RHH domains that is formed when NikR is bound to DNA. Our studies illustrate that NikR-DNA binding was most favorable when this site contains a monovalent cation the size of  $\text{K}^+$ . These studies support a physiological role of  $\text{K}^+$  in NikR-DNA binding.

Structures from crystals of NikR and NikR-bound to DNA soaked with excess nickel ions indicate six types of potential low-affinity nickel binding sites on the protein surface. Binding of excess nickel ions to these sites does not induce any significant conformational change, suggesting that these sites have an electrostatic effect increasing

NikR's affinity for DNA. Using a combination of X-ray crystallography and molecular simulations we have identified and explored the metal binding sites on *E. coli* NikR and how they influence NikR:DNA binding.

Thesis Supervisor: Catherine L. Drennan

Title: Professor of Chemistry and Biology

Investigator and Professor, Howard Hughes Medical Institute

Thesis Co-supervisor: Collin M. Stultz

Title: Associate Professor of Electrical Engineering and Computer Science

and Health Sciences and Technology

*For my Dad, who always encouraged me to ask how and why.*

## ACKNOWLEDGEMENTS

First, I'd like to thank my thesis committee, my chair Barbara Imperiali and member Thomas Schwartz, for their advice and support along the way. Thanking my two thesis advisors, Cathy and Collin, in just a few sentences seems insufficient, but I'll do my best.

Before I applied to graduate schools I knew I wanted to learn crystallography and I was fortunate that my undergraduate advisor at Vassar knew of a pretty good protein crystallographer, Cathy Drennan. Cathy had worked with my undergraduate advisor, Miriam Rossi, when she was at Vassar. Entering the biochemistry PhD program at MIT with no biochemistry or biology background I definitely felt like I was in way over my head. Though I doubted myself, Cathy never did. Even as I discussed the possibility of leaving graduate school when I felt overwhelmed with orals or cumes, she never even hinted that she thought that would be a good idea. Her faith in my abilities as a scientist and a teacher helped me through the roughest patches of graduate school.

In my third year, following a discussion of project ideas and plans, Cathy and I approached Collin about having me spend some time in his lab addressing some questions of the NikR system using a more theoretical approach. Collin didn't hesitate to invite me into his lab, later citing that he had enjoyed my presentations at joint group meetings and thought I would be a good fit. Learning a completely new set of techniques and skills in my 3<sup>rd</sup> year of graduate school wasn't easy, but Collin was a fantastic teacher and took multiple hours out of each week to sit with me and go over everything from electrostatic potentials to writing a specific piece of code. Though we have gone through some more difficult patches over the past few years, I'm certain I made the right choice—and was lucky to be able to make the choice—to join his lab. I will be forever grateful for Collin's unwavering support as an advisor, and I'm sure I will be calling upon him for advice for years to come.

I have to thank all of my lab members—from both the Drennan and Stultz labs—for their encouragement, good humor, and shared woes. To start at the beginning, thanks to Hector for showing me around the Drennan lab and mentoring me in the lab in the summer of 2004. To Eric, who set the basis for the NikR work, taught me how to do a protein prep, collected a number of the datasets discussed in this thesis, and who has always found time to discuss my science even as he was beginning his faculty position. Jess, for her mentoring on the X-rays, both at home and at SSRL, and for taking the time (and having the patience) to help me process my first dataset. The computer gurus—Paul and Danny—for their positive attitude even when responding to a “computer emergency” phone call early on a weekend morning. Ainsley's support in everything from science to softball and his realistic, but positive attitude always had a way of convincing me things would be okay. Thanks to Sarah her friendship and being my first pottery buddy. For inspiring all of us in lab that science can work—thanks to Kaity for the upbeat attitude regardless of the countless hours she had spent in lab. To Cintyu, who, though much quieter than many other lab members, never failed to lend a helping hand when needed or partake in the crazy fun, especially of post-synchrotron runs. Laura, who joined the Drennan lab at the same time as me,

was a fantastic resource for snide comments and dry humor, a great friend, and a continuous source of calm.

In addition to being the first Christina I've ever really liked, Christina has been a fantastic labmate—while I'm awed by her knowledge and enthusiasm in lab, she has also made me feel useful and knowledgeable. Thanks to Peter, for his daily positive attitude, always providing a laugh, and for putting up with my harassment. Jeremy, for taking over responsibilities as Merohedral Twins captain and helping me make a fire. Marcus willingly took over the NiKR project and my mentoring responsibilities in perfect timing to allow me to graduate when I did and has been a great in-lab inorganic reference. For allowing me to pick their brains, listen to my many seminar practices, and reading manuscripts and grant proposals, not to mention company on many walks to Starbucks, thanks to Mishtu and Nozomi. Thanks to Becky for her assistance in keeping the lab running and taking over the SufR project.

Joining the Stultz lab later during my time at MIT I was worried about fitting into a whole new lab dynamic, but the members of the lab made me feel welcome from the first day. Ramon, the only other member who has spent an appreciable amount of time in both labs, was a great resource for both answering computer questions and helping me manage two advisors. Elaine has been a great labmate to both talk science and commiserate with. Christian's relaxed attitude and rigorous science always set a positive tone in the lab. Sharing the same side of the lab, Austin graciously put up with all my antics and never complained as I constantly harassed him with very basic Matlab and scripting questions. Thanks to Orly for many cups of coffee (or tea), great conversations, and yummy dinners. Charles, for providing equation-filled group meetings and having patient and clear responses to my obnoxious (and most likely trivial) questions. Thanks also to Sophie for helping me move, stay sane, and be insane on occasion. To newer members of the Drennan and Stultz labs, thanks for your support and best of luck!

I also must thank the many UROPs I've had while at MIT: Andrew, Anjali, Daniel, Madhavi, Collins, and Stephanie. They've all played a big role in helping me mature as an advisor, researcher, and teacher and I thank them very much for that.

A few lab members have been omitted from above, because without their knowledge, support, and friendship I firmly believe I would have quit graduate school long ago. Leah has been a great role model in lab and in life. Her enthusiasm for not only science, but also spending time with family, the outdoors, and having fun helped remind me to stay balanced throughout graduate school. Although I didn't follow her to the synchronized swimming team and she only spent a single semester with me in the pottery studio, we always had a great time out of lab using the "other half of the brain" to cook, crochet, paint, and make papier mâché iron-sulfur clusters. Over the last months as we each struggled with long distance relationships, we spent hours together laughing, crying, and working—all of which I'm going to miss as we move to separate cities.

To get me off the ground when I joined the Stultz lab in my 3<sup>rd</sup>, Paul was "assigned" as my mentor, teaching me CHARMM, helping me interpret Delphi's user manual, and explaining all physics-related concepts. Fortunately for me, this worked out wonderfully and with Paul's help

we had a publication within 1½ years of joining the lab. Without his patience and sarcastic but encouraging attitude, the process would have taken much longer. After spending the last six months commiserating about theses, science, and long-distance relationships, Paul has decided he can still put up with me for a bit longer as we'll both be working in labs located in Stanley Hall at UC Berkeley for our postdocs. If all goes well, I envision many fruitful collaborations in the future.

Even though he started a year after me, I can't really remember a time in the Drennan lab without Yan. He has been my "go-to" person in the lab when I have any question about biochemistry, crystallography, and molecular biology. He's also edited many manuscripts, emails, and fellowship proposals for me. Outside of lab, I've been fortunate to have Yan as a close friend. Having spent countless hours playing Settlers, Carcassonne, and other board games with he and Casey it's going to be difficult for Nick and I to find new game partners in Berkeley. Of course, since Yan will be moving to Berkeley soon, we'll only have to suffer for a year at most.

I feel most fortunate for having had the pleasure to work with members of both the Drennan and Stultz lab for the last 5½ years not because they're the smartest group of people I've ever known (although they are), but because I have been able to work with a great group of friends. I will miss them all dearly and look forward to my visits back to Boston.

In addition to my labmates, I've been fortunate to have a great network of friends outside of the lab. The summer softball team, the Merohedral Twins, were a great source of amusement every Monday night in the summer. For listening to my rants, complaints, and bizarre lab stories as well as numerous fun times together, many thanks to Casey, Laura, Eugene, Heather, Sam, Alisha, Maria, John, Jen, Mary, Audra, Eric, Ashtu, Sean, and Shep. For anyone reading this whose name isn't mentioned here, undoubtedly you should be thanked and I apologize for the omission. Thank you. I'd also like to thank my family, especially my Mom, Renée, Joe and Matt for always reminding me that there is life outside the lab.

Finally, I would like to give a special thanks to my fiancé Nick. Never faltering as my strongest supporter, I have been so fortunate to find someone I am so comfortable with and who mutually enjoys spending as much time together as possible. I always joke that if nothing else, I found a husband in graduate school. But in all honesty, the most important things I've learned and experienced over the last five years have been with Nick, and I am excited to start the next chapter of my life with him.



# TABLE OF CONTENTS

## Chapter I: Introduction to NikR

<b>A. Abstract</b>	13
<b>B. Metal Homeostasis in Bacteria</b>	14
<b>C. Nickel in Bacteria</b>	14
<b>D. Nickel Regulatory Protein, NikR</b>	16
<b>E. Biochemistry of NikR</b>	19
1. <i>Nickel binding properties of NikR</i>	
2. <i>Studies of NikR-DNA binding</i>	
3. <i>Biochemical studies of metal specificity</i>	
<b>F. Crystal Structures of NikR</b>	21
1. <i>Overall structure</i>	
2. <i>Conformational changes upon nickel binding to NikR</i>	
3. <i>Conformational changes of NikR with DNA binding</i>	
4. <i>Structural details of NikR-DNA interactions</i>	
<b>G. Spectroscopic Studies of NikR</b>	28
1. <i>Spectroscopic studies of the high-affinity nickel site</i>	
2. <i>Spectroscopic studies of EcNikR with various transition metals</i>	
3. <i>Spectroscopic studies of the low-affinity nickel binding site</i>	
<b>H. The Metal Binding Sites of NikR</b>	29
<b>I. References</b>	31
<b>J. Figures</b>	
1. <i>X-ray crystal structure of NiFe hydrogenase</i>	15
2. <i>X-ray crystal structure of urease</i>	16
3. <i>Nickel uptake and regulation in Escherichia coli</i>	17
4. <i>Series of crystal structures of EcNikR</i>	22
5. <i>Representative crystal structures of HpNikR and PhNikR</i>	22
6. <i>Topology diagram of a single monomer of NikR</i>	23
7. <i>The high affinity nickel binding site of EcNikR</i>	24
8. <i>The second metal binding site of EcNikR</i>	26
9. <i>Schematic of NikR-DNA interactions</i>	27

## Chapter II: Structural Basis of the Metal Specificity for Nickel Regulatory Protein NikR

<b>A. Abstract</b>	35
<b>B. Introduction</b>	36
<b>C. Results</b>	38
1. <i>Full Length versus MBD NikR Structures</i>	
2. <i>Metal-Binding Sites</i>	
3. <i>Alpha 3 Helix</i>	
<b>D. Discussion</b>	46
1. <i>Metal binding to NikR</i>	
2. <i>Ordering of the <math>\alpha 3</math> helix is metal-dependent</i>	
3. <i>Ordering of <math>\alpha 3</math> helix is linked to DNA binding</i>	
4. <i>Mechanism of NikR binding to DNA</i>	
5. <i>Conclusions</i>	
<b>E. Methods</b>	52

1.	<i>Structure determination of apo-MBD NikR</i>	
2.	<i>Structure determination of Cu<sup>2+</sup>-MBD NikR</i>	
3.	<i>Structure determination of Zn<sup>2+</sup>-MBD NikR</i>	
4.	<i>Criteria for including <math>\alpha 3</math> in model</i>	
5.	<i>Circular dichroism of Ni<sup>2+</sup>, Cu<sup>2+</sup>, Zn<sup>2+</sup>, and Apo-MBD</i>	
<b>F.</b>	<b>Acknowledgments</b>	57
<b>G.</b>	<b>References</b>	58
<b>H.</b>	<b>Tables</b>	
1.	<i>Distances and angles around the metals in the metal-bound MBD structures</i>	40
2.	<i>Average B-factors (in Å<sup>2</sup>) for different portions of the apo, Zn<sup>2+</sup>-, Cu<sup>2+</sup>-, and Ni<sup>2+</sup>-bound MBD structures</i>	43
3.	<i>Root-mean-squared deviations (RMSDs) between the C<sub>a</sub> atoms in apo and metal-bound MBD NikR structures</i>	47
4.	<i>Data collection and refinement statistics</i>	53
<b>I.</b>	<b>Figures</b>	
1.	<i>Structures of E. coli NikR</i>	37
2.	<i>Metal binding sites with 2F<sub>o</sub>-F<sub>c</sub> electron density</i>	39
3.	<i>Two monomer “states” in the Zn-MBD crystal</i>	41
4.	<i>Hydrogen bonding network connecting two nickel binding sites</i>	42
5.	<i>Ordering of the <math>\alpha 3</math> helix</i>	43
6.	<i>One sigma 2F<sub>o</sub>-F<sub>c</sub> electron density around the area of the <math>\alpha 3</math> helix</i>	45
7.	<i>Proposed NikR regulatory mechanism</i>	50

### Chapter III: Physical Basis of Metal-Binding Specificity in *Escherichia coli* NikR

<b>A.</b>	<b>Abstract</b>	63
<b>B.</b>	<b>Introduction</b>	64
<b>C.</b>	<b>Results</b>	67
1.	<i>The Conformation of High Affinity Sites in the Presence of Ni<sup>2+</sup> or K<sup>+</sup></i>	
2.	<i>The Conformation of the Second Metal Binding Site in the Presence of Ni<sup>2+</sup> or K<sup>+</sup></i>	
3.	<i>EcNikR-DNA Association with Either Ni<sup>2+</sup> or K<sup>+</sup> in the Second Metal Binding Site</i>	
4.	<i>The Effect of Ion Size on DNA Binding</i>	
<b>D.</b>	<b>Discussion</b>	77
<b>E.</b>	<b>Methods</b>	81
1.	<i>Structure Preparation and Solvation</i>	
2.	<i>Minimization and Molecular Dynamics of the High Affinity Site in EcNikR</i>	
3.	<i>Minimization and Molecular Dynamics of the Second Metal Binding Site in the EcNikR-DNA Complex</i>	
4.	<i>MMPB Studies</i>	
5.	<i>Thermodynamic Integration</i>	
<b>F.</b>	<b>Acknowledgments</b>	87
<b>G.</b>	<b>References</b>	88

<b>H. Tables</b>	
1. <i>Contributions to the electrostatic free energy difference</i>	74
2. <i>Free energy differences between EcNikR-DNA complex with K<sup>+</sup> and other monovalent ions</i>	77
<b>I. Figures</b>	
1. <i>Crystal structures of EcNikR and the metal binding sites</i>	65
2. <i>Representative structures of the high affinity metal binding sites after energy minimization and MD simulation studies</i>	68
3. <i>Representative structures of the second metal binding site from minimization studies of the EcNikR-DNA complex</i>	70
4. <i>Thermodynamic path comparing EcNikR-DNA binding with either K<sup>+</sup> or Ni<sup>2+</sup> at the second metal binding site</i>	71
5. <i>Thermodynamic cycle for calculating the electrostatic free energy difference associated with replacing potassium with nickel in the second metal binding sites</i>	73
6. <i>EcNikR-DNA structure with residues with the most extreme contributions to <math>\Delta\Delta G</math></i>	75
7. <i>Thermodynamic cycle for calculating the free energy difference associated with replacing a monovalent cation with the radius of potassium with a larger or smaller radius</i>	76
8. <i>Representative graphs of metal-ligand distances for the four known metal ligands of the high affinity site</i>	80
9. <i>The average energy of the system over the time of the simulation with either K<sup>+</sup> or Ni<sup>2+</sup> bound in the high affinity site</i>	83
10. <i>The average energy the system over the time of the simulation with either K<sup>+</sup> or Ni<sup>2+</sup> bound in the second metal binding site</i>	84

## Chapter IV: Examining the Low Affinity Nickel Binding Sites of *Escherichia coli* NikR

<b>A. Abstract</b>	93
<b>B. Introduction</b>	94
<b>C. Results</b>	95
1. <i>Crystal structure of NikR in the absence of DNA soaked with 8 mM NiCl<sub>2</sub></i>	
2. <i>Nickel anomalous density in the NikR-DNA structure soaked with 5 mM NiCl<sub>2</sub></i>	
3. <i>Low affinity Ni<sup>2+</sup> sites from the crystal structures</i>	
4. <i>Molecular dynamics simulations of site types 1-3 on the NikR-DNA complex</i>	
<b>D. Discussion</b>	104
<b>E. Methods</b>	110
1. <i>Refinement of crystal structure of NikR soaked with 8 mM NiCl<sub>2</sub> and identification of nickel sites</i>	
2. <i>Identifying nickel sites on a NikR-DNA complex using anomalous scattering from low resolution X-ray data</i>	
3. <i>Modeling ligands to potential low affinity nickel sites on the NikR-DNA complex</i>	
<b>F. Acknowledgments</b>	114
<b>G. References</b>	115

<b>H. Tables</b>	
1. <i>Data collection statistics for NikR and NikR-DNA complex</i>	96
2. <i>Descriptions of the types of low affinity nickel sites seen in the NikR and NikR-DNA complex structure</i>	97
<b>I. Figures</b>	
1. <i>Nickel anomalous density maps of excess nickel soaked NikR and NikR-DNA complexes</i>	98
2. <i>Low affinity nickel sites 1-3, 5 and 6 from the crystal structure of NikR without DNA</i>	100
3. <i>Low affinity nickel site 4 is stabilized by a crystallographically-related DNA molecule</i>	102
4. <i>Representative structures following 1 ns molecular dynamics simulation of three types of low affinity nickel binding sites</i>	103
5. <i>Representative composite omit density in the NikR structure with excess nickel</i>	106
6. <i>Sequence alignment of various NikR homologs, including <i>E. coli</i> and <i>H. pylori</i></i>	107
7. <i>Proposed scheme for NikR-DNA binding</i>	110
<b>Chapter V: Searching for the <i>nik</i> Operon: Relating the Mechanism for NikR Binding DNA to Current Theories of how Transcription Factors Find their DNA Binding Sites</b>	
<b>Figures</b>	
1. <i>Crystal structures of full-length <i>E. coli</i> NikR</i>	121
2. <i>K<sup>+</sup> site links an extending H-bonding network between NikR and DNA</i>	122
3. <i>Proposed model for NikR search for <i>nik</i> operon on DNA</i>	123
4. <i>Putative energy landscape for NikR when bound to DNA in two different conformations</i>	126
<b>References</b>	127
<i>Curriculum vitae</i>	131

## **Chapter I: Introduction to NikR**

### **I.A. Abstract**

The variety of roles that transition metals fulfill within the cell is staggering, and the concentrations of these metals must be tightly regulated to maintain minimal requisite levels yet simultaneously prevent metal-induced oxidative stress or inappropriate metal binding events. One transition metal that is essential to bacteria, albeit in very low concentrations, is nickel. Bacteria control the intracellular concentration of nickel using the transcriptional repressor NikR. When the nickel concentration in a cell becomes too high, the NikR protein binds nickel ions, inducing NikR's affinity for a promoter region upstream of a gene encoding a nickel-specific importer. This binding event blocks RNA polymerase from attaching to the DNA, preventing the continued expression of nickel-specific importers. Biochemical, structural, and spectroscopic studies on NikR have indicated that NikR actually has multiple metal binding sites, which accommodate different metal ions. The complexities of the metal binding properties of this transcription factor are described in this chapter and provide the main focus for the work described in the following chapters.

## I.B. Metal Homeostasis in Bacteria

Metal ions are crucial cofactors in all biological systems. In bacteria, metal ions assist in enzymatic reactions, electron transport, small molecule sensing, and many other processes. The high reactivity, varied coordination states, ability to serve in various catalytic roles, and rich redox activity of transition metal ions make them an excellent resource for the cell, but they can also act as toxins. Thus, the concentration of metal ions must be tightly controlled within the cell and common thought is that there are no free metal ions in the cell—that is, all metal ions in the cell are bound to a protein, small molecule, or DNA and are not freely diffusing through the cell. Many metal storage, chaperone, and regulatory proteins have been characterized over the past decades, supporting the concept of strict metal regulation in the cell.

## I.C. Nickel in Bacteria

Nickel is an essential cofactor in a number of bacteria. A list of known nickel-containing enzymes include: hydrogenase, urease, superoxide dismutase, carbon monoxide dehydrogenase, acetyl-CoA synthase, methyl-CoM reductase, glyoxylase I, and acireductone dioxygenase (1). Bacterial cells have also evolved a number of accessory proteins to assist in obtaining, delivering, storing, and regulating the concentration of nickel within the cell. Nickel regulation is crucial because high metal concentration can cause cell death (2, 3).

Among the bacteria for which nickel is essential to survival are the human pathogens *Escherichia coli* and *Helicobacter pylori*. The pathogenic CFT073 strain of *E. coli* is responsible for causing urinary tract or bladder infections (4). To live in the slightly anaerobic environment of the urinary tract or bladder, these bacteria utilize the enzyme hydrogenase, which contains a Ni-Fe cofactor (Figure I.1), and catalyzes the following reaction (Scheme I.1) as the main energy source for the bacterium (5):

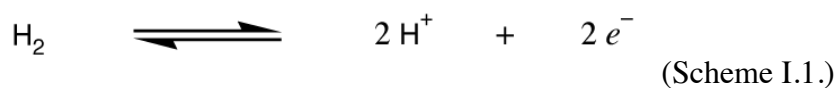
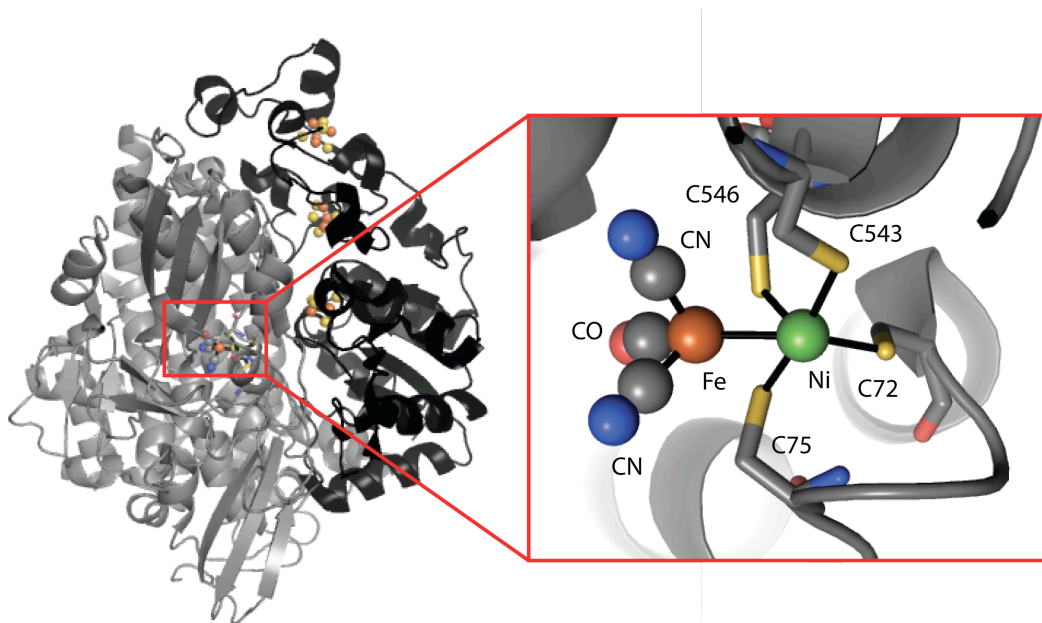


**Figure I.1.** X-ray crystal structure of NiFe hydrogenase from *Desulfovibrio fructosovorans* (PDB ID 1YRQ). The overall fold is shown on the left and active site composition on the right. Carbons are grey, nitrogens blue, sulfur yellow, oxygen red, iron orange, and nickel green. All structural figures are made with PyMOL (6).



*H. pylori* are gram-negative bacteria known to cause stomach ulcers by colonizing the stomach mucosa. Survival in the acidic environment of the stomach, where the pH can be as low as 1, requires the utilization of the nickel-containing enzyme urease (Figure I.2). At the nickel catalytic site in urease, urea is converted to ammonia, which helps neutralize the pH of the bacterial cytosol, via the reactions shown in Scheme I.2.

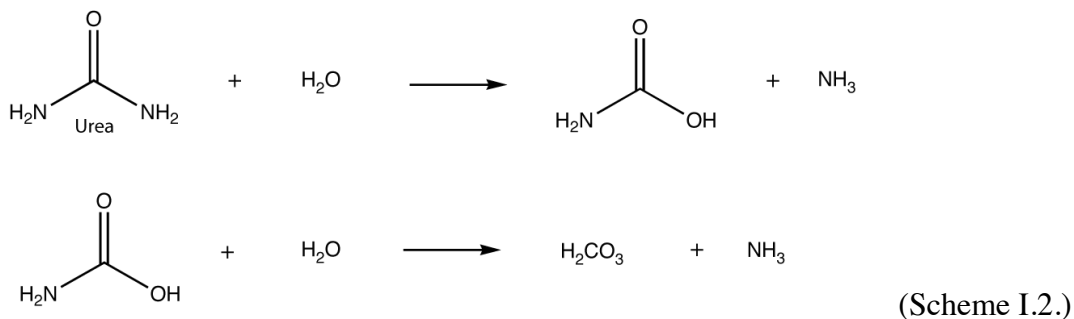
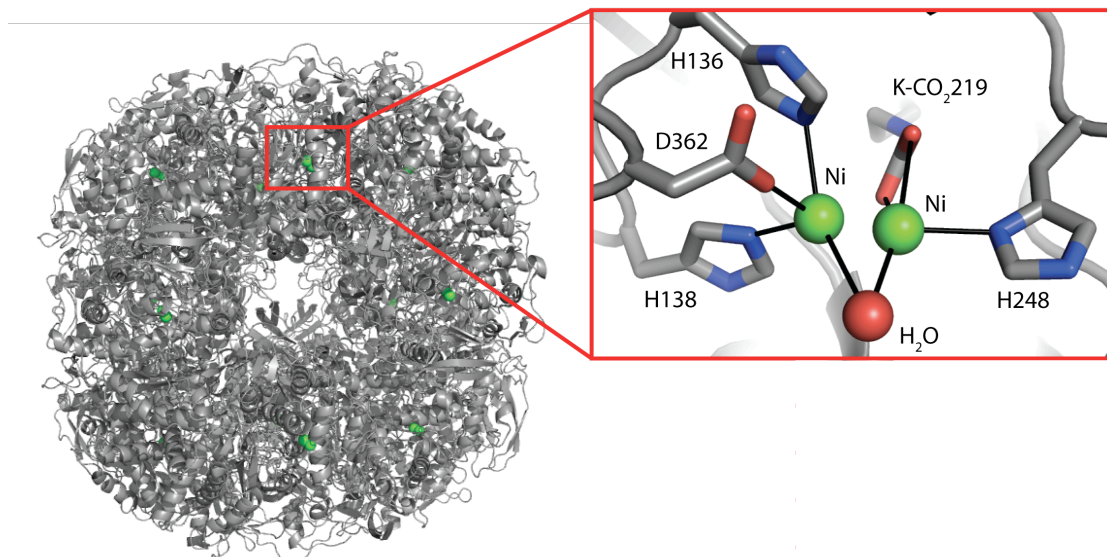


**Figure I.2:** X-ray crystal structure of urease and the di-nickel catalytic site from *Helicobacter pylori* (PDB ID 1E9Z). Coloring the same as in Figure I.1 with the red sphere representing a water molecule.



The focus of the work in this thesis is on the nickel regulatory transcription factor, NikR, and how bacteria and specifically *E. coli* use this protein to regulate the concentration of nickel in the cell.

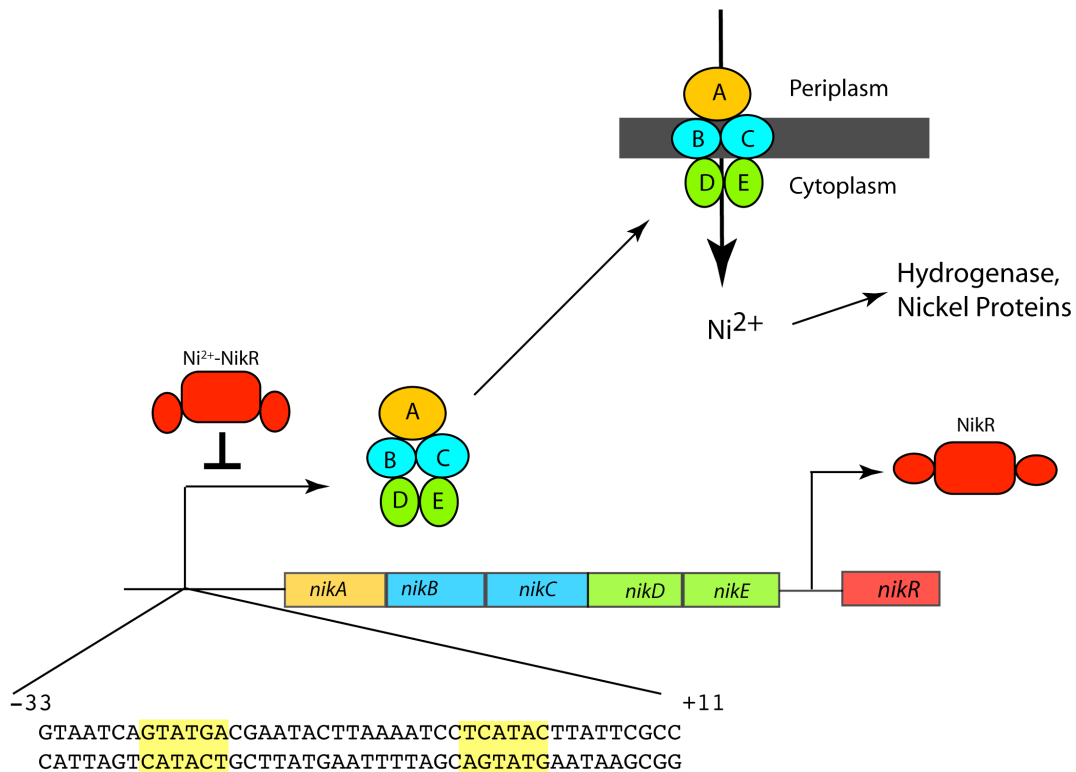
#### **I.D. Nickel Regulatory Protein, NikR**

The transcription factor NikR is used to regulate the concentration of nickel in many bacterial systems. The *nikR* gene has been found or predicted in more than 40 bacterial species and is often encoded in or near operons related to other nickel proteins (7). To date, the best characterized NikR protein is from *Escherichia coli* (EcNikR), though significant progress is being made on the *Helicobacter pylori* homolog (HpNikR) due to its importance in human pathology, and some characterization has also been performed on *Pyrococcus horikoshii* NikR (PhNikR). All characterized NikR homologues have been shown to be tetrameric at experimentally accessible concentrations, regardless of nickel concentration (7). However, all of these concentrations are above what one would expect



in the cell, so the true oligomeric state of the protein in the absence of nickel inside the cell remains uncertain (8).

**Figure I.3:** Nickel uptake and regulation in *Escherichia coli*. Nickel enters the cytoplasm from a nickel-specific ABC-type transporter, NikABCDE. NikA is a periplasmic nickel binding protein that hands nickel off to the transmembrane proteins, NikB and NikC. Nickel is then transported through the ATP-binding proteins NikD and NikE into the cell where it can be utilized by nickel-containing proteins such as hydrogenase. When there is too much nickel in the cell, nickel binds to the transcriptional regulator, NikR, which in turn binds upstream of the *nik* operon at the two half sites whose sequences are highlighted in yellow, blocking the transcription of the genes (*nikABCDE*) encoding for the nickel-specific uptake protein.



Although NikR always acts as a transcription factor, the biological role of this transcription factor appears to vary between organisms (7). In *E. coli*, the only known function of NikR is to regulate the transcription of the nickel-specific ABC-type transporter (ATP-binding cassette type transporter) complex, NikABCDE. This complex is responsible for nickel-specific import into the cell (9). When the concentration of nickel in the cell is high, nickel binds to NikR, which in turn binds to the *nik* operon, repressing transcription of NikABCDE (Figure I.3). In particular, NikR recognizes and binds palindromic operator sites on DNA separated by 16 base pairs and located upstream of the *nik* operon (Figure I.3) (10). Binding of NikR to the *nik* promoter region physically prevents RNA polymerase from binding to the start codon, thus inhibiting transcription of the *nikABCDE* genes.

Research on NikR in *H. pylori* (HpNikR) over the past few years has indicated that in this organism NikR regulates at least five different genes, all of which have some connection to nickel uptake or utilization in the cell. Similar to *E. coli* NikR, HpNikR has been shown to repress the transcription of a nickel-specific uptake protein, NixA (11, 12). This nickel-uptake protein is monomeric, in contrast to the ABC-type transporter in *E. coli* (12). In addition to down-regulating transcription of the *nixA* operon, HpNikR has been shown to enhance transcription of a urease accessory protein, UreA, and inhibit the transcription of three outer membrane proteins that may be involved in nickel transport into the periplasm (11, 13-15). The additional roles of NikR in *H. pylori* may reflect the importance of nickel in this organism.

Many other types of metal regulatory transcription factors are known, which all help maintain the proper concentration of different metals in the cell. Some examples are the iron sensors DtxR (Diphtheria toxin repressor)/IdeR (Iron dependent regulator) (16-20), the zinc uptake regulator Zur/FurB (Ferric uptake regulator B) (21), copper-sensing regulator CsoR (22), and molybdate dependent regulator ModE (23). These transcription factors have varied topologies and oligomerization states, but none have the same tetrameric organization as NikR.

## **I.E. Biochemistry of NikR**

### *I.E.1. Nickel binding properties of NikR*

The NikR protein was first reported in 1999 by de Pina *et al.*, who showed that this protein was responsible for repression of the *nik* operon under high nickel concentrations (24). Chivers and Sauer first reported a submicromolar affinity of nickel for NikR from a spectrophotometric assay and later specified the binding affinity as picomolar from nickel titration and competition assays (8, 10). The picomolar affinity of nickel for the protein was confirmed by Wang *et al.* in 2004 using a similar spectrophotometric competition assay (25). Recently, a study from Diederix *et al.* using filter binding assays, UV-Vis equilibration titrations, and rapid kinetics experiments has suggested that the affinity of nickel to protein is actually sub-micromolar but these results have not yet been reproduced (26).

A second, low-affinity nickel binding site has been identified in EcNikR using EcNikR-DNA affinity studies with stoichiometric and surplus amounts of nickel ions (8). In these experiments, NikR exhibited an increased affinity for DNA in the presence of excess nickel ions ( $2 \times 10^{-11}$  M, as compared to  $5 \times 10^{-9}$  M for stoichiometric nickel) (8, 27). The biological importance of this low affinity nickel binding site and where this site (or sites) is located has been debated and remains an open question that will be the discussion of Chapter IV.

### *I.E.2. Studies of NikR-DNA binding*

The initial studies of NikR-DNA binding were performed by Chivers and Sauer on the truncated N-terminal ribbon-helix-helix (RHH) domain of *E. coli* NikR and indicated that binding to the *nikABCDE* operon occurred between bases -31 and +2 (28). A study of the full-length protein followed, where DNA footprinting and mutational studies indicated that in the presence of stoichiometric nickel, EcNikR binds two dyad-symmetric GTAGTA sequences on DNA (highlighted in yellow in Figure I.3) separated by 16 base pairs in the region previously mentioned (10). Gel-shift mobility assays showed that nickel was required to induce DNA binding (10). *In vivo* LacZ reporter assays confirmed

that NikR bound the *nik* operon promoter region as the transcription of the *lacZ* gene was repressed when a plasmid containing a *nik* promoter-*lacZ* fusion was transformed into a cell expressing NikR (10).

Following these initial studies, more specific binding experiments were performed to determine the affinity of NikR for DNA under varying concentrations of nickel. The affinity of Ni<sup>2+</sup>-EcNikR for DNA was recorded as 30 nM in the presence of stoichiometric amounts of nickel (8, 25). NikR's affinity for the *nik* operon increased to picomolar strength in the presence of excess nickel ions (8, 25). This increased affinity was suggestive of the second nickel binding site on the protein introduced in the previous section (8, 25).

#### *I.E.4. Biochemical studies of metal specificity*

Binding studies to explore the affinity of different metals for the NikR protein illustrated that a number of transition metals can bind NikR with affinities corresponding to the Irving-Williams series: Mn<sup>2+</sup> < Co<sup>2+</sup> < Ni<sup>2+</sup> < Cu<sup>2+</sup> ≥ Zn<sup>2+</sup> (25). Gel-shift assays and DNA footprinting experiments revealed the abilities of these metals to induce NikR-DNA binding (27). These studies showed that copper and nickel induce DNA binding with similar nanomolar binding constants, while NikR binding of zinc, cobalt, and cadmium have a smaller effect on DNA binding (27). Proteolysis experiments, chemical and thermal stability assays, and hydrogen-deuterium exchange experiments indicate that nickel binding, and copper binding to a lesser extent, are able to stabilize the apo (Ni<sup>2+</sup>-free) protein more than any other metal tested (25, 29, 30).

A number of biochemical and spectroscopic studies have been performed to inspect the characteristics of NikR with the aforementioned metal ions upon DNA binding (25, 27, 29, 30). The *in vitro* studies suggest that divalent copper induces DNA binding as efficiently as divalent nickel ions, while a few other metals also impart a significant affinity to EcNikR for DNA (27). *In vivo* studies suggest that only nickel is able to repress transcription of the *nik* operon in the cell (30). In Chapter II of this thesis we look

at the structural effects of different transition metals binding to the high affinity sites of NikR and the conformational changes incurred by the correct metal ion binding to this site.

### **I.F. Crystal Structures of NikR**

The first crystal structures of EcNikR were reported by Schreiter *et al.* in 2003 and illustrated the overall tetrameric structure of the protein with two dimeric ribbon-helix-helix (RHH) domains flanking a central metal-binding domain (MBD) (Figure I.4) (31). The following structures of EcNikR had been published prior to the start of the work in this thesis: apo-NikR, Ni<sup>2+</sup>-bound MBD, Ni<sup>2+</sup>-bound NikR, and Ni<sup>2+</sup>-bound NikR bound to DNA (31, 32). In addition to the crystal structures of EcNikR, structures of HpNikR and PhNikR have also been reported (Figure I.5) (33, 34). The overall fold of these proteins is identical to that of EcNikR.

**Figure I.4:** Series of crystal structures of EcNikR. The RHH, MBD domains, and the  $\alpha 3$  helix are indicated. Each monomer is colored separately with the nickel ions as green spheres and the potassium ions in purple spheres. (a) apo-EcNikR, (b)  $\text{Ni}^{2+}$ -EcNikR, and (c) EcNikR-DNA with NikR in a “down-cis” configuration. The EcNikR-DNA structure has a transparent surface to highlight the interactions between the MBD and the DNA.

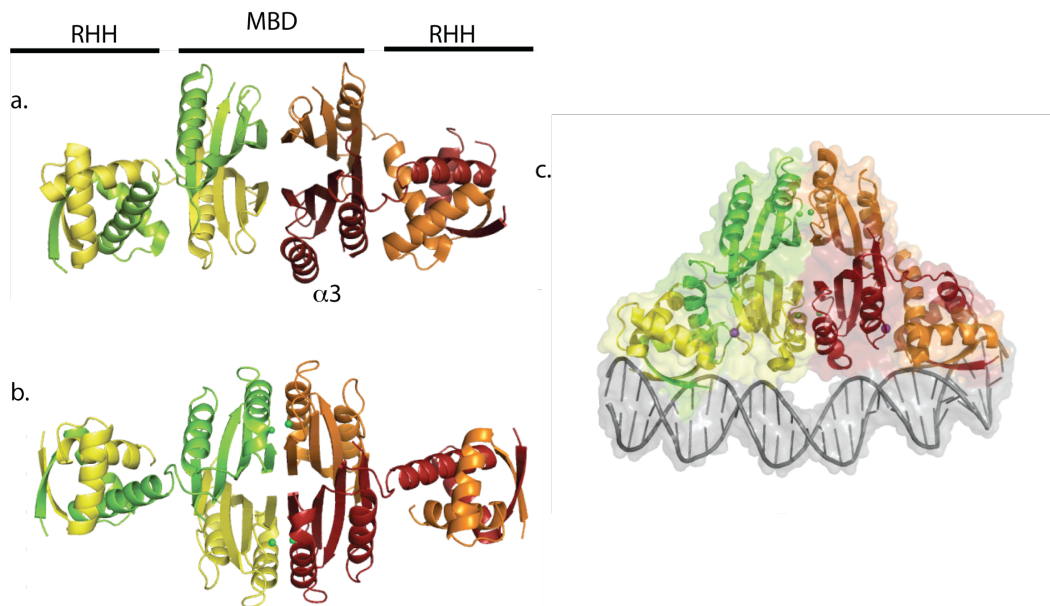
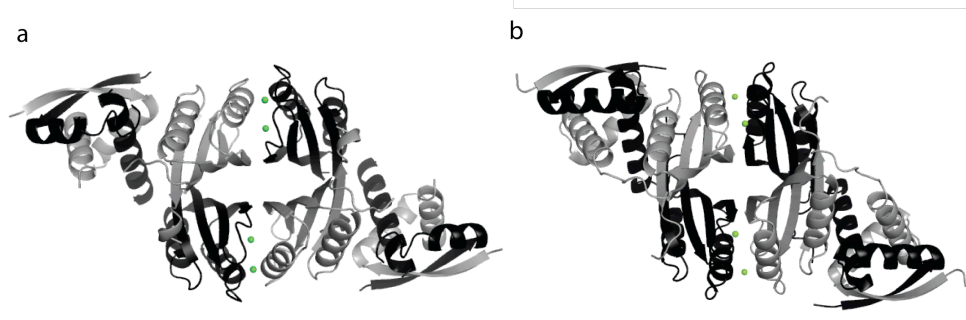


**Figure I.5:** Representative crystal structures of (a) *Helicobacter pylori* (PDB ID 2CAD) and (b) *Pyrococcus horikoshii* (PDB ID 2BJ7) NikR. Both NikR structures are in “down-trans” configurations. Nickel ions are in green spheres.



### I.F.1. Overall structure

The central MBD, which maintains the tetrameric interface, is composed of amino acids 48-133 and has an open  $\alpha/\beta$ -sandwich type fold with a  $\beta\alpha\beta\alpha\beta$  topology (Figure I.6). The two dimeric RHH domains compose the DNA binding motif and encompass residues 1-47. Proteins containing the RHH motif constitute one of the most common DNA binding families, with members performing a variety of functions within the cell (35). The nickel-bound EcNikR structure (Figure I.4b) shows that the MBD contains the four high-affinity nickel-binding sites, one in each monomer. These high affinity sites lie close to the tetrameric interface (Figure I.7) and play a key role in regulating NikR's affinity for DNA (32). The DNA-bound EcNikR structure illustrates that a second metal binding site is formed when NikR is bound to DNA and the RHH domains are in a “down-*cis*” position (Figures I.4c and I.8) (32). The identity and importance of the metal at this site is discussed in Chapter III of this thesis.

**Figure I.6:** Topology diagram of a single monomer of NikR. Helices are represented by grey rectangles and  $\beta$  strands are represented by black arrows, with loops drawn as lines. All  $\alpha$  helices and  $\beta$  strands are labeled to their left. The MBD and RHH domains are labeled.

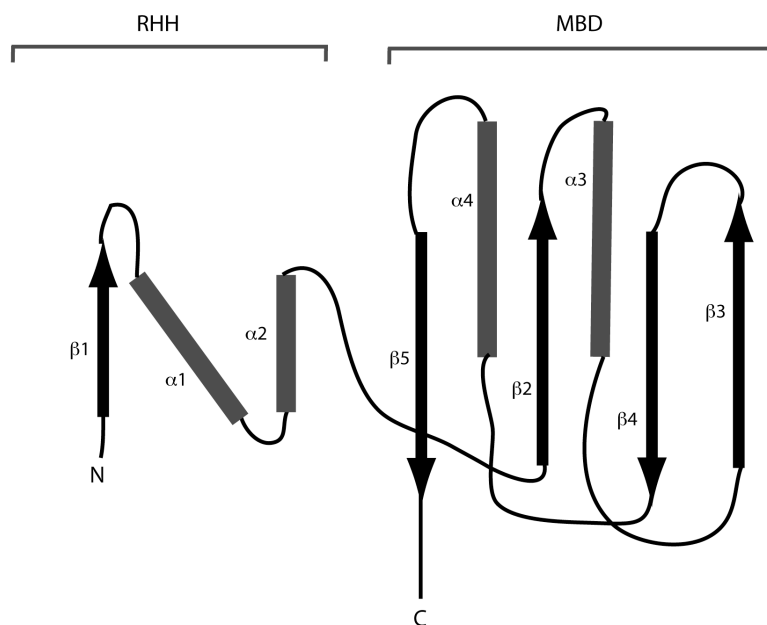
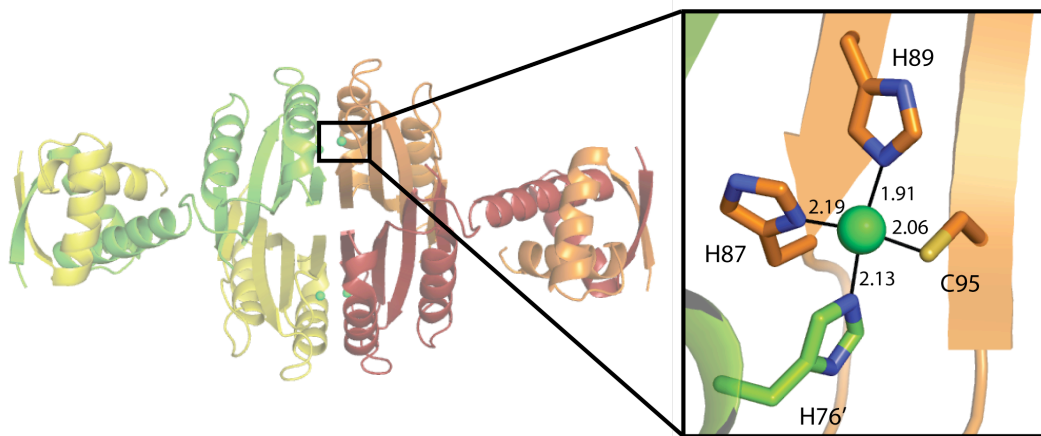


**Figure I.7:** The high affinity nickel binding site with nickel represented in a green sphere. Structure of Ni<sup>2+</sup>-bound EcNikR (PDB ID 2HZA).

Distances are in Å.



The wealth of structures of EcNikR provide snapshots of the organizational and conformational ensembles of full-length EcNikR in the most biologically relevant forms: without nickel (apo), nickel-bound, and in complex with DNA.

#### *I.F.2. Conformational changes upon nickel binding to NikR*

At the tetrameric interface of the EcNikR protein complex lies a square planar nickel binding site. The residues that make up this high-affinity nickel-binding site are His87, His89, and Cys95 from one monomer and His76' from a neighboring monomer (Figure I.7). These four residues are conserved in all known NikR sequences (31).

In the crystal structure solved in the absence of metal, His89, His87, and Cys95 are in different positions than when nickel is bound, and His76' has high B-factors or poor electron density to describe its position, indicating that this region is highly flexible and not pre-ordered for nickel binding. However, once nickel binds in this site, these four residues and a number of neighboring residues are repositioned, creating a hydrogen-bonding network connecting two nickel sites. Involved in this network are His76 and Gln75, two residues in the  $\alpha$ -helix neighboring the metal site ( $\alpha$ 3). When ordered by



appropriate metal binding, these residues help anchor the  $\alpha 3$  helix into place, stabilizing the rest of the residues in the helix and the preceding loop (32, 36).

### *I.F.3. Conformational changes of NikR with DNA binding*

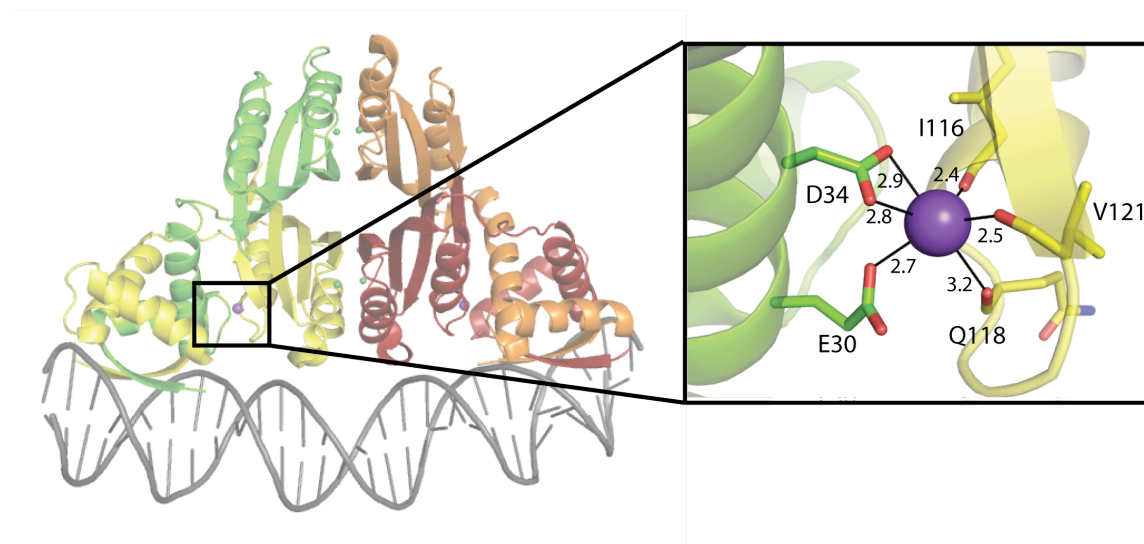
Comparison of the apo-EcNikR and Ni<sup>2+</sup>-bound EcNikR structures indicates an ordering of the  $\alpha 3$  helix and preceding loop (64-65) upon nickel binding (31, 32). In the DNA-bound EcNikR structure, this loop makes direct contacts to phosphates on the DNA backbone. Thus, we hypothesize that anchoring the  $\alpha 3$  helix is an important conformational change, readying the protein for DNA binding (32, 36). We test this hypothesis in Chapter II.

In addition to the flexibility of the  $\alpha 3$  helix, the RHH domain of NikR has been shown to take on different orientations in the numerous crystal structures of full-length NikR from three organisms (31-34). In the apo- and Ni<sup>2+</sup>-EcNikR structures these “arms” are in an “out” position (Figures I.4a and I.4b), while in the EcNikR-DNA structure the RHH domains are in a “down-*cis*” position (Figure I.4c), indicating that the binding of nickel does not induce ordering or correct orientation of the DNA binding region of the protein (32). The apo- and one of the nickel-bound PhNikR (Ni1-PhNikR) structures also have the RHH domains in an “out” position, but a second structure (Ni2-PhNikR) shows the RHH domains in a “down-*trans*” position (Figure I.5) (34). Finally, the apo- and Ni<sup>2+</sup>-HpNikR structures have the RHH domains in a “down-*trans*” conformation (33). While some of these conformers may be strained due to crystal contacts, the variability of the orientation of the RHH domains in these crystal structures highlights their flexibility. A computational study examining the vibrational modes of the protein based on published crystal structures confirms that the RHH domains are a very flexible region of the protein until DNA is bound (37).

In the EcNikR structure, the realignment of the RHH domains in a “down-*cis*” orientation creates a second metal binding site at the interface between the RHH and MBD domains (Figures I.4 and I.8). The second metal binding site is an octahedral site formed by side-

chains E30 and D34 of the RHH domain and backbone carbonyls of the MBD (Figure I.8) (32). The lack of nickel anomalous difference density in this area of the crystal structure and the high concentration of potassium in the crystallization condition (200 mM) suggest that this site is occupied by potassium in the crystals (32). Interestingly, the corresponding site in PhNikR is filled with nickel in one of the crystal structures, suggesting nickel can also bind at this site (34). In Chapter III we examine which metal is preferred to bind in this second metal binding site and why that metal is preferred.

**Figure I.8:** The second metal binding site from the co-crystal structure of EcNikR and DNA with a potassium ion represented in a purple sphere (PDB ID 2HZV). Distances in Å.

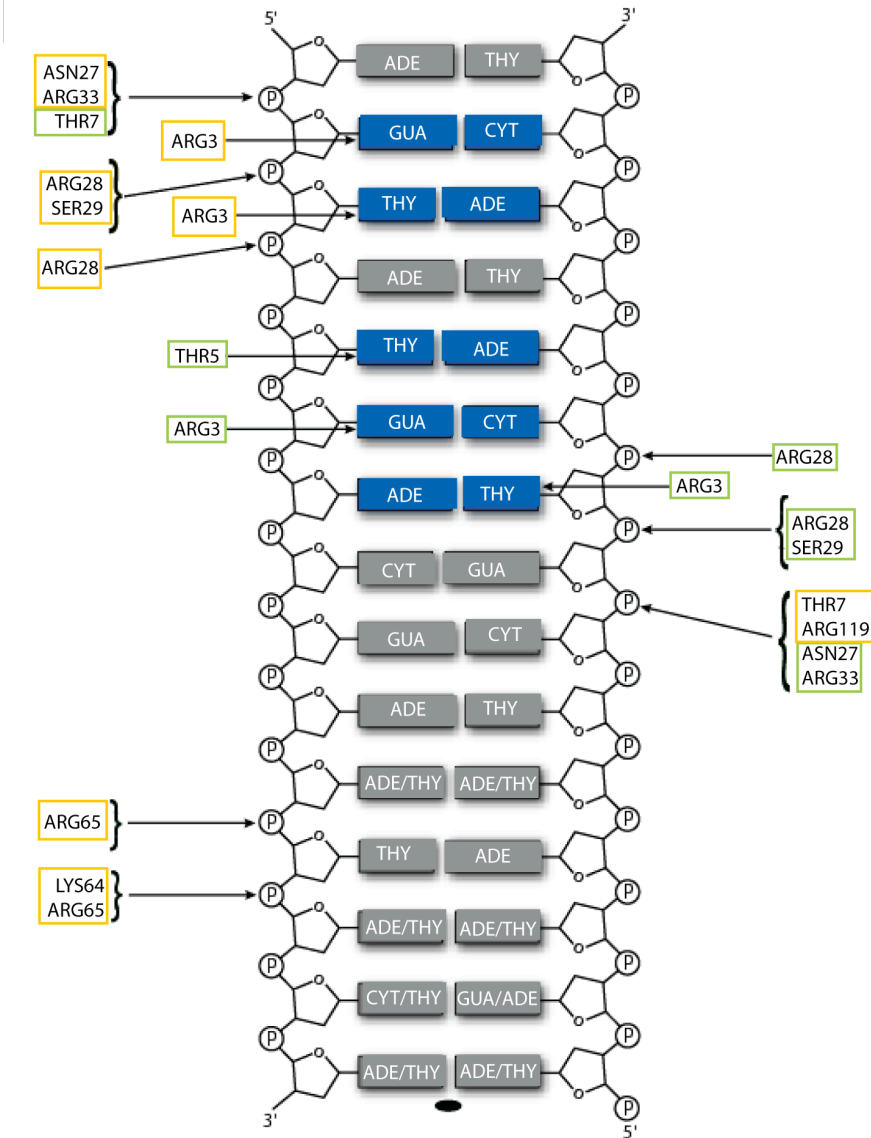


#### *I.F.4. Structural details of NikR-DNA interactions*

The specific interactions between EcNikR and DNA were revealed in the EcNikR-DNA structure (32). This structure confirmed key interactions between the first few residues in the RHH domain (namely Arg3 and Thr5) with nucleotides in the DNA (Figure I.9) (10, 32). In addition, there were numerous contacts between the RHH region and the DNA phosphate backbone (Figure I.9). Residues 64, 65, and 119 of the MBD also make direct hydrogen-bonding contacts with the DNA phosphate backbone (Figure I.9). A transparent surface representation of the NikR and DNA is shown in Figure I.4c and illustrates the

extensive amount of surface area shared between NikR and DNA, including a significant amount of interaction between the MBD and the DNA.

**Figure I.9:** Schematic of NikR-DNA interactions. Direct contacts between amino acids in NikR and the DNA are indicated with half of the palindromic DNA, or one of the two RHH binding sites. Blue nucleotides illustrate sites where mutations reduce NikR-DNA binding. Amino acids are boxed with colors corresponding to the monomer they belong to in Figure I.4c (adapted from Reference 31).



## **I.G. Spectroscopic Studies of NikR**

### *I.G.1. Spectroscopic studies of the high-affinity nickel site*

EXAFS (Extended X-ray Absorption Fine Structure) studies comparing Ni<sup>2+</sup>-EcNikR and Ni<sup>2+</sup>-EcNikR-DNA spectra suggested a change in nickel coordination number from four to six upon DNA binding (38). While this coordination change would introduce an interesting mechanism for sensing DNA, this result has not been confirmed and is inconsistent with crystallographic studies (32). The Ni-EcNikR-DNA complex structure shows the high-affinity nickel site as a 4-coordinate, square planar geometry identical to that of the Ni<sup>2+</sup>-EcNikR nickel site (32). In contrast, the nickel-ligand distances predicted by EXAFS data and the crystal structure for the high affinity site of NikR in absence of DNA are in excellent agreement.

### *I.G.2. Spectroscopic studies of EcNikR with various transition metals*

EXAFS and XANES (X-ray Absorption Near Edge Structure) studies by the Maroney laboratory have indicated that like Ni<sup>2+</sup> ions, Cu<sup>2+</sup> ions bind to NikR with square-planar coordination geometries (30). These spectroscopic studies also showed that Co<sup>2+</sup> ions bind with an octahedral geometry, Zn<sup>2+</sup> in tetrahedral coordination, and Cu<sup>+</sup> in a trigonal geometry (30). Crystallographic studies looking at NikR with various transition metals bound are discussed in Chapter II and crystal structure data are compared with this spectroscopic work.

### *I.G.3. Spectroscopic studies of the low-affinity nickel binding site*

In an attempt to visualize the coordination environment of the low-affinity nickel binding site using EXAFS and XANES, the Maroney laboratory incubated NikR first with DNA and stoichiometric divalent copper and then added excess nickel ions. In these studies, copper ions bound to the high affinity metal binding site with the typical square planar geometry and nickel ions bound in a 6-coordinate octahedral geometry with a spectrum best fit to two imidazole ligands and four additional N/O donors (30). Studies with nickel at the high affinity site with the typical square planar geometry and excess cobalt added to the sample suggest that cobalt also binds in a 6-coordination arrangement in a site

different from the high affinity nickel site (30). These studies suggest that a second low-affinity metal binding site maintains an octahedral geometry and may be composed by two histidine ligands and a number of other N/O donors. However, these studies do not indicate where on the protein the low affinity sites are located or if the sites seen here are indeed where the excess nickel ions bind to enhance NikR's affinity to DNA. In Chapter IV we discover potential low-affinity nickel sites and discuss the importance of these sites for enhancing NikR-DNA binding affinity.

### **I.H. The Metal Binding Sites of NikR**

To summarize; biochemical, spectroscopic, and structural work on EcNikR has indicated that this protein has at least three types of metal binding sites: a high affinity nickel site, a second metal binding site at the interface of the RHH and MBD, and one or more low affinity nickel sites. The high affinity nickel site is best suited for a nickel ion but can accommodate a number of transition metals. In Chapter II we examine the different binding modes of other transition metal ions at this site using protein crystallography. We then draw connections between metal binding and DNA binding and important conformational changes induced by the correct metal binding to the high affinity site. These parallels allow us to develop a model for nickel-dependent NikR-DNA binding.

A co-crystal structure of NikR bound to DNA indicated the presence of a second metal binding site at the interface of the MBD and RHH domains. In the crystal structure, this metal is most likely a potassium ion due to the high concentration of potassium in the crystallization condition and lack of nickel anomalous density at this site. However, the question remains if this site preferentially binds nickel, as is seen in the PhNikR crystal structure, or another metal ion. In Chapter III we use molecular dynamics, Poisson-Boltzmann electrostatic calculations, and thermodynamic integration to examine which metal is preferred to bind at the second metal binding site and why.

Early work on the NikR system illustrated that NikR has two affinities for DNA—a nanomolar affinity when stoichiometric nickel is bound to the protein and a picomolar

affinity when excess nickel ions are present. The enhanced DNA affinity with extra nickel ions suggests that there are one or more low affinity nickel sites on the protein. Our attempt to locate and analyze these sites using a combination of X-ray crystallography and the molecular mechanics Poisson-Boltzmann approach are described in Chapter IV.

## I.I. References

1. Li, Y., and Zamble, D. B. (2009) Nickel Homeostasis and Nickel Regulation: An Overview, *Chem. Rev.* *109*, 4617-4643.
2. Mulrooney, S. B., and Hausinger, R. P. (2003) Nickel uptake and utilization by microorganisms, *FEMS Microbiol. Rev.* *27*, 239-261.
3. Wu, L. F., Navarro, C., de Pina, K., Quenard, M., and Mandrand, M. A. (1994) Antagonistic Effect of Nickel on the Fermentative Growth of *Escherichia coli* K-12 and Comparison of Nickel and Cobalt Toxicity on the Aerobic and Anaerobic Growth, *Environ. Health* *102*, 297-300.
4. Welch, R. A., Burland, V., Plunkett, G., Redford, P., Roesch, P., Rasko, D., Buckles, E. L., Liou, S. R., Boutin, A., Hackett, J., Stroud, D., Mayhew, G. F., Rose, D. J., Zhou, S., Schwartz, D. C., Perna, N. T., Mobley, H. L. T., Donnenberg, M. S., and Blattner, F. R. (2002) Extensive mosaic structure revealed by the complete genome sequence of uropathogenic *Escherichia coli*, *Proc. Natl. Acad. Sci. U. S. A.* *99*, 17020-17024.
5. Uden, G., and Bongaerts, J. (1997) Alternative respiratory pathways of *Escherichia coli*: energetics and transcriptional regulation in response to electron acceptors, *Biochim. Biophys. Acta* *1320*, 217-234.
6. DeLano, W. L. (2002) The PyMOL Molecular Graphics System, DeLano Scientific LLC, San Carlos, CA, USA.
7. Dosanjh, N. S., and Michel, S. L. J. (2006) Microbial nickel metalloregulation: NikRs for nickel ions, *Curr. Opin. Chem. Biol.* *10*, 123-130.
8. Chivers, P. T., and Sauer, R. T. (2002) NikR Repressor: High-Affinity Nickel Binding to the C-Terminal Domain Regulates Binding to Operator DNA, *Chem. Biol.* *9*, 1141-1148.
9. Navarro, C., Wu, L. F., and Mandrand-Berthelot, M.-A. (1993) The *nik* operon of *Escherichia coli* encodes a periplasmic binding-protein-dependent transport system for nickel., *Mol. Microbiol.* *9*, 1181-1191.
10. Chivers, P. T., and Sauer, R. T. (2000) Regulation of high affinity nickel uptake in bacteria. Ni<sup>2+</sup>-Dependent interaction of NikR with wild-type and mutant operator sites, *J. Biol. Chem.* *275*, 19735-19741.
11. Ernst, F. D., Kuipers, E. J., Heijens, A., Sarwari, R., Stoof, J., Penn, C. W., Kusters, J. G., and van Vliet, A. H. M. (2005) The Nickel-Responsive Regulator NikR controls Activation and Repression of Gene Transcription in *Helicobacter pylori*, *Infect. Immun.* *73*, 7252-7258.

12. Wolfram, L., Haas, E., and Bauerfeind, P. (2006) Nickel Represses the Synthesis of the Nickel Permease NixA of *Helicobacter pylori*, *J. Bacteriol.* 188, 1245-1250.
13. Davis, G. S., Flannery, E. L., and Mobley, H. L. T. (2006) *Helicobacter pylori* HP1512 is a nickel-responsive NikR-regulated outer membrane protein, *Infect. Immun.* 74, 6811-6820.
14. Delany, I., Ieva, R., Soragni, A., Hilleringmann, M., Rappuoli, R., and Scarlato, V. (2005) In Vitro Analysis of Protein-Operator Interactions of the NikR and Fur Metal-Responsive Regulators of Coregulated Genes in *Helicobacter pylori*, *J. Bacteriol.* 187, 7703-7715.
15. Ernst, F. D., Stoof, J., Horrevoets, W. M., Kuipers, E. J., Kusters, J. G., and van Vliet, A. H. M. (2006) NikR Mediates Nickel-Responsive Transcriptional Repression of the *Helicobacter pylori* Outer Membrane Proteins FecA3 (HP1400) and FrpB4 (HP1512), *Infect. Immun.* 74, 6821-6828.
16. Wisedchaisri, G., Holmes, R. K., and Hol, W. G. (2004) Crystal Structure of an IdeR-DNA complex reveals a conformational change in activated IdeR for base-specific interactions, *J Mol Biol* 342, 1155-1169.
17. Feese, M. D., Ingason, B. P., Goranson-Siekierke, J., Holmes, R. K., and Hol, W. G. (2001) Crystal structure of the iron-dependent regulator from *Mycobacterium tuberculosis* at 2.0-Å resolution reveals the Src homology domain3-like fold and metal binding function of the third domain, *J Biol Chem* 276, 5959-5966.
18. Pohl, E., Holmes, R. K., and Hol, W. G. (1998) Motion of the DNA-binding domain with respect to the core of the diphtheria toxin repressor (DtxR) revealed in the crystal structures of apo- and holo-DtxR, *J Biol Chem* 273, 22420-22427.
19. Pohl, E., Holmes, R. K., and Hol, W. G. (1999) Crystal structure of a cobalt-activated diphtheria toxin repressor-DNA complex reveals a metal-binding SH3-like domain, *J Mol Biol* 292, 653-667.
20. White, A., Ding, X., vanderSpek, J. C., Murphy, J. R., and Ringe, D. (1998) Structure of the metal-ion-activated diphtheria toxin repressor/tox operator complex, *Nature* 394, 502-506.
21. Lucarelli, D., Russo, S., Garman, E., Milano, A., Meyer-Klaucke, W., and Pohl, E. (2007) Crystal structure and function of the zinc uptake regulator FurB from *Mycobacterium tuberculosis*, *J Biol Chem* 282, 9914-9922.
22. Liu, T., Ramesh, A., Ma, Z., Ward, S. K., Zhang, L., George, G. N., Talaat, A. M., Sacchettini, J. C., and Giedroc, D. P. (2006) CsoR is a novel *Mycobacterium*



- tuberculosis* copper-sensing transcriptional regulator, *Nature Chemical Biology* 3, 60-68.
23. Hall, D. R., Gourley, D. G., Leonard, G. A., Duke, E. M., Anderson, L. A., Boxer, D. H., and Hunter, W. N. (1999) The high-resolution crystal structure of the molybdate-dependent transcriptional regulator (ModE) from *Escherichia coli*: a novel combination of domain folds, *Embo J* 18, 1435-1446.
  24. de Pina, K., Desjardin, V., Mandrand-Berthelot, M.-A., Giordano, G., and Wu, L. F. (1999) Isolation and Characterization of the *nikR* Gene Encoding a Nickel-Responsive Regulator in *Escherichia coli*, *J. Bacteriol.* 181, 670-674.
  25. Wang, S. C., Dias, A. V., Bloom, S. L., and Zamble, D. B. (2004) Selectivity of Metal Binding and Metal-Induced Stability of *Escherichia coli* NikR, *Biochemistry* 43, 10018-10028.
  26. Diederix, R. E. M., Fauquant, C., Rodrigue, A., Mandrand-Berthelot, M.-A., and Michaud-Soret, I. (2008) Sub-micromolar affinity of *Escherichia coli* NikR for Ni(II), *Chemical Communications* 15, 1813-1815.
  27. Bloom, S. L., and Zamble, D. B. (2004) Metal-Selective DNA-Binding Response of *Escherichia coli* NikR, *Biochemistry* 43, 10029-10038.
  28. Chivers, P. T., and Sauer, R. T. (1999) NikR is a ribbon-helix-helix DNA-binding protein, *Protein Sci.* 8, 2494-2500.
  29. Dias, A. V., and Zamble, D. B. (2005) Protease digestion analysis of *Escherichia coli* NikR: evidence for conformational stabilization with Ni(II), *J. Bio. Inorg. Chem.* 10, 605-612.
  30. Leitch, S., Bradley, M. J., Rowe, J. L., Chivers, P. T., and Maroney, M. J. (2007) Nickel-Specific Response in the Transcriptional Regulator, *Escherichia coli* NikR, *J. Am. Chem. Soc.* 129, 5085-5095.
  31. Schreiter, E. R., Sintchak, M. D., Guo, Y., Chivers, P. T., Sauer, R. T., and Drennan, C. L. (2003) Crystal structure of nickel-responsive transcription factor NikR, *Nat. Struct. Bio.* 10, 794-799.
  32. Schreiter, E. R., Wang, S. C., Zamble, D. B., and Drennan, C. L. (2006) NikR-operator complex structure and the mechanism of repressor activation by metal ions, *Proc. Natl. Acad. Sci. U. S. A.* 103, 13676-13681.
  33. Dian, C., Schauer, K., Kapp, U., McSweeney, S. M., Labigne, A., and Terradot, L. (2006) Structural Basis of the Nickel Response in *Helicobacter pylori*: Crystal Structures of HpNikR in Apo and Nickel-bound States, *J. Mol. Bio.* 361, 715-730.

34. Chivers, P. T., and Tahirov, T. H. (2005) Structure of *Pyrococcus horikoshii* NikR: Nickel Sensing and Implications for the Regulation of DNA Recognition, *J. Mol. Bio.* 348, 597-607.
35. Schreiter, E. R., and Drennan, C. L. (2007) Ribbon-helix-helix transcription factors: variations on a theme, *Nat Rev Microbiol* 5, 710-720.
36. Phillips, C. M., Schreiter, E. R., Guo, Y., Wang, S. C., Zamble, D. B., and Drennan, C. L. (2008) Structural Basis of the Metal Specificity for Nickel Regulatory Protein NikR, *Biochemistry* 47, 1938-1946.
37. Cui, G., and Kenneth M. Merz, J. (2008) The Intrinsic Dynamics and Function of Nickel Binding Regulatory Protein: Insights from Elastic Network Analysis, *The Biophysical Society* 94, 3769-3778.
38. Carrington, P. E., Chivers, P. T., Al-Mjeni, F., Sauer, R. T., and Maroney, M. J. (2003) Nickel coordination is regulated by the DNA-bound state of NikR, *Nat. Struct. Bio.* 10, 126-130.

## Chapter II: Structural Basis of the Metal Specificity for Nickel Regulatory Protein NikR

### II.A. Abstract

In the presence of excess nickel, *Escherichia coli* NikR regulates cellular nickel uptake by suppressing the transcription of the *nik* operon, which encodes for the nickel uptake transporter, NikABCDE. Previously published *in vitro* studies have shown that NikR is capable of binding a range of divalent transition metal ions in addition to Ni<sup>2+</sup>, including Co<sup>2+</sup>, Cu<sup>2+</sup>, Zn<sup>2+</sup>, and Cd<sup>2+</sup>. To understand how the high-affinity nickel binding site of NikR is able to accommodate these other metal ions, and to better understand NikR's mechanism of binding to DNA, we have determined structures of the metal-binding domain (MBD) of NikR in the apo form and in complex with Cu<sup>2+</sup> and Zn<sup>2+</sup> ions and compare them with the previously published structures with Ni<sup>2+</sup>. We observe that Cu<sup>2+</sup> ions bind in a very similar manner to Ni<sup>2+</sup>, with a square planar geometry but with longer bond lengths. Crystals grown in the presence of Zn<sup>2+</sup> reveal a protein structure similar to that of apo MBD with a disordered  $\alpha 3$  helix, but with two electron density peaks near the Ni<sup>2+</sup> binding site corresponding to two Zn<sup>2+</sup> ions. These structural findings along with biochemical data on NikR support a hypothesis that ordering of the  $\alpha 3$  helix is important for repressor activation.

This chapter was published in similar form in: Phillips, C.M., Schreiter, E.R., Wang, S.C., Zamble, D.B., and Drennan, C.L. Structural Basis of the Metal Specificity for Nickel Regulatory Protein NikR. *Biochemistry* **47**, 1938-1946 (2008).

## II.B. Introduction

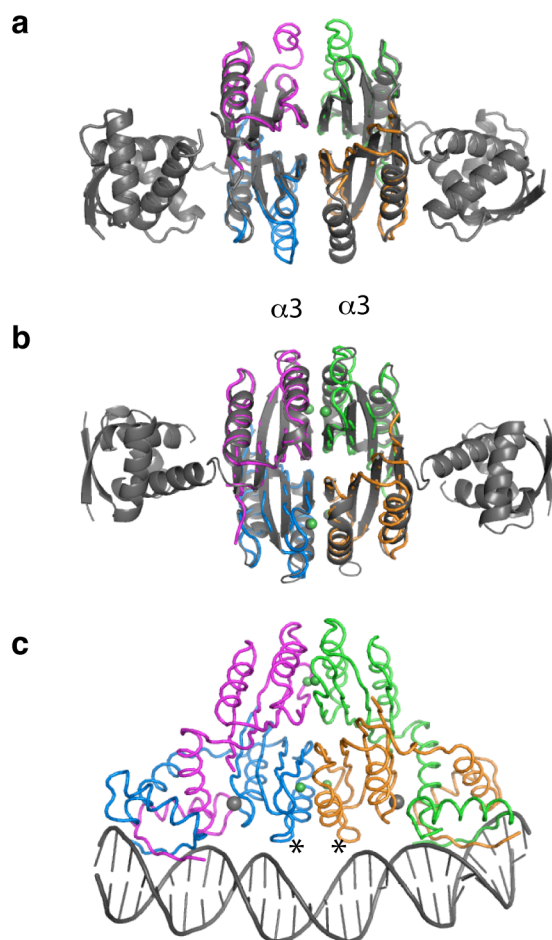
A number of microorganisms use nickel as an essential cofactor, including the extensively studied *Escherichia coli* and *Helicobacter pylori*. In *E. coli*, nickel is necessary under anaerobic conditions for proper functioning of hydrogenase (1). *H. pylori*, which colonize the acidic environment of the stomach, require the nickel-containing enzymes urease and hydrogenase to maintain a neutral pH within the cell and as an energy source, respectively (2, 3). An excess of nickel ions in either organism can lead to cell death (3, 4). Both organisms use the transcription factor NikR to inhibit the transcription of the nickel-uptake machine in the presence of surplus nickel (5, 6). In *E. coli*, this metal uptake machinery is an ABC-transporter (NikABCDE) (7), while in *H. pylori*, the monomeric metal-uptake protein, NixA is the key player (6). Although the apo form of NikR has no detectable affinity for DNA (8, 9), stoichiometric amounts of nickel induce a binding affinity of  $5 \times 10^{-9}$  M to the *nik* operon in *E. coli* (10) and  $5 \times 10^{-8}$  M to the *nixA* operon in *H. pylori* (11). In addition to controlling the transcription of NixA (6), NikR regulates a number of genes in *H. pylori*, including the urease accessory protein UreA (12) and outer membrane proteins FepA3 (13), FrpB4 (2, 13), and ExbB (14).

Despite the variety of metals in the cell, most metalloproteins bind a given metal with great specificity (15). The origin of this specificity remains an active area of research in the bioinorganic field. For NikR, *in vitro* spectroscopic studies and metal binding experiments seem to contradict this basic principle, as they indicate that NikR binds a number of transition metals including  $\text{Ni}^{2+}$ ,  $\text{Co}^{2+}$ ,  $\text{Zn}^{2+}$ ,  $\text{Cd}^{2+}$ , and  $\text{Cu}^{2+}$  with significant affinity (16). While nickel is best able to stabilize NikR (16-18), a number of different transition metal ions induce substantial DNA binding affinity to NikR (10). To investigate how different metals bind NikR and to explore the issue of specificity we have determined the structures of the *E. coli* NikR metal-binding domain (MBD) with  $\text{Zn}^{2+}$  and  $\text{Cu}^{2+}$  bound and with no metals bound.

Structures of NikR from *E. coli* (19, 20), *H. pylori* (21), and *Pyrococcus horikoshii* (22) have provided insight into the tertiary structure of the protein and the changes that occur upon nickel and DNA binding. NikR is a homotetrameric protein arranged with a central tetrameric MBD and two flanking dimeric DNA-binding ribbon-helix-helix (RHH) domains (Figure II.1). A

comparison between *E. coli* apo-NikR (PDB 1Q5V) and Ni<sup>2+</sup>-bound MBD and NikR structures (PDBs 1Q5Y and 2HZA) indicates that the  $\alpha 3$  helices of the MBD are flexible in the absence of nickel and become structured when nickel binds to the protein (19, 20). An array of structures of

**Figure II.1.** Structures of *E. coli* NikR. Each monomer composing the tetramer is a different color. (a) Alignment of apo-MBD (in color, this work) and apo full-length NikR (in grey, PDB 1Q5V). (b) Alignment of Ni<sup>2+</sup>-bound structures of MBD (in color, PDB 1Q5Y) and full-length NikR (in grey, PDB 2HZA). (c) DNA- and Ni<sup>2+</sup>-bound full-length NikR (PDB 2HZV). K<sup>+</sup>, which was observed bound in NikR-DNA structure, are represented by black spheres. Asterisks indicate loops and  $\alpha 3$  helices that make connections to the DNA.



Ni<sup>2+</sup>-NikR from each of the organisms listed above (20-22) compared to the one structure of NikR bound to DNA (20) illustrate that the RHH domains are not pre-arranged into the correct

DNA-binding configuration upon nickel binding (Figure II.1). Only in the presence of DNA are both RHH domains oriented “down” in a productive DNA binding configuration. In this “down” DNA-binding configuration in *E. coli*, a second metal-binding site, occupied by  $K^+$  in the crystal structure, is formed at the interface of the RHH and MBD (20). Binding of a cation such as  $K^+$  to this site may serve to help lock NikR onto its DNA operator (20).

We have previously proposed that the MBD  $\alpha 3$  helices play an important role in the metal-dependent response of NikR for DNA (19, 20). Here we test this hypothesis by examining whether metals yielding high NikR-DNA affinity indeed stabilize the  $\alpha 3$  helix. The structures we describe here, in combination with previously published biochemical studies, lead to a mechanism for NikR-DNA binding.

## II.C. Results

### II.C.1. Full Length versus MBD NikR Structures.

The isolated MBD of NikR is a simple model system that can be used to study the structural consequences of transition metal ion binding to the protein. The MBD construct of NikR (residues 48-133) contains the residues involved in high-affinity metal binding, but lacks the N-terminal ribbon-helix-helix (RHH) DNA binding domains. The MBD domain retains all key metal-binding features of the full-length NikR while crystallizing much more readily. The isolated MBD is tetrameric and has identical topology to the MBD portion of the full-length NikR protein (Figure II.1). The RMSD for structural alignment of  $Ni^{2+}$ -MBD (PDB 1Q5Y) (19) and full-length  $Ni^{2+}$ -NikR (PDB 2HZA) (20) is 0.89 Å for 321  $C_a$  atoms and 1.13 Å for all 2387 common atoms. Similarly, the apo-MBD aligns with the previously described apo-NikR (PDB 1Q5V) (19) with an RMSD of 0.67 Å for 261  $C_a$  atoms and 0.96 Å for all 1910 common atoms. All structural alignments and RMSD calculations were done in LSQMAN (23).

### II.C.2. Metal-Binding Sites.

The previous crystal structure of  $Ni^{2+}$ -MBD (PDB 1Q5Y) (19) shows that nickel binds in a square planar geometry at the interface between two subunits of the NikR tetramer, and is coordinated by H87, H89, and C95 of one monomer and H76 of a neighboring monomer (Figure

II.2a). The  $\text{Cu}^{2+}$ -MBD structure described here illustrates that copper binds with the same square planar geometry and ligands as nickel (Figure II.2b), with slightly longer metal-ligand distances than in the  $\text{Ni}^{2+}$ -MBD structure (Table II.1). The two distances that lengthen the most are from residues directly opposite each other (H89 and C95), creating a slightly asymmetric square planar site.

**Figure II.2.** Metal binding sites with  $2F_o-F_c$  electron density (blue) contoured at  $1\sigma$  around metal and ligands. One monomer is in magenta and the other in green. (a)  $\text{Ni}^{2+}$ -MBD, (b)  $\text{Cu}^{2+}$ -MBD, (c)  $\text{Zn}^{2+}$ -MBD. The dispersive difference map (orange) was calculated by subtracting data collected at  $1.2829 \text{ \AA}$  (zinc inflection wavelength) from  $1.00 \text{ \AA}$  (a remote wavelength) and indicates the presence of zinc, contoured at  $-8.0 \sigma$ . (d)  $\text{Zn}^{2+}$ -MBD with  $F_o-F_c$  difference density maps around the zinc binding sites with positive difference electron density in green contoured at  $+3\sigma$  and negative difference electron density in red contoured at  $-3\sigma$ .

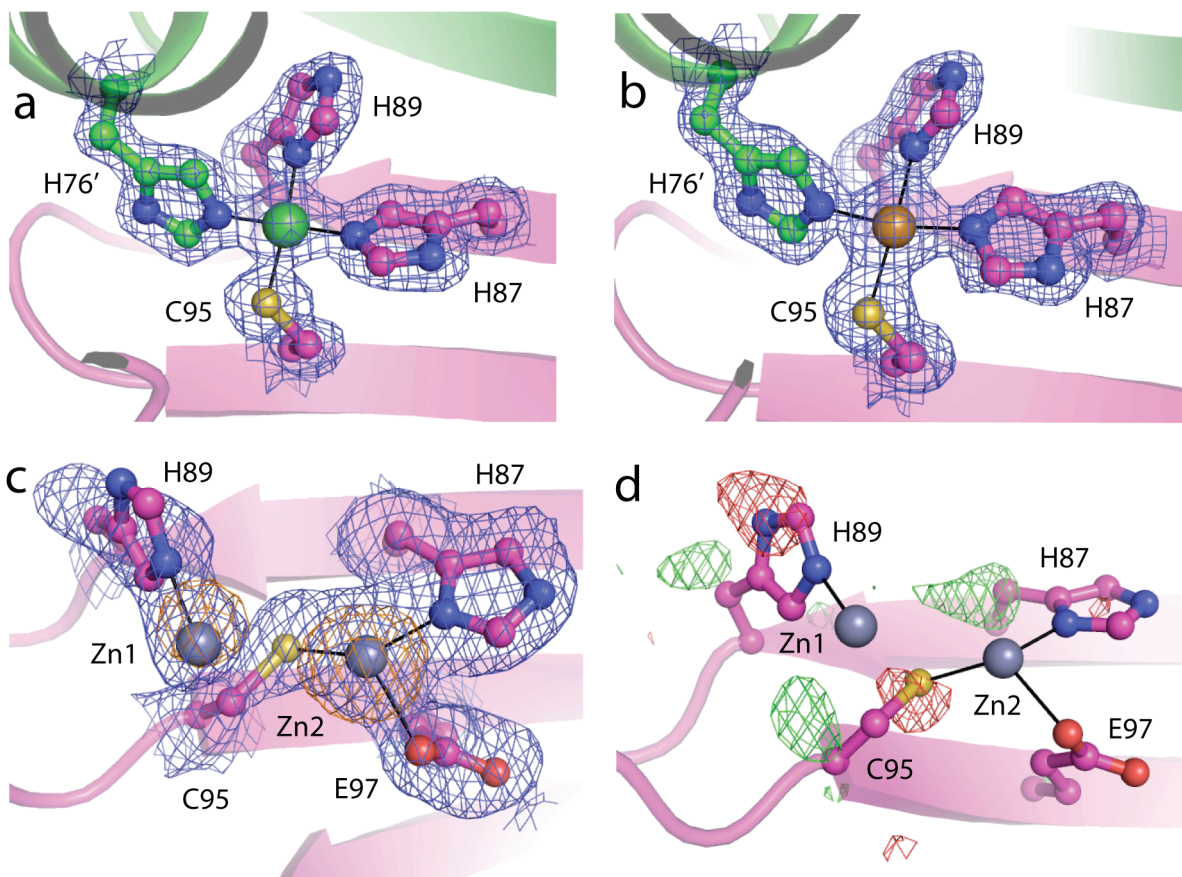


**Table II.1.** Distances and angles around the metals in the metal-bound MBD structures. Distances and angles were averaged over the four monomers of the Ni<sup>2+</sup> and Cu<sup>2+</sup>-bound structures. The numbers in parentheses refer to the last digits of the mean and represent the standard deviation of the measurement.

	Ni-MBD	Cu-MBD	Zn1	Zn2
M-H76' (Å)	1.85(7)	2.00(5)		
M-H87 (Å)	1.94(5)	2.09(6)		1.99
M-H89 (Å)	2.01(4)	2.40(2)	2.21	
M-C95 (Å)	2.22(3)	2.43(3)		2.32
M-E97 (Å)				2.34
H76'-M-C95 (°)	88(2)	94(4)		
H76'-M-H87 (°)	175(2)	164(7)		
H76'-M-H89 (°)	88(2)	76(16)		
C95-M-H87 (°)	93(1)	99(3)		131
C95-M-H89 (°)	175(2)	170(3)		
H87-M-H89 (°)	91(1)	84(5)		
H87-M-E97 (°)				90
C95-M-E97 (°)				120

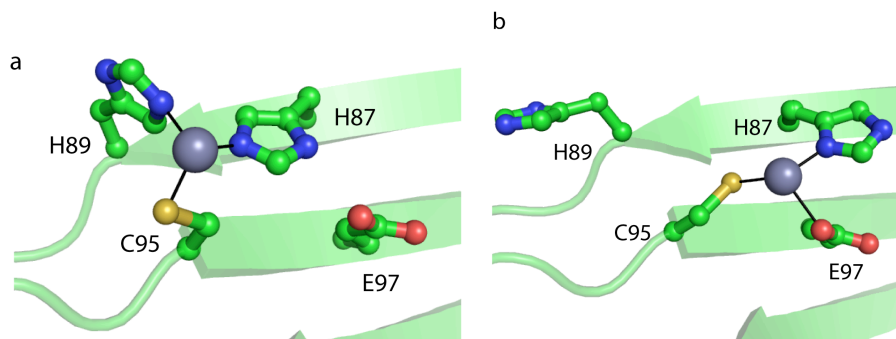
The protein used for crystallization contained one Zn<sup>2+</sup> ion per MBD monomer, yet two zinc binding sites were detected in each monomer through dispersive difference electron density maps (Figure II.2c). After refinement of the protein structure, the occupancies of the zinc sites were refined in CNS (24) while restraining the B-factors of the zinc ions to values similar to the surrounding ligands. This refinement provided occupancies for the two zinc sites of 25% and 57%. It should be noted that the refinement of occupancies in this manner is not quantitative as we had to estimate the B-factors of the metals ions based on those of surrounding residues, and were not able to refine B-factors and occupancies simultaneously at this resolution. While the relative occupancy values are meaningful, the total occupancy is less so.

Zinc binding sites are located in the same region of the MBD as the copper and nickel sites, and use three of the same ligands (Figure II.2c). Approximately 25% of the monomers in the crystal have Zn in zinc site Zn1, located near H89 (Figure II.3a). Closer to 57% of the monomers in the



crystal have Zn coordinated by residues C95, E97, and H87 in zinc site Zn2 (Figure II.3b). Both Zn1 and Zn2 are poor zinc binding sites with only 1 or 3 ligands in our structure ordered for coordination, respectively. Zinc ions prefer a tetrahedral environment (25) and neither site has 4

**Figure II.3.** Two monomer “states” in the Zn-MBD crystal. (a) The Zn1 (less prevalent site) is occupied in about 25% of all monomers of the crystal and is ligated by H89, H87, and C95. (b) The Zn2 (more prevalent site) is occupied is about 57% of monomers in the crystal and is ligated by H87, C95, and E97. The occupancies are estimates based on refinement with fixed B-factors. Figures 2c and 2d show the observed average site. Here we show the two main components that comprise the average.

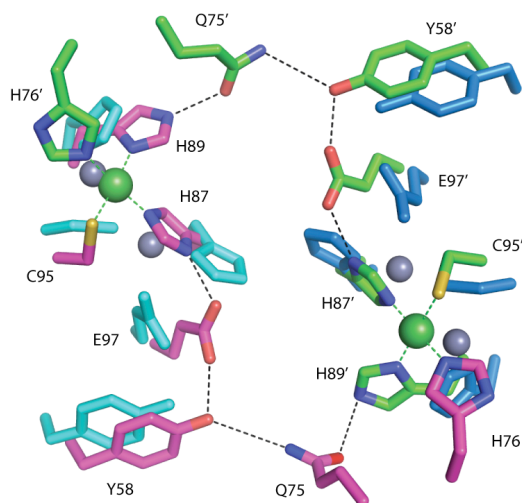


ligands or angles befitting a tetrahedral geometry (Table II.1). Water molecules (or another small ligand), which should be visible at 1.9 Å resolution, are not indicated by the presence of positive  $F_o-F_c$  density near either zinc ion. In addition, H76 from  $\alpha 3$ , which ligates both nickel and copper from a neighboring MBD monomer, is disordered and cannot be modeled in the zinc structure. Even the residues that can be modeled at these sites are not well ordered as indicated by the presence of both positive and negative  $F_o-F_c$  difference electron density around these residues (Figure II.2d). Since the electron density observed is an average of all molecules in the crystal, it is likely that residues H87, H89, and C95 adopt different conformations in molecules that have Zn in site Zn1 than in molecules that have Zn in site Zn2, as indicated by the positive and negative difference electron density shown in Figure II.2d. The dominant conformation of the residues is the one that provides better coordination of Zn2 as shown in Figure II.2c and

Figure II.3b. The minor conformation in the crystal, where zinc is bound at Zn1, is shown in Figure II.3a.

The nickel (19) and copper structures maintain two hydrogen bonding networks that each connect two of the four metal binding sites in the tetrameric MBD. This network stretches across the MBD interface and includes two residues from the  $\alpha 3$  helix, but the network is not ordered in the apoNikR (19) or apoMBD structures. Thus, this network could be involved in stabilizing both helix  $\alpha 3$  and the overall structure of NikR for DNA binding. In contrast to  $\text{Ni}^{2+}$ - and  $\text{Cu}^{2+}$ -MBD structures, this hydrogen bonding network is greatly disturbed in the  $\text{Zn}^{2+}$ -MBD structure (Figure II.4).

**Figure II.4.** Hydrogen bonding network connecting two nickel binding sites.  $\text{Zn}^{2+}$ -MBD colored in cyan and blue aligned to the  $\text{Ni}^{2+}$ -MBD structure with carbon atoms in green and magenta, oxygen in red, sulfur in yellow, and nitrogen in blue.



### II.C.3. Alpha 3 Helix.

The  $\alpha 3$  helix, residues 65-78, (Figure II.1b,c) has been implicated in the mechanism of NikR binding to DNA, due to the fact that nickel binding orders this helix and that there are contacts made by residues of this helix and the preceding loop to DNA (Figure II.1c) (20). Therefore, it

is important to consider each metal's ability to order the  $\alpha 3$  helix. The  $\text{Ni}^{2+}$ -MBD and  $\text{Cu}^{2+}$ -MBD structures have fully-ordered  $\alpha 3$  helices (Figure II.5a,b; Figure II.6), with B-factors of the amino acids very similar to those in the rest of the structure (Table II.2). The alignment of  $\text{Ni}^{2+}$ -MBD with  $\text{Cu}^{2+}$ -MBD indicates no significant change in the overall structure, with an RMSD of only 0.47 Å for all 2469 atoms in the copper and nickel structures.

**Figure II.5.** Ordering of the  $\alpha 3$  helix. Ribbon diagrams of the (a)  $\text{Ni}^{2+}$ -MBD, (b)  $\text{Cu}^{2+}$ -MBD, (c)  $\text{Zn}^{2+}$ -MBD, (d) apo-MBD; with each monomer represented in a separate color. (e) Circular dichroism spectra of apo-,  $\text{Ni}^{2+}$ -,  $\text{Cu}^{2+}$ -, and  $\text{Zn}^{2+}$ -MBD.

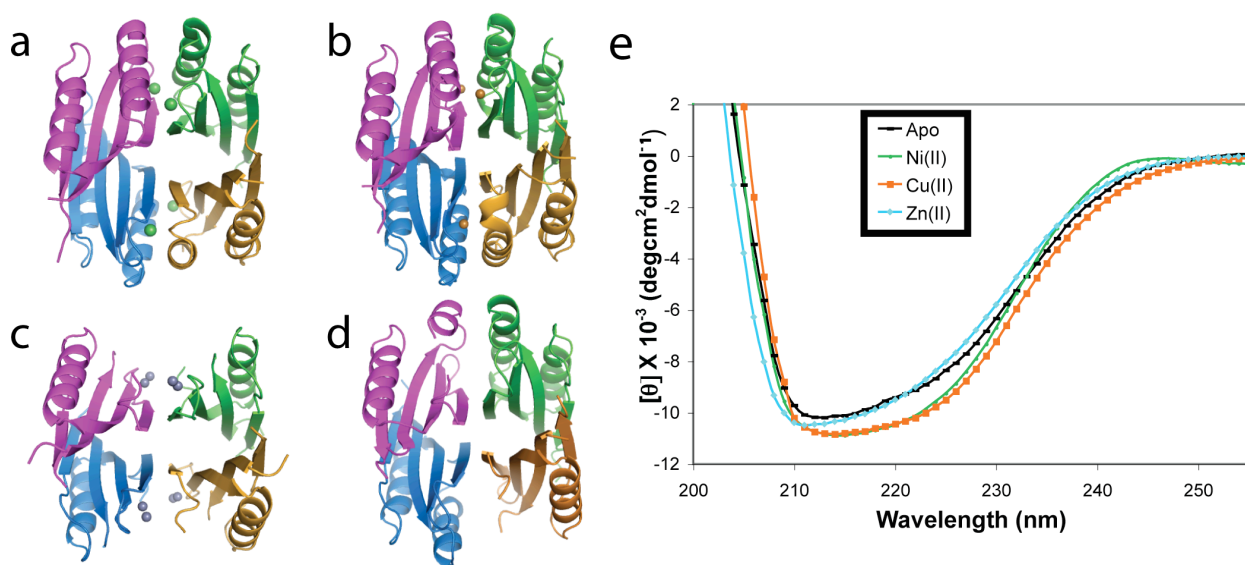


**Table II.2.** Average B-factors (in Å<sup>2</sup>) for different portions of the apo,  $\text{Zn}^{2+}$ -,  $\text{Cu}^{2+}$ -, and  $\text{Ni}^{2+}$ -bound MBD structures.

	Apo-MBD	$\text{Zn}^{2+}$ -MBD	$\text{Cu}^{2+}$ -MBD	$\text{Ni}^{2+}$ -MBD (19)
Overall Structure	62.2	45.1	21.0	28.0
Protein	62.3	44.6	20.6	26.8
$\alpha 3$ Helix <sup>a</sup> (Res. 65-78)	87.7	97.8	25.2	32.7
Metals	-	47.6	23.9	19.1
Metal Ligands	-	42.2	18.9	22.0
Water	51.7	60.7	27.1	39.3

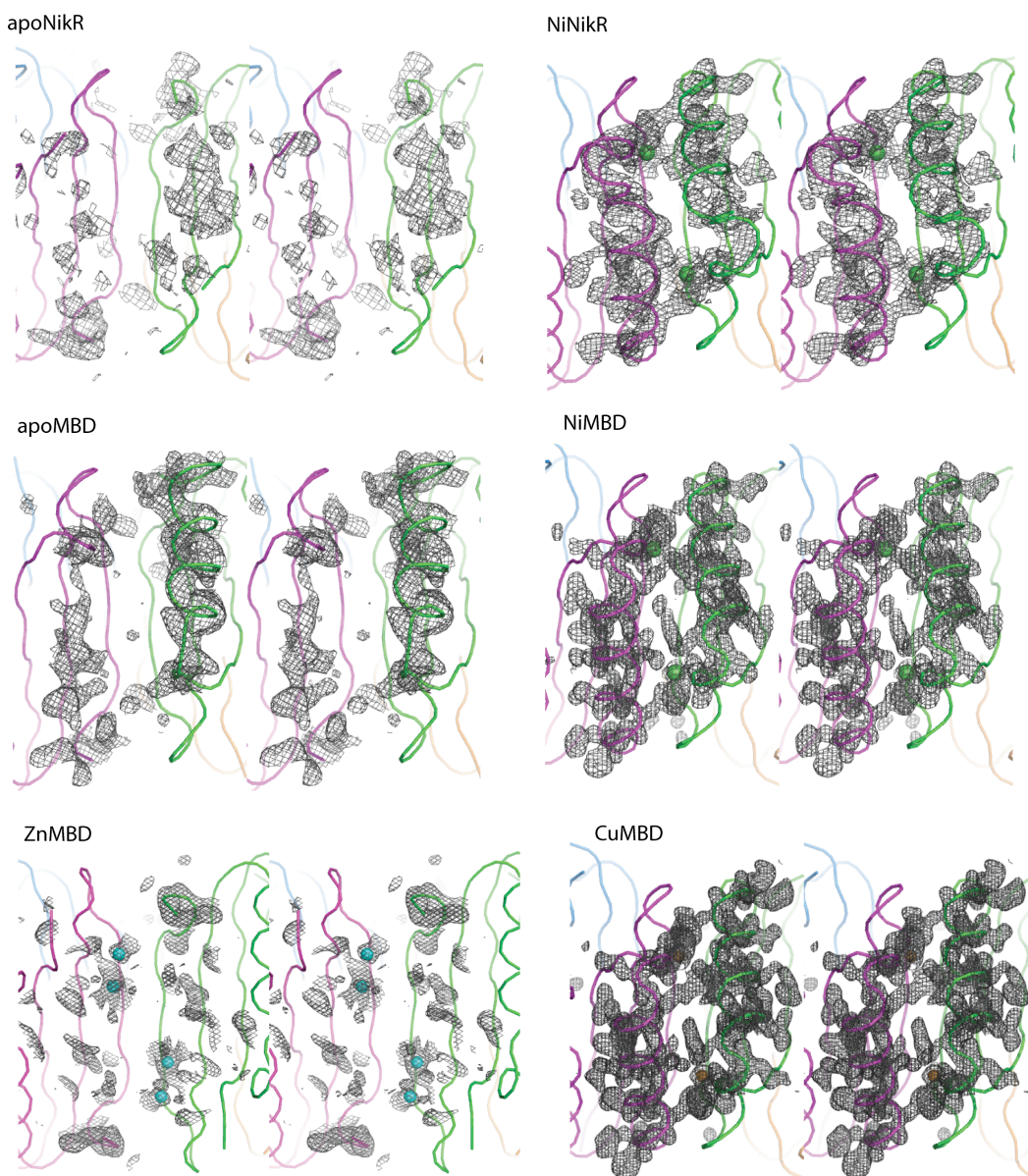
<sup>a</sup> The B-factor for the Zn structure is an average following a single round of refinement when the  $\alpha 3$  helix was modeled into the structure.

The  $\alpha 3$  helix in the  $\text{Zn}^{2+}$ -MBD structure, however, is disordered and untraceable in the electron density map (Figure II.5c, Figure II.6). When helix  $\alpha 3$  is modeled into the  $\text{Zn}^{2+}$ -MBD structure there are large regions of the helix in negative  $F_o-F_c$  difference electron density, insufficient  $2F_o-F_c$  density, and higher atomic B-factors than in the rest of the protein (Table II.2, Figure II.5). Therefore, residues 62-78 were omitted from the  $\text{Zn}^{2+}$ -MBD structure. The RMSD for 66  $C_\alpha$  atoms in the  $\text{Zn}^{2+}$ -MBD and  $\text{Ni}^{2+}$ -MBD monomers is 1.24 Å, and 1.98 Å for all 491 identical atoms, much higher than for  $\text{Cu}^{2+}$ -MBD compared to  $\text{Ni}^{2+}$ -MBD.

Similar to the full-length apo-NikR structure, the apo-MBD structure (Figure II.5d) has poorly ordered  $\alpha 3$  helices (Figure II.6). When modeled into the structure, the helices do not refine well in 2 of the 4 monomers, have insufficient  $2F_o-F_c$  density, high B-factors, and are therefore either modeled as incomplete helices (monomer A) or are entirely omitted (monomer D). In no case is there sufficient density to model the sidechains of any  $\alpha 3$  helix residue longer than alanine or serine. When the apo-MBD structure is aligned to the  $\text{Ni}^{2+}$ -MBD structure, the RMSD for 305  $C_\alpha$  atoms is 1.40 Å.

Circular dichroism was used to confirm differences in a helical character of the MBD between the apo and metal-bound forms in solution (Figure II.5e). Calculated from the ellipticity of each complex at 222 nm, the  $\text{Ni}^{2+}$ - and  $\text{Cu}^{2+}$ -MBD have approximately 9% more alpha-helicity than the apo- and  $\text{Zn}^{2+}$ -MBD forms (Figure II.5e, see II.E.5 for details). A fully formed  $\alpha 3$  helix would represent about 50% of the helicity for the MBD. Thus, a decrease of 9% helicity suggests that in solution some but not all of the  $\alpha 3$  helix is disordered in apo- and  $\text{Zn}^{2+}$ -MBD. This result is consistent with the broken electron density and high B-factors for residues in the  $\alpha 3$  helices of these structures.

**Figure II.6.** One sigma  $2F_o - F_c$  electron density around the area of the  $\alpha 3$  helix calculated with phases from the final refined structure. Wall-eyed stereo images. Monomers are colored separately and two of the four monomers in the apoNikR, apoMBD, ZnMBD, NiNikR, NiMBD, and CuMBD structures are shown. Nickel ions are in green, copper ions in orange, and zinc ions in aqua spheres. Splotchy or poor density in the apoNikR, apoMBD, and ZnMBD structures indicated disordered helices in the crystal, while in the Ni- and Cu-bound forms the helices are well ordered with complete electron density for the helices.



## II.D. Discussion

NikR's nickel-specific response in binding the *nik* operon suggests that the protein would be similarly specific to binding nickel over other metals. However, *in vitro* studies have shown that a number of metals are able to bind NikR, some with affinities similar to those of nickel (16). The measured binding affinities using competition assays for copper, nickel, and zinc to full length NikR are,  $1 \times 10^{-17}$ ,  $9 \times 10^{-13}$ , and  $<1 \times 10^{-12}$  M, respectively (16). These comparable affinities raise the questions of how NikR specifically responds to nickel within the cell. The data presented here allow us to discuss how a metal's ability to order the  $\alpha 3$  helix corresponds to its ability to increase NikR's affinity for DNA.

### II.D.1. Metal binding to NikR.

EXAFS and XANES studies by the Maroney laboratory have indicated that  $\text{Ni}^{2+}$  and  $\text{Cu}^{2+}$  ions bind to NikR in square-planar environments (18). The known  $\text{Ni}^{2+}$ -MBD and full-length  $\text{Ni}^{2+}$ -NikR structures are consistent with this geometry, and now we show that  $\text{Cu}^{2+}$  also binds in the same site as  $\text{Ni}^{2+}$  with the same ligands and a nearly identical coordination environment (Figure II.2). The  $\text{Cu}^{2+}$ -MBD has slightly longer metal-ligand bond distances than the distances in the  $\text{Ni}^{2+}$ -MBD structure (Table II.1), also consistent with the trend observed through the EXAFS studies where the metal- $\text{N}_{\text{imd}}$  distances were measured as 1.905 Å and 1.928 Å and metal-S distances as 2.130 Å and 2.210 Å for nickel and copper, respectively (18). The absolute values measured from the crystallographic data tend to be longer (Ni-S 2.22 Å; Cu-S 2.43 Å, Ni- $\text{N}_{\text{imd}}$  1.93 Å, Cu- $\text{N}_{\text{imd}}$  2.16 Å).

The  $\text{Zn}^{2+}$  sites observed in our structure are partially occupied and the ligands to the metals are highly flexible. The zinc XANES data have been modeled in terms of a single  $\text{Zn}^{2+}$  ion bound to NikR with four coordinating ligands, interpreted as a tetrahedral coordination environment (18), which is common for divalent zinc ions. We do not observe a tetrahedral site nor can we imagine a ligand rearrangement that would allow for a tetrahedral geometry (see angles in Table II.1 and Figure II.2c). Reported distances from EXAFS are 2.229 Å for the Zn-S bond and 1.990 Å for the Zn- $\text{N}_{\text{imd}}$  bonds (18). Crystallographic metal-ligand distances are similar but again somewhat longer (we find 2.32 Å for Zn-S and 2.18 Å for Zn-N/O on average). We also

observe four unique ligands to the zinc ions, three of which are N/O donors and one that is a S-donor, again consistent with the EXAFS data (18). Re-evaluation of the  $Zn^{2+}$  EXAFS data using our model would determine if the zinc data can be fit as well to a partially occupied dinuclear zinc model as it can to a single tetrahedral zinc site.

#### II.D.2. Ordering of the $\alpha 3$ helix is metal-dependent.

The initial structures of *E. coli* NikR provided insight into the structural changes nickel induces upon binding to the apo protein (19, 20). In apo-NikR, three of the four  $\alpha 3$  helices are disordered and not traceable in the electron density maps (residues 62-77) (Figure II.6). The  $Ni^{2+}$ -bound MBD and full-length NikR structures have complete electron density for all  $\alpha 3$  helices with B-factors similar to the rest of the protein (Table II.2). Divalent nickel and copper bind tightly to NikR and both are able to order the  $\alpha 3$  helix, while divalent zinc binds less tightly and is incapable of ordering the  $\alpha 3$  helix (Figures 5 and 6). Circular dichroism experiments (Figure II.5e) also indicate that the  $Zn^{2+}$ - and apo-MBD complexes contain less  $\alpha$ -helicity than the  $Cu^{2+}$ - and  $Ni^{2+}$ -MBD complexes. In addition, examination of the RMSDs between different structures indicate that apo and  $Zn^{2+}$ -MBD are similar to each other, while the  $Ni^{2+}$ - and  $Cu^{2+}$ -MBD structures are structurally homologous (Table II.3).

**Table II.3.** Root-mean-squared deviations (RMSDs) between the  $C_{\alpha}$  atoms in apo and metal-bound MBD NikR structures in Å. The number of aligned atoms is in parentheses.

	Apo MBD	$Zn^{2+}$ MBD	$Ni^{2+}$ MBD	$Cu^{2+}$ MBD
Apo MBD	-	1.18 (65)	1.40 (305)	1.43 (305)
$Zn^{2+}$ MBD	1.18 (65)	-	1.24 (66)	1.20 (66)
$Ni^{2+}$ MBD	1.40 (305)	1.24 (66)	-	0.22 (321)
$Cu^{2+}$ MBD	1.43 (305)	1.20 (66)	0.22 (321)	-

Our results are consistent with previous experiments investigating the stability of the protein in the presence of different metals. In proteolysis experiments, nickel, and copper to a lesser extent, are able to stabilize residues 66-133, which includes the  $\alpha 3$  helix, protecting them from

proteolysis, while zinc offers no (or little) protection (17). Chemical and thermal stability assays indicate that nickel-bound NikR requires a larger amount of guanidine HCl or a higher temperature to be denatured in comparison to any other metal-bound NikR, though copper did stabilize the protein more than zinc (16). Hydrogen-deuterium exchange experiments indicate that when nickel or copper are bound to the protein the exchange rate is much slower than when zinc or no metal is bound, which the authors relate to the ordering of the  $\alpha 3$  helix (18).

An obvious difference between the  $Zn^{2+}$ /apo and the  $Cu^{2+}/Ni^{2+}$  structures is the disorder of H76, a residue in  $\alpha 3$ , which is involved in metal ligation in the  $Cu^{2+}/Ni^{2+}$  structures. In  $Cu^{2+}$ - and  $Ni^{2+}$ -bound MBD, H76 bridges the tetrameric interface by becoming the fourth ligand of the square planar metal site. It is our proposal that nickel and copper's ability to ligate this residue and in turn "tie down" the  $\alpha 3$  helix and its preceding loop is related to the ability of  $Ni^{2+}$ - and  $Cu^{2+}$ -bound NikR to bind DNA. The hydrogen bonding network across the tetrameric interface in the MBD formed only in presence of  $Ni^{2+}$  and  $Cu^{2+}$  may also be responsible for inducing some ordering of the  $\alpha 3$  helix (Figures 4 and 5). The disruption of this hydrogen bonding network in the apo or  $Zn^{2+}$ -bound NikR forms could play a role in determining the overall flexibility of the  $\alpha 3$  helix observed crystallographically and by circular dichroism.

### *II.D.3. Ordering of $\alpha 3$ helix is linked to DNA binding.*

Ordering of the  $\alpha 3$  helix and the loop preceding it (loop 64-65) has previously been implicated in the mechanism of NikR binding to DNA (19, 20). The structure of  $Ni^{2+}$ -NikR-DNA illustrates an interaction between the MBD and backbone phosphates on the DNA (marked with \* in Figure II.1c). Some of the residues of the MBD that make these contacts are in loop 64-65, which, along with the  $\alpha 3$  helix, is disordered in the absence of  $Ni^{2+}$ . The structures of apo-,  $Zn^{2+}$ -, and  $Cu^{2+}$ -MBD in combination with previously solved structures and DNA-binding data provide further evidence that the ordering of the  $\alpha 3$  helix is an important step in NikR's recognition of DNA.

*In vitro* DNA foot printing and mobility shift assays indicate that although  $Cu^{2+}$ ,  $Ni^{2+}$ ,  $Zn^{2+}$ ,  $Co^{2+}$ , and  $Cd^{2+}$  are capable of inducing some DNA binding,  $Cu^{2+}$  and  $Ni^{2+}$  are the most efficient (10).



$\text{Cu}^{2+}$ - and  $\text{Ni}^{2+}$ -bound NikR have nanomolar affinity to the *nik* operon, while  $\text{Zn}^{2+}$ -NikR has a binding affinity two orders of magnitude less for the operon (10). *In vivo*, LacZ reporter assays indicate that only nickel and not Mn, Fe, Co, Cu, or Zn is capable of repressing transcription of the *nik* operon (18). While the inability of copper to repress transcription *in vivo* is seemingly inconsistent with the DNA-binding and structural data, these latter results are for  $\text{Cu}^{2+}$ , not  $\text{Cu}^+$ , which is the form of copper that would be most abundant in the cell (26, 27). While specificity of a nickel-regulatory protein for nickel makes logical sense, if there is no free  $\text{Cu}^{2+}$  in the cell there would be no evolutionary pressure for NikR to have evolved such that  $\text{Cu}^{2+}$  wouldn't activate it (26, 27).

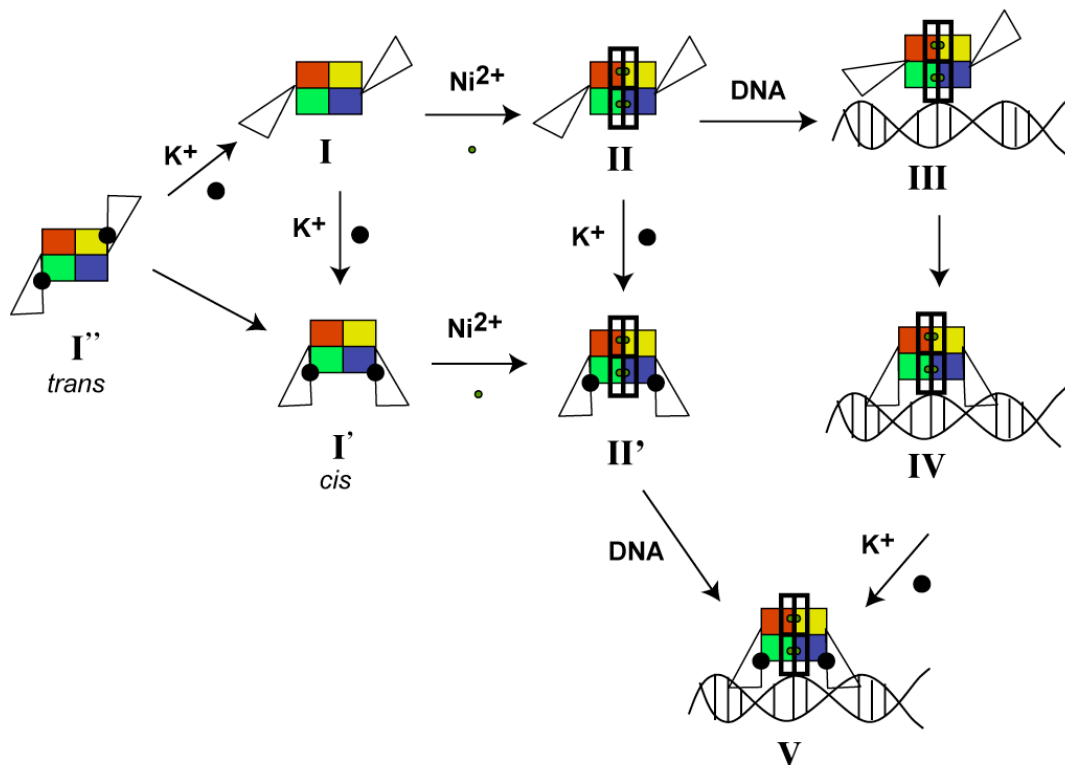
#### *II.D.4. Mechanism of NikR binding to DNA.*

The data presented here along with previous studies suggest that there are at least three factors that are likely important in forming a stable complex between NikR and the *nik* operator DNA with stoichiometric nickel present: (1) hydrogen bonding and electrostatic interactions formed between MBD and DNA upon  $\alpha 3$  ordering; (2) the proper orientation of the RHH domains “down” such that residues of this domain can make specific contacts to DNA; and (3) the binding of  $\text{K}^+$ , or a similar cellular abundant cation, to a site between the RHH domains and MBD, stabilizing the RHH domain in a “down”, cis DNA-binding orientation. It should be noted that one turn of helix  $\alpha 2$  of the RHH domain must unwind for the “down” RHH conformation to be obtained (20, 22). It has been reported that with excess nickel NikR binds DNA with greater affinity (8, 10). Whether this greater affinity is due to a specific low affinity nickel site in NikR or to a general electrostatic effect is unknown. It is also not known if this ‘low affinity’ nickel effect is physiologically relevant. For further discussion and possible identifications of these excess nickel binding sites, see Chapter IV of this thesis. For simplicity, here we will only consider the mechanistic situation for NikR with stoichiometric nickel and with a second metal cation like  $\text{K}^+$ . For further discussion of the second metal binding site or  $\text{K}^+$  site see Chapter III of this thesis and for more on the excess nickel binding site see Chapter IV.

Figure II.7 shows many possible DNA binding pathways, but the process most likely to occur in the cell on a regular basis consists of steps **I** to **V**.  $\text{Ni}^{2+}$  binds to the high-affinity site of NikR,

stabilizing the  $\alpha 3$  helix and its preceding loop (**I**  $\rightarrow$  **II**). The NikR molecule makes initial contacts to DNA, stabilized via hydrogen bonds and electrostatic interactions between residues in the loop of the MBD and the phosphate backbone (**II**  $\rightarrow$  **III**). The conformationally flexible DNA-binding RHH domains are then capable of finding their binding sites in the major grooves of the DNA, enforcing contacts between the NikR molecule and DNA (**III**  $\rightarrow$  **IV**). Finally, an abundant intracellular metal ion such as potassium binds at the interface of the MBD and RHH domains, serving to stabilize this NikR configuration (**IV**  $\rightarrow$  **V**).

**Figure II.7.** Proposed NikR regulatory mechanism. Dimeric RHH domains are represented by white triangles, each monomer of the MBD is represented in a different color, bold empty rectangles represent an ordered  $\alpha 3$  helix, nickel ions are represented by green circles outlined in black, and potassium ions are represented in large black spheres.



There are a few pieces of structural, biochemical, and computational evidence for the necessity of K<sup>+</sup> in NikR-DNA binding. In the initial NikR-DNA crystal structure we saw extra electron density at the interface of the MBD and RHH domains ligated by unconserved backbone

carbonyls from the MBD and conserved amino acids E30 and D34 from the RHH domain (20). Nickel anomalous maps indicated this atom was not nickel and modeling  $K^+$  in this site left no unaccounted for electron density. In addition, recent biochemical work in the Zamble laboratory at the University of Toronto illustrates that NikR requires  $K^+$  ions for DNA binding (personal communication). Finally, work described in Chapter III of this thesis explains the physical reasons for  $K^+$  ion preference at this site.

With respect to the role of  $K^+$  in the mechanism presented in Figure II.7, we believe the affinity of NikR for  $K^+$  should be greater in the NikR-DNA complex where the RHH are stably positioned near the MBD (Figure II.7, IV). In the absence of DNA, RHH domains are highly mobile and  $K^+$  binding sites only exist transiently when the RHH domains sample cis (I') or trans (I'') conformations. Thus, while  $K^+$  may bind weakly to multiple forms of NikR (I', I'', II' in Figure II.7), high occupancy of  $K^+$  is likely only in the NikR-DNA state (V). Again, it is not known if the RHH domain or MBD binds DNA first, but we find it easiest to think about the MBD making the first contacts. The interactions between residues in the MBD with backbone phosphates in the DNA are not specific but could initially localize NikR to DNA while the protein searches for the ideal binding site. With NikR localized on DNA, the floppy RHH domains will occasionally sample a “down” conformation and when they do, they will make specific contacts to DNA when the correct operator sequence is available. The fact that apo-NikR does not bind DNA with measurable affinity suggests that if the RHH domains bind first, they would have weak affinity until a metal-ordered MBD is also stably bound to DNA.

#### *II.D.5. Conclusions.*

To control nickel concentrations in the cell, Nature developed a transcription factor both flexible enough to bind two half sites separated by two turns of DNA and conformationally regulated by the binding of nickel. Interestingly, the only conformational change observed upon  $Ni^{2+}$  binding is the ordering of  $\alpha 3$  and its preceding loop (20-22), the RHH domains remain flexible (20-22). To prevent untimely repression of the *nik* operon, it is important that NikR be highly responsive toward nickel ions, but not be activated by other intracellular transition metals. Divalent copper is the only metal known to induce DNA-binding affinities *in vitro* equivalent to that of nickel.

Current research suggests that any free copper in the cell is reduced to  $\text{Cu}^+$  (26, 27), which would negate any evolutionary pressure for NikR to be able to distinguish between  $\text{Ni}^{2+}$  and  $\text{Cu}^{2+}$ . Unlike  $\text{Cu}^{2+}$ , there is a significant amount of  $\text{Zn}^{2+}$  within the cell, although the amount of free zinc may be small. While  $\text{Zn}^{2+}$  can bind NikR with some affinity, it does not induce the ordering of the  $\alpha 3$  helix, and  $\text{Zn}^{2+}$ -NikR's affinity to DNA is decreased compared to  $\text{Ni}^{2+}$ -NikR. Here we illustrate a correlation between the ability of a metal to order the  $\alpha 3$  helix and that metal's ability to induce DNA binding, and use this information along with previous results to describe a mechanism for NikR binding to DNA.

## II.E. Methods

### II.E.1. Structure determination of apo-MBD NikR.

MBD NikR was over-expressed and purified with nickel bound as described previously (19). Nickel was removed from the sample by incubation with 10 mM EDTA (representing a 10-fold molar excess over MBD) at 4°C for 48 hours. The sample changed color from light yellow to colorless. To remove Ni-EDTA and excess EDTA, the sample was passed twice through Micro Bio-Spin P-6 columns (Bio-Rad).

Apo-MBD was crystallized using the hanging drop technique in a drop containing 1.5 ml of 10 mg/ml apo-MBD in buffer (20 mM Tris pH 8.0, 300 mM NaCl) and 1.5 ml of precipitant solution (0.2 M sodium tartrate, 20% w/v PEG 3350) at room temperature. Colorless, plate-shaped crystals were cryoprotected in precipitant solution containing 30% ethylene glycol.

Data were collected on beamline X12-B at the National Synchrotron Light Source, Brookhaven National Laboratory at 100 K with an oscillation step size of  $0.5^\circ$  per frame, data collection statistics in Table II.4. Reliable reflections were collected to 2.1 Å and reduced using DENZO/SCALEPACK (28).

**Table II.4.** Data collection and refinement statistics.<sup>a</sup>

Crystal	Apo-MBD	Cu <sup>2+</sup> -MBD	Zn <sup>2+</sup> -MBD	
			Inflection	Remote
Space Group	C2	P2 <sub>1</sub> 2 <sub>1</sub> 2 <sub>1</sub>	P6 <sub>2</sub> 22	P6 <sub>2</sub> 22
Cell Dimensions				
a (Å)	67.35	45.95	46.22	46.27
b (Å)	59.67	78.44	-	-
c (Å)	75.14	81.46	124.90	125.05
β (°)	94.01	-	-	-
Wavelength (Å)	1.100	0.9791	1.2829	1.0
Resolution Range (Å)	50-2.1 (2.18-2.10)	50-1.5 (1.55-1.5)	40-1.9 (2.0-1.9)	28.9-1.9 (1.9-2.0)
Unique Reflections	17408 (1685)	46684 (4006)	6755 (957)	6765 (965)
Average Redundancy	7.3 (2.6)	8.1 (6.1)	9.8 (6.0)	11.0 (11.4)
Completeness (%)	99.5 (96.7)	97.9 (85.2)	99.5 (99.6)	99.6 (100)
<i>I</i> / σ( <i>I</i> )	17.8 (1.7)	16.9 (5.3)	28.1 (3.4)	30.6 (5.7)
<i>R</i> <sub>sym</sub> (%) <sup>b</sup>	6.9 (45.1)	5.7 (25.4)	5.2 (34.5)	5.1 (35.6)
<i>R</i> <sub>cryst</sub> ( <i>R</i> <sub>free</sub> ) (%) <sup>c</sup>	28.8 (33.5)	19.5 (22.7)	24.9 (27.3)	
Number of protein atoms	2262	2618	509	
Number of metal ions	0	4	2	
Number of water molecules	15	171	22	
R.m.s. deviations				
Bond lengths (Å)	0.008	0.011	0.005	
Bond angles (°)	1.53	1.35	1.1	
Ramachandran (%)				
Most favored	81.3	92.2	92.9	
Additionally Allowed	18.7	7.8	5.4	
Generously Allowed	0.0	0.0	1.8	
Disallowed	0.0	0.0	0.0	

<sup>a</sup>The number in parentheses is for the highest resolution shell.

<sup>b</sup> $R_{\text{sym}} = \sum_{hkl} |I_{(hkl)}^i - \langle I_{(hkl)} \rangle| / \sum_{hkl} \langle I_{(hkl)} \rangle$ , where  $I_{(hkl)}^i$  is the  $i^{\text{th}}$  measured diffraction intensity and  $\langle I_{(hkl)} \rangle$  is the mean of the intensity for the miller index ( $hkl$ ).

<sup>c</sup> $R_{\text{work}} = \sum_{hkl} ||F_o(hkl)| - |F_c(hkl)|| / \sum_{hkl} |F_o(hkl)|$ .  $R_{\text{free}} = R_{\text{cryst}}$  for a test set of reflections (5%) not included in refinement.

The structure of apo-MBD was solved by molecular replacement in the program EPMR (29) using the protein component of the Ni<sup>2+</sup>-MBD structure as a model (PDB ID: 1Q5Y) (19). The structure was refined in CNS (24) with model rebuilding and adjustments made in Xfit (30) or Coot (31) to a final  $R_{\text{work}} = 28.8\%$  and  $R_{\text{free}} = 33.5\%$ , with refinement statistics in Table II.4.

Residues 72-78 of chain A and 64-79 in chain D were not observed in electron density maps and are therefore not present in the final model.

### *II.E.2. Structure determination of Cu<sup>2+</sup>-MBD NikR.*

Apo-MBD NikR was obtained as described above. Cu<sup>2+</sup> was added by slow addition with vortex mixing of a 50 mM CuCl<sub>2</sub> stock solution until a stoichiometry of 1.2:1 CuCl<sub>2</sub>:MBD was reached. Upon addition of CuCl<sub>2</sub>, the sample became a dark yellow-orange color. Cu<sup>2+</sup>-MBD was crystallized in the same form and under the same conditions as Ni<sup>2+</sup>-MBD, the structure of which is published (PDB ID: 1Q5Y) (19). Briefly, 1.5  $\mu$ L of 10 mg/mL Cu<sup>2+</sup>-MBD in 300 mM NaCl, 20 mM Tris, pH 8.0 was mixed with 1.5  $\mu$ L of 0.2 M disodium tartrate dehydrate, 20% w/v PEG 3350 in a hanging-drop vapor diffusion experiment at room temperature. Deep yellow-orange crystals appeared within 2-4 days.

Crystals were cryoprotected by briefly soaking in a precipitant solution with 20% ethylene glycol. A dataset was collected on beamline 8-BM of the Advanced Photon Source, Argonne National Lab, at 100 K to 1.5 Å resolution (Table II.4). Data were reduced using DENZO/SCALEPACK (28).

Crystals of Ni<sup>2+</sup>-MBD and Cu<sup>2+</sup>-MBD were isomorphous, so the protein component of the Ni<sup>2+</sup>-MBD structure (1Q5Y) was used directly as a starting model for refinement. Refinement was carried out in Refmac 5 from the CCP4 program suite (32). Rigid body refinement of the MBD tetramer and individual subunits was followed by rounds of positional and B-factor refinement and manual refitting of the model in Xfit (30). After refinement of anisotropic thermal displacement parameters and addition of hydrogens in their riding positions,  $R_{\text{work}} = 19.5\%$  and  $R_{\text{free}} = 22.7\%$  (Table II.4). The final model contains residues 50-132 of NikR. One molecule of the tetramer is missing residues 64-66, which were not clearly observed in the electron density maps.

### *II.E.3. Structure determination of Zn<sup>2+</sup>-MBD NikR.*

Apo MBD was produced as described above and Zn<sup>2+</sup> ions were added to the protein from a stock of 20 mM Zn-NTA complex to avoid MBD precipitation. The protein was allowed to equilibrate overnight at 4 degrees and then was desalted by passing through a Micro Bio-Spin P-6 column (Bio-Rad) to remove NTA. The final Zn:MBD ratio was 1:1 as confirmed spectrophotometrically with 4-(2-pyridylazo)resorcinol (PAR) (16). Crystals were obtained by mixing 1.5  $\mu$ L Zn<sup>2+</sup>-MBD solution (5 mg/mL MBD in 300 mM NaCl, 20 mM Tris, pH 8.0) with 1.5  $\mu$ L of precipitant (0.1 M Bis-Tris pH 5.5-6.5, 0.2 M (NH<sub>4</sub>)<sub>2</sub>SO<sub>4</sub>, and 25% w/v PEG 3350) in a hanging drop vapor diffusion experiment at room temperature. Colorless hexagonal crystals with dimensions 140 $\times$ 80 $\times$ 80  $\mu$ m grew in 2-5 days. Three brief, consecutive soaks in solutions of increasing ethylene glycol concentration (5%-12%-20%) were performed to prevent the crystals from cracking during cryoprotection.

A dataset was collected on the Zn<sup>2+</sup>MBD crystals at the Stanford Synchrotron Radiation Laboratory (SSRL) in Palo Alto, CA, on beam line 9-2 at 100 K at both the zinc inflection wavelength (1.2829  $\text{\AA}$ ) and a remote wavelength (1.00  $\text{\AA}$ ). Crystals diffracted to 1.9  $\text{\AA}$  and data were integrated in MOSFLM (33) and scaled in Scala (34).

The protein crystallized as a tetramer as in all other NikR structures, but with one molecule of MBD per asymmetric unit (asu) instead of the typical four. The whole protein component of one MBD monomer from the Ni<sup>2+</sup>-MBD structure (1Q5Y) was used as a search model for molecular replacement using PHASER (35). A good solution was found in P6<sub>2</sub>22 (Z-score of 24) and was refined in CNS (24) against the inflection wavelength (1.2829  $\text{\AA}$ ) dataset by rigid body refinement followed by simulated annealing. The  $\alpha$ 3 helix of the MBD is mostly disordered, as in the apo-MBD and apo-NikR (1Q5V) (19) structures. This helix was removed from the model and alternating cycles of positional and B-factor refinement with manual refitting in Coot (31) were carried out. The final model refined to an R<sub>work</sub> of 24.9% and R<sub>free</sub> of 27.3%, and includes one subunit of the MBD NikR (residues 50-61 and 80-130), 22 water molecules, and two zinc ions (Table II.4). All structures were validated using composite omit maps generated in CNS (24) and examined in Xfit (30) or Coot (31).

#### *II.E.4. Criteria for including $\alpha 3$ in model.*

NikR crystal structures sometimes show little or no electron density in the region of helix  $\alpha 3$  (Figure II.6). In some cases, we have left some or all residues in the  $\alpha 3$  helix out of the final coordinates due to a lack of confidence about the positioning of these atoms. Our criteria for deeming  $\alpha 3$  too disordered to model are as follows: (1) B-factors are  $25 \text{ \AA}^2$  or more higher for  $\alpha 3$  residues than for the rest of the structure; (2) 50% or more of the  $C_\alpha$  atoms are not in  $2F_o-F_c$  density following a few rounds of refinement; (3) more negative  $F_o-F_c$  density is around this portion of the structure than is typical; (4) composite omit map density is missing for more than 50% of the helical atoms.

#### *II.E.5. Circular dichroism of $Ni^{2+}$ , $Cu^{2+}$ , $Zn^{2+}$ , and Apo-MBD.*

The MBD of NikR was expressed and purified on a  $Ni^{2+}$ -NTA column (Qiagen, Valencia, CA), followed by incubation with EDTA and anion exchange chromatography, as previously described (8, 16). An assay with Ellman's reagent and  $\beta$ -mercaptoethanol as a standard was used to confirm that the MBD was fully reduced, and an HPLC assay was used to confirm that the protein was apo (36). Circular dichroism spectra were collected on a Jasco model J-710 spectropolarimeter in a cylindrical cell of 0.1 cm optical path length over a wavelength range from 260 to 195 nm at room temperature, as previously described (16). Each CD spectrum was the average of five accumulations at a scanning speed of 50 nm/min, a 1.0 nm spectral band width, a data pitch of 0.1 nm, and a 4 s response time. The experiments were performed by using protein stocks dialyzed against 10 mM HEPES, 100 mM KCl, pH 7.6, at concentrations ranging from 5 to 40  $\mu$ M. For experiments performed in the presence of metal, the protein was first incubated overnight with stoichiometric amounts of metal sulfate at room temperature. The concentrations of the holo-protein stocks were verified by diluting the protein in 6 M GuHCl and EDTA and measuring the absorbance at 280 nm, using the calculated extinction coefficient of  $2680 \text{ M}^{-1}\text{cm}^{-1}$  (37). Following data collection, the absorbance at 220 nm was analyzed to determine the percent helicity of each structure using Equation 1.

$$\text{(Equation 1) } \% \text{ alpha-helix} = [(-\theta_{222\text{nm}} + 3000)/39000] \times 100$$

where  $\theta_{222\text{nm}}$  is the mean residue ellipticity at 222nm (38-40).



## **II.F. Acknowledgements**

Eric Schreiter grew the Cu<sup>2+</sup>-MBD and apo-MBD crystals, collected data, and did initial data processing on these data sets. Portions of this research were carried out at the Stanford Synchrotron Radiation Laboratory (SSRL), a national user facility operated by Stanford University on behalf of the U.S. Department of Energy, Office of Basic Energy Sciences. The SSRL Structural Molecular Biology Program is supported by the Department of Energy, Office of Biological and Environmental Research, and by the National Institutes of Health, National Center for Research Resources, Biomedical Technology Program, and the National Institute of General Medical Sciences. Use of the Advanced Photon Source (Contract No. DE-AC02-06CH11357) and the National Synchrotron Light Source at Brookhaven National Laboratory (Contract No. DE-AC02-98CH10886) was supported by the U.S. Department of Energy, Office of Science, and Office of Basic Energy Sciences.

## II.G. References

1. Unden, G., and Bongaerts, J. (1997) Alternative respiratory pathways of *Escherichia coli*: energetics and transcriptional regulation in response to electron acceptors, *Biochim. Biophys. Acta* 1320, 217-234.
2. Davis, G. S., Flannery, E. L., and Mobley, H. L. T. (2006) *Helicobacter pylori* HP1512 is a nickel-responsive NikR-regulated outer membrane protein, *Infect. Immun.* 74, 6811-6820.
3. Mulrooney, S. B., and Hausinger, R. P. (2003) Nickel uptake and utilization by microorganisms, *FEMS Microbiol. Rev.* 27, 239-261.
4. Wu, L. F., Navarro, C., de Pina, K., Quenard, M., and Mandrand, M. A. (1994) Antagonistic Effect of Nickel on the Fermentative Growth of *Escherichia coli* K-12 and Comparison of Nickel and Cobalt Toxicity on the Aerobic and Anaerobic Growth, *Environ. Health* 102, 297-300.
5. de Pina, K., Desjardin, V., Mandrand-Berthelot, M.-A., Giordano, G., and Wu, L. F. (1999) Isolation and Characterization of the *nikR* Gene Encoding a Nickel-Responsive Regulator in *Escherichia coli*, *J. Bacteriol.* 181, 670-674.
6. Wolfram, L., Haas, E., and Bauerfeind, P. (2006) Nickel Represses the Synthesis of the Nickel Permease NixA of *Helicobacter pylori*, *J. Bacteriol.* 188, 1245-1250.
7. Navarro, C., Wu, L. F., and Mandrand-Berthelot, M.-A. (1993) The *nik* operon of *Escherichia coli* encodes a periplasmic binding-protein-dependent transport system for nickel., *Mol. Microbiol.* 9, 1181-1191.
8. Chivers, P. T., and Sauer, R. T. (2000) Regulation of high affinity nickel uptake in bacteria. Ni<sup>2+</sup>-Dependent interaction of NikR with wild-type and mutant operator sites, *J. Biol. Chem.* 275, 19735-19741.
9. Chivers, P. T., and Sauer, R. T. (2002) NikR Repressor: High-Affinity Nickel Binding to the C-Terminal Domain Regulates Binding to Operator DNA, *Chem. Biol.* 9, 1141-1148.
10. Bloom, S. L., and Zamble, D. B. (2004) Metal-Selective DNA-Binding Response of *Escherichia coli* NikR, *Biochemistry* 43, 10029-10038.
11. Benanti, E. L., and Chivers, P. T. (2007) The N-terminal Arm of the *Helicobacter pylori* Ni<sup>2+</sup>-dependent Transcription Factor NikR Is Required for Specific DNA Binding, *J. Biol. Chem.* 282, 20365-20375.
12. Ernst, F. D., Kuipers, E. J., Heijens, A., Sarwari, R., Stoof, J., Penn, C. W., Kusters, J. G., and van Vliet, A. H. M. (2005) The Nickel-Responsive Regulator NikR controls Activation and Repression of Gene Transcription in *Helicobacter pylori*, *Infect. Immun.* 73, 7252-7258.

13. Ernst, F. D., Stoof, J., Horrevoets, W. M., Kuipers, E. J., Kusters, J. G., and van Vliet, A. H. M. (2006) NikR Mediates Nickel-Responsive Transcriptional Repression of the *Helicobacter pylori* Outer Membrane Proteins FecA3 (HP1400) and FrpB4 (HP1512), *Infect. Immun.* *74*, 6821-6828.
14. Delany, I., Ieva, R., Soragni, A., Hilleringmann, M., Rappuoli, R., and Scarlato, V. (2005) In Vitro Analysis of Protein-Operator Interactions of the NikR and Fur Metal-Responsive Regulators of Coregulated Genes in *Helicobacter pylori*, *J. Bacteriol.* *187*, 7703-7715.
15. Pennella, M. A., Shokes, J. E., Cosper, N. J., Scott, R. A., and Giedroc, D. P. (2003) Structural elements of metal selectivity in metal sensor proteins, *Proc. Natl. Acad. Sci. U. S. A.* *100*, 3713-3718.
16. Wang, S. C., Dias, A. V., Bloom, S. L., and Zamble, D. B. (2004) Selectivity of Metal Binding and Metal-Induced Stability of *Escherichia coli* NikR, *Biochemistry* *43*, 10018-10028.
17. Dias, A. V., and Zamble, D. B. (2005) Protease digestion analysis of *Escherichia coli* NikR: evidence for conformational stabilization with Ni(II), *J. Bio. Inorg. Chem.* *10*, 605-612.
18. Leitch, S., Bradley, M. J., Rowe, J. L., Chivers, P. T., and Maroney, M. J. (2007) Nickel-Specific Response in the Transcriptional Regulator, *Escherichia coli* NikR, *J. Am. Chem. Soc.* *129*, 5085-5095.
19. Schreiter, E. R., Sintchak, M. D., Guo, Y., Chivers, P. T., Sauer, R. T., and Drennan, C. L. (2003) Crystal structure of nickel-responsive transcription factor NikR, *Nat. Struct. Bio.* *10*, 794-799.
20. Schreiter, E. R., Wang, S. C., Zamble, D. B., and Drennan, C. L. (2006) NikR-operator complex structure and the mechanism of repressor activation by metal ions, *Proc. Natl. Acad. Sci. U. S. A.* *103*, 13676-13681.
21. Dian, C., Schauer, K., Kapp, U., McSweeney, S. M., Labigne, A., and Terradot, L. (2006) Structural Basis of the Nickel Response in *Helicobacter pylori*: Crystal Structures of HpNikR in Apo and Nickel-bound States, *J. Mol. Bio.* *361*, 715-730.
22. Chivers, P. T., and Tahirov, T. H. (2005) Structure of *Pyrococcus horikoshii* NikR: Nickel Sensing and Implications for the Regulation of DNA Recognition, *J. Mol. Bio.* *348*, 597-607.
23. Kleywegt, G. J., and Jones, T. A. (1994) A super position, *CCP4/ESF-EACBM Newsletter Protein Crystallography* *31*, 9-14.
24. Brünger, A. T., Adams, P. D., Clore, G. M., DeLano, W. L., Gros, P., Grosse-Kunstleve, R. W., Jiang, J. S., Kuszewski, J., Nilges, M., Pannu, N. S., Read, R. J., Rice, L. M.,

- Simonson, T., and Warren, G. L. (1998) Crystallography & NMR system (CNS): A new software suite for macromolecular structure determination, *Acta Crystallogr. D54*, 905-921.
25. Rulisek, L., and Vondrasek, J. (1998) Coordination geometries of selected transition metal ions ( $\text{Co}^{2+}$ ,  $\text{Ni}^{2+}$ ,  $\text{Cu}^{2+}$ ,  $\text{Zn}^{2+}$ ,  $\text{Cd}^{2+}$ , and  $\text{Hg}^{2+}$ ) in metalloproteins, *J. Inorg. Biochem.* *71*, 115-127.
  26. Finney, L. A., and O'Halloran, T. V. (2003) Transition metal speciation in the cell: insights from the chemistry of metal ion receptors, *Science* *300*, 931-936.
  27. Rosenzweig, A. C. (2001) Copper delivery by metallochaperone proteins, *Acc. Chem. Res.* *34*, 119-128.
  28. Otwinowski, Z., and Minor, W. (1997) Processing of X-ray Diffraction Data Collected in Oscillation Mode, *Methods Enzymol.* *276: Macromolecular Crystallography, part A*, 307-326.
  29. Kissinger, C. R., Gehlhaar, D. K., and Fogel, D. B. (1999) Rapid automated molecular replacement by evolutionary search, *Acta Crystallogr. D55*, 484-491.
  30. McRee, D. E. (1999) XtalView/Xfit - A Versatile Program for Manipulating Atomic Coordinates and Electron Density, *J. Struct. Bio.* *125*, 156-165.
  31. Emsley, P., and Cowtan, K. (2004) Coot: model-building tools for molecular graphics., *Acta Crystallogr. D60*, 2126-2132.
  32. Collaborative Computational Project, N. (1994) The CCP4 Suite: Programs for Protein Crystallography, *Acta Crystallogr. D50*, 760-763.
  33. Leslie, A. G. W. (2005) MOSFLM, 6.2.5 ed., Cambridge, UK.
  34. Evans, P. (2006) Scala, 3.2.5 ed., Cambridge, UK.
  35. Storoni, L. C., McCoy, A. J., and Read, R. J. (2004) Likelihood-enhanced fast rotation functions, *Acta Crystallographica, Section D D60*, 432-438.
  36. Atanassova, A., Lam, R., and Zamble, D. B. (2004) A high-performance liquid chromatography method for determining transition metal content in proteins, *Anal. Biochem.* *335*, 103-111.
  37. Gill, S. C., and von Hippel, P. H. (1989) Calculation of protein extinction coefficients from amino acid sequence data, *Anal. Biochem.* *182*, 319-326.
  38. Greenfield, N. J., and Fasman, G. D. (1969) Computed circular dichroism spectra for the evaluation of protein conformation, *Biochemistry* *8*, 4108-4116.

39. Morrisett, J. D., David, J. S. K., Pownall, H. J., and Gotto, A. M. (1973) Interaction of an apolipoprotein (apoLP-alanine) with phosphatidylcholine, *Biochemistry* 12, 1290 - 1299.
40. Taylor, J. W., and Kaiser, E. T. (1987) Structure-function analysis of proteins through the design, synthesis, and study of peptide models, *Methods Enzymol.* 154, 473-498.



## Chapter III: Physical Basis of Metal-Binding Specificity in *Escherichia coli* NikR

### III.A. Abstract

In *Escherichia coli* and other bacteria, nickel uptake is regulated by the transcription factor NikR. Nickel binding at high affinity sites in *E. coli* NikR (*EcNikR*) facilitates *EcNikR* binding to the *nik* operon, where it then suppresses transcription of genes encoding the nickel uptake transporter, NikABCDE. A structure of the *EcNikR*-DNA complex suggests that a second metal binding site is also present when NikR binds to the *nik* operon. Moreover, this co-crystal structure raises the question of what metal occupies the second site under physiological conditions:  $K^+$ , which is present in the crystal structure, or  $Ni^{2+}$ , which has been proposed to bind to low as well as high affinity sites on *EcNikR*. To determine which ion is preferred at the second metal binding site and the physical basis for any preference of one ion over another in both the second metal binding site and the high affinity sites, we conducted a series of detailed molecular simulations on the *EcNikR* structure. Simulations that place  $Ni^{2+}$  at high affinity sites lead to stable trajectories with realistic ion-ligand distances and geometries while simulations that place  $K^+$  at these sites lead to conformational changes in the protein that are likely unfavorable for ion binding. By contrast, simulations on the second metal site in *EcNikR*-DNA complex lead to stable trajectories with realistic geometries regardless of whether  $K^+$  or  $Ni^{2+}$  occupies this site. Electrostatic binding free energy calculations, however, suggest that *EcNikR* binding to DNA is more favorable when the second metal binding site contains  $K^+$ . An analysis of the energetic contributions to the electrostatic binding free energy suggests that while the interaction between *EcNikR* and DNA is more favorable when the second site contains  $Ni^{2+}$ , the large desolvation penalty associated with moving  $Ni^{2+}$  from solution to the relatively buried second site offsets this favorable interaction term. Additional free energy simulations that account for both electrostatic and non-electrostatic effects argue that *EcNikR* binding to DNA is most favorable when the second site contains a monovalent ion the size of  $K^+$ . Taken together, these data suggest that the *EcNikR* structure is most stable when  $Ni^{2+}$  occupies high affinity sites and that *EcNikR* binding to DNA is more favorable when the second site contains  $K^+$ .

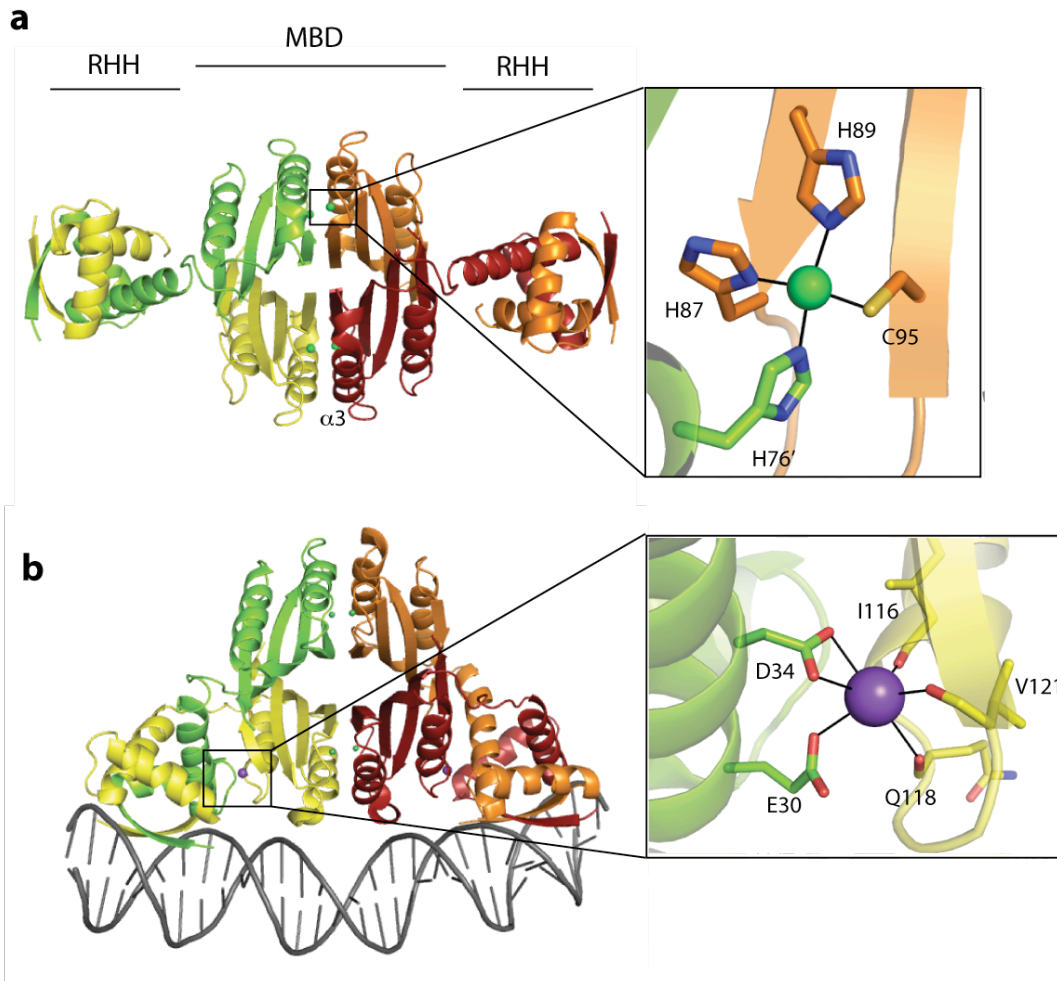
### III.B. Introduction

Monitoring the concentration of metal ions within the cell is of crucial importance, as a relatively small concentration of some metal ions is necessary for a number of cellular processes to occur, but often too much of that same ion may cause cell damage and death (1-4). Nickel is an essential cofactor for a number of bacterial enzymes that are involved in cell survival, including hydrogenase and urease – two enzymes vital to the survival of the pathogenic bacteria *Helicobacter pylori* (1). The concentration of nickel in many bacteria is regulated by the nickel-binding transcription factor, NikR, which transcriptionally represses genes encoding nickel-specific importers (5).

The best characterized NikR homologs are from *E. coli* (*EcNikR*), *H. pylori* (*HpNikR*), and *Pyrococcus horikoshi* (*PhNikR*) (6-9). Each is a homotetramer composed of two domains; the central tetrameric metal-binding domain (MBD) and two flanking dimeric ribbon-helix-helix (RHH) domains (Figure III.1a). The MBD is composed of C-terminal residues 48-133 (*E. coli* numbering) and each monomer contains a single high affinity square-planar nickel-binding site composed of H87, H89, and C95 from one monomer and H76 from a neighboring monomer (Figure III.1a). The RHH DNA binding portion of the protein is composed of residues 1-47 and is arranged in a common DNA binding motif such that the N-terminal ribbons from two monomers create a two-stranded  $\beta$  sheet that inserts into the major groove of DNA. The RHH domains are separated from the MBD by flexible linkers and crystal structures have captured the RHH in a number of different arrangements with respect to the MBD, suggesting that the RHH domains are free to move with respect to the MBD (8, 9). However, the relevant DNA-binding conformation for the RHH domains appears to be a “down-cis” arrangement as seen in the *EcNikR*-DNA crystal structure (Figure III.1b) (9). In addition, two identical second metal binding sites are formed when NikR assumes a “down-cis” arrangement and are located at the interface of the RHH and MBD domains (Figure III.1b). These second metal binding sites are composed of two conserved amino acid residues from the RHH domain, E30 and D34, and a number of backbone carbonyls from residues in the MBD (Figure III.1b) (9).



**Figure III.1.** Crystal structures of *EcNikR* and the metal binding sites. Each of the four monomers is colored individually and nickel ions are represented with green spheres and potassium ions with purple spheres. (a)  $\text{Ni}^{2+}$ -bound *EcNikR* (PDB 2HZA) and the square-planar high affinity nickel binding site. (b) *EcNikR*-DNA complex (PDB 2HZV) and the second metal binding site with potassium bound in an octahedral geometry.



Biochemical data and crystal structures of various NikR proteins have informed as well as raised interesting questions regarding these metal binding sites. The high affinity metal binding sites have been well characterized as nickel binding sites, which upon nickel binding induce a conformational change allowing NikR to bind DNA (10, 11). Interestingly, nickel binding does not appear to affect the conformation of the RHH DNA binding domains that make specific

contacts to DNA, instead altering the structure of the MBD that makes nonspecific DNA contacts (Figure III.1) (9). In particular, Ni<sup>2+</sup> binding orders the  $\alpha$ -helix 3 through its coordination of helical residue H76; conversely, H76 and  $\alpha$ -helix 3 are disordered in the apo *EcNikR* structure (8).

Crystallographic and mutagenesis data suggest that like *NikR*'s high affinity site, the second metal binding sites are also important in modulating the affinity of *NikR* for DNA (9). The location of these sites at the interface of the MBD and RHH domains suggests that a metal in this site would stabilize the “down-cis” or the DNA-binding mode of *EcNikR*. Although there has been general agreement that these sites are functionally important, opinions have varied about which metal is likely to occupy them *in vivo*, with the contenders being Ni<sup>2+</sup> and K<sup>+</sup> (6, 9). The suggestion that Ni<sup>2+</sup> occupies these second sites comes from biochemical as well as crystallographic data. In particular, metal binding studies have shown that the affinity of *EcNikR* for DNA increases from nanomolar, when stoichiometric Ni<sup>2+</sup> ions are bound to the high affinity nickel binding sites, to picomolar, when excess nickel is present (11, 12). This increased DNA binding affinity with excess nickel suggests the presence of one or multiple low-affinity Ni<sup>2+</sup> binding sites on *EcNikR*. The idea that one of these low-affinity sites could be the second metal site is supported by crystallographic data on *PhNikR* (6, 9). Here, however, the high concentration of Ni<sup>2+</sup> used (20 mM) and the need for phosphate in the crystallization conditions raises questions about the physiological relevance of these structural data. In addition, crystallographic data on *EcNikR* do not support the idea that Ni<sup>2+</sup> binds in the second metal sites, instead showing multiple low-affinity sites of the surface of the *EcNikR* protein (9).

The suggestion that K<sup>+</sup> might be the relevant metal in the second metal binding sites also comes from both biochemical and structural data. Sheila Wang and Deborah Zamble have recently shown that K<sup>+</sup> is required for *EcNikR*-DNA binding under both stoichiometric and excess nickel conditions (13). The localization of this K<sup>+</sup> effect to the second metal binding sites is derived from the structure of the *EcNikR*-DNA complex, in which a K<sup>+</sup> ion from the crystallization buffer is modeled in this site (9). Although the binding of ions from the crystallization buffer is often an artifact, in this case the concentration of K<sup>+</sup> in the crystallization buffer (200 mM) is

slightly lower than that in *E. coli* (250 mM), indicating that the presence of  $K^+$  in the second metal binding sites of this structure could be physiologically relevant (9, 14). If these second metal binding sites are  $K^+$  sites, then they would not be a regulatory sites but rather structural sites in which the binding of abundant cellular monovalent ions affords additional stability to the DNA-bound conformation of *EcNikR*.

To decipher the physical basis underlying any difference in metal binding specificity at both the high affinity and second metal binding sites we conducted a series of detailed molecular simulations on the *EcNikR* structure. We begin with an analysis of the *EcNikR* structure when either  $K^+$  or  $Ni^{2+}$  occupies the high affinity or the second metal binding sites. We then explore the effect of the identity of the ion in the second metal binding site on *EcNikR*-DNA binding using a combined molecular mechanics Poisson-Boltzmann (MMPB) approach (15). Lastly, we use detailed free energy simulations to explore the effect ion size in the second metal binding site has on *EcNikR*-DNA association. In total, these data clarify the physical basis for metal ion specificity in both the high affinity and second metal binding sites in *EcNikR*.

### III.C. Results

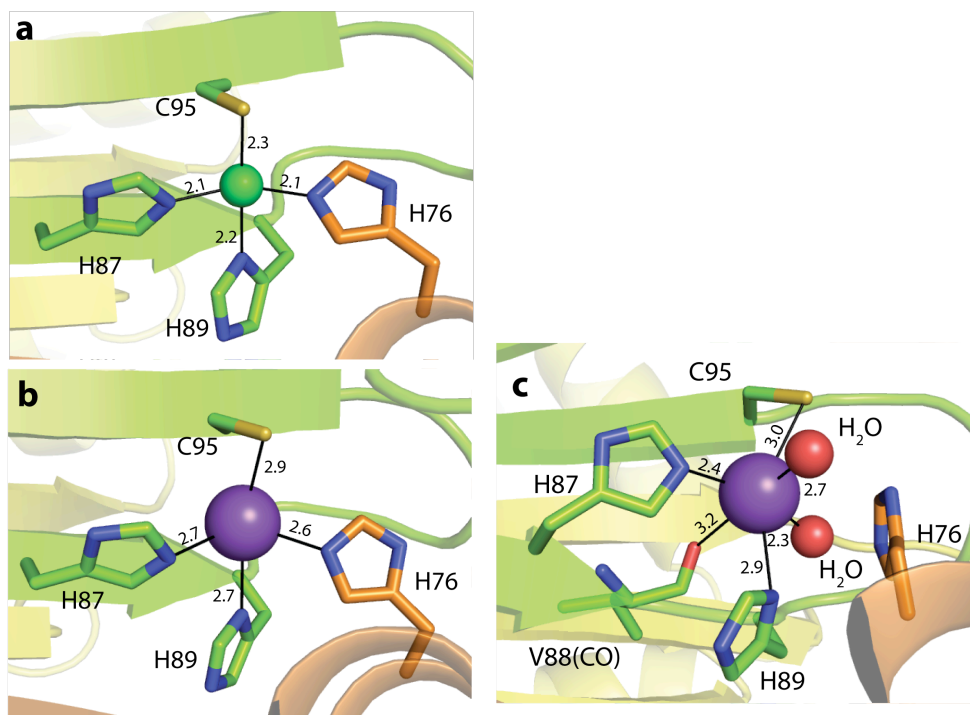
#### III.C.1. The Conformation of High Affinity Sites in the Presence of $Ni^{2+}$ or $K^+$

The high affinity metal binding sites on *EcNikR* have been well-characterized as square-planar  $Ni^{2+}$ -binding sites (Figure III.1a) (8, 16, 17). While this site is preferentially a  $Ni^{2+}$  binding site, *in vitro* metal-binding studies have shown that the coordinating species are flexible and can rearrange under different conditions (8, 17, 18). In light of this, we explored whether high affinity sites in *EcNikR* could rearrange to accommodate  $K^+$ , which is present at much higher concentrations in the intracellular space than  $Ni^{2+}$ . Starting our studies with the high affinity sites allows us to explore the preference for  $Ni^{2+}$  versus  $K^+$  under conditions where the identity of the physiologically relevant metal is unquestioned.

Extensive energy minimizations of the  $Ni^{2+}$  containing high affinity sites do not alter the geometry or the ion-ligand distances relative to the crystal structure (Figure III.2a). To determine potential binding modes for  $K^+$  in the high affinity sites, we replaced  $Ni^{2+}$  with  $K^+$  and energy

minimized the system. The objective of these calculations was to determine if there are flexible moieties in the vicinity of the high affinity site that could participate in metal coordination, thereby yielding a geometry that was favorable for  $K^+$ . However, the energy minimized structure does not significantly deviate from a square-planar geometry (Figure III.2b). While this geometry is expected for  $Ni^{2+}$ , it is unprecedented for  $K^+$ . A recent review of metal-ligand geometries of 4,277 small molecule crystal structures and 113 proteins structures suggests that the minimum coordination number for  $K^+$  is 5, with 6 being the most common number of coordinating ligands (19). In addition, the resulting coordinating species in this site consist of nitrogen and sulfur atoms, known  $Ni^{2+}$  ligands, but less common  $K^+$  ligands (19, 20).

**Figure III.2.** Representative structures of the high affinity metal binding sites after energy minimization and MD simulation studies. High affinity site with either (a)  $Ni^{2+}$  or (b)  $K^+$  after energy minimization. Metal-ligand distances are shown in Å. (c) Average structure from MD simulation of high affinity site containing  $K^+$ . Coloring is the same as in Figure III.1. Water molecules are represented as red spheres.



Since typical energy minimization routines find local energy minima in the vicinity of the starting structure, we performed molecular dynamics simulations of *EcNikR* with  $K^+$  in the high affinity sites to sample low energy states over a larger region of conformational space. The goal is to determine whether the protein can adopt conformations that are consistent with our current understanding of favorable  $K^+$  binding geometries. Simulations of *EcNikR* with  $K^+$  in the high affinity sites were performed for 3.1 ns in explicit solvent. The average structure arising from these simulations has  $K^+$  coordinated by six ligands arranged in an octahedral geometry (Figure III.2c) – a geometry consistent with prior analyses of  $K^+$ -ligand binding sites (19). In the average structure, three of the original high affinity site ligands maintain their interactions with the ion while the H76 side chain is displaced by 3.7 Å and the backbone carbonyl of V88, along with two water molecules, aid in coordinating the  $K^+$  ion (Figure III.2c). In short, in order for  $K^+$  to adopt its expected octahedral geometry, the protein “opens” to allow water molecules to enter the high affinity site during the simulation. For comparison, we also conducted simulations in explicit solvent of *EcNikR* with  $Ni^{2+}$  in the high affinity sites. After more than 3 ns, however, no water penetrates the high affinity site when it is occupied by  $Ni^{2+}$ , and the  $Ni^{2+}$  maintains its interactions with all four coordinating species as shown in Figure III.2a.

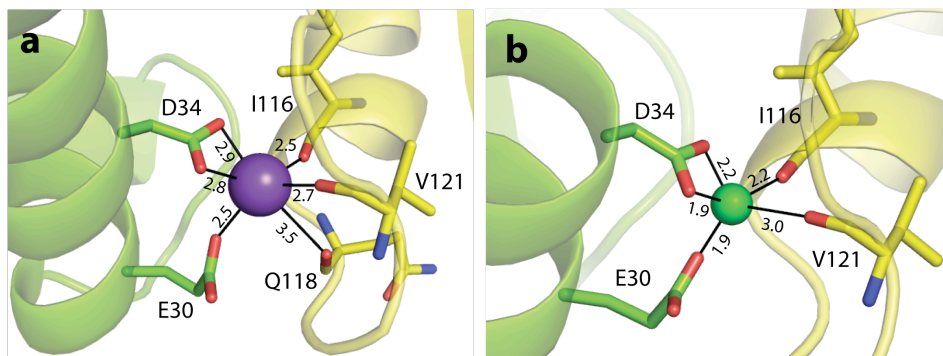
These data suggest that the high affinity sites in the protein cannot rearrange to form ion coordination numbers that are consistent with favorable  $K^+$  binding geometries. An octahedral geometry is only obtained when additional solvent molecules enter the site to participate in ligand coordination. However, as the high affinity sites are not solvent exposed, this requires the protein to undergo significant conformational changes that allow the entry of water molecules. This observation suggests that  $K^+$ -containing high affinity sites are associated with large conformational changes that cause the protein to significantly deviate from the prototypical *EcNikR* structure.

### *III.C.2. The Conformation of the Second Metal Binding Site in the Presence of $Ni^{2+}$ or $K^+$*

In the crystal structure of *EcNikR* bound to DNA, ligands that coordinate the ion in the second metal binding site are arranged in an octahedral geometry (Figure III.1b) and energy

minimization of this site does not significantly alter this geometry (Figure III.3a). To explore whether the second metal binding site can rearrange to adopt conformations that are favorable for  $\text{Ni}^{2+}$ , we replaced  $\text{K}^+$  with  $\text{Ni}^{2+}$  in the crystal structure of *EcNikR* bound to DNA. Subsequent energy minimization resulted in a distorted square-pyramidal geometry, with a coordination number of 5, and shorter metal-ligand distances (Figure III.3b). The shorter metal-ligand distances in the complex with  $\text{Ni}^{2+}$  bound at the second metal binding site are consistent with  $\text{Ni}^{2+}$  having a smaller van der Waals radius than  $\text{K}^+$ ; the typical  $\text{Ni}^{2+}$ -O distance is about 2.2 Å while the average  $\text{K}^+$ -O distance is about 2.8 Å (19, 20). An analysis of  $\text{Ni}^{2+}$  coordination geometries obtained from 8 structures in the Protein Data Bank and over 1,000 structures in the Cambridge Structural Database reveals that similar geometries have been observed in other crystal structures that contain bound  $\text{Ni}^{2+}$  ions (20-22).

**Figure III.3.** Representative structures of the second metal binding site from minimization studies of the *EcNikR*-DNA complex with either (a)  $\text{K}^+$  or (b)  $\text{Ni}^{2+}$  bound in the second metal binding site. Distances are in Å and coloring is the same as in Figure III.1.



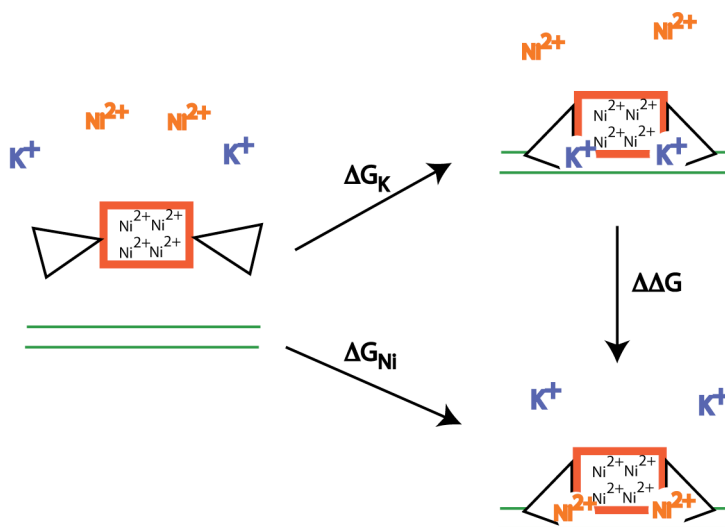
Molecular dynamics simulations of *EcNikR* complexed to DNA with either  $\text{K}^+$  or  $\text{Ni}^{2+}$  in the second metal binding site confirm that the octahedral geometry and the distorted square-pyramidal geometry for  $\text{K}^+$  and  $\text{Ni}^{2+}$ , respectively, represent stable geometries for both ions. Over the course of a 2.1 ns simulation, both metals maintained the previously described binding geometries with reasonable metal-ligand distances. Hence, unlike the previous simulations that uncovered significant structural changes in high affinity sites when the  $\text{Ni}^{2+}$  was replaced with

$K^+$ , these data suggest that the second metal binding site can accommodate either ion and substitution with  $Ni^{2+}$  does not lead to significant deviations in the *EcNikR*-DNA structure.

### III.C.3. *EcNikR*-DNA Association with Either $Ni^{2+}$ or $K^+$ in the Second Metal Binding Site

In light of these data we explored the effect that  $K^+$  or  $Ni^{2+}$  binding at the second metal binding site has on *EcNikR*-DNA association. We are interested in calculating the difference between the energy associated with *EcNikR* binding to DNA with  $K^+$  in the second site ( $\Delta G_K$ ) and DNA binding with  $Ni^{2+}$  in the second site ( $\Delta G_{Ni}$ ) (Figure III.4). The difference between the two binding energies is equal to the free energy difference between two states; one state has  $K^+$  in the second site and the other state has  $Ni^{2+}$  in the second site, and  $\Delta\Delta G = \Delta G_{Ni} - \Delta G_K$ . The thermodynamic cycle used for the MMPB calculations is outlined in Figure III.4. If  $\Delta\Delta G$  is positive, *EcNikR*-DNA binding is preferred when  $K^+$  is in the second metal binding site and if  $\Delta\Delta G$  is negative *EcNikR*-DNA binding is preferred when  $Ni^{2+}$  is bound.

**Figure III.4.** Thermodynamic path comparing *EcNikR*-DNA binding with either  $K^+$  ( $\Delta G_K$ ) or  $Ni^{2+}$  ( $\Delta G_{Ni}$ ) at the second metal binding site. Red rectangles represent the MBD, black triangles the RHH domains, parallel green lines the DNA, and ions are explicitly shown in blue or orange. The ions not bound to the structure are infinitely distant from the protein.



We note that the individual binding free energies ( $\Delta G_K$  and  $\Delta G_{Ni}$ ) can be decomposed into a sum of electrostatic and non-electrostatic contributions (23, 24):

$$\Delta G_K = \Delta G_K^{elec} + \Delta G_K^{non-elec} \quad (1)$$

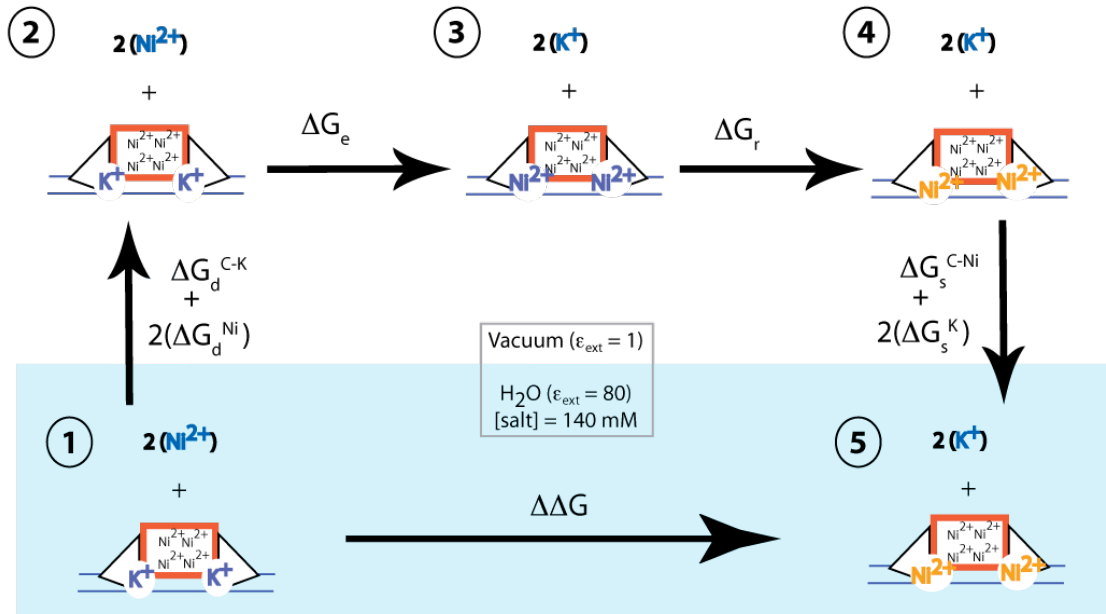
$$\Delta G_{Ni} = \Delta G_{Ni}^{elec} + \Delta G_{Ni}^{non-elec} \quad (2)$$

In each case, the non-electrostatic contributions can be expressed as a sum of a hydrophobic term plus additional terms that account for other contributions such as configuration entropy (23-25). These non-electrostatic terms are typically estimated from an analysis of the unbound state and the bound complex; e.g., the hydrophobic term is calculated using the buried surface area of the complex (23-25). We assume that the *EcNikR* binding mode is the same regardless of whether  $Ni^{2+}$  or  $K^+$  is present in the second metal binding site; i.e., that the structural changes at the second metal binding site are small (Figure III.3). Consequently,  $\Delta G_{Ni}^{non-elec} \approx \Delta G_K^{non-elec}$  and hence  $\Delta \Delta G \approx \Delta G_{Ni}^{elec} - \Delta G_K^{elec}$ . We therefore use a combined molecular mechanics Poisson-Boltzmann approach to estimate the overall difference in binding free energy (15).

We further express  $\Delta \Delta G$  as a sum of physically meaningful terms as outlined in Figure III.5, in a manner similar to what has been done in previous studies (23, 24, 26, 27). First, the  $K^+$ -bound *EcNikR*-DNA complex and two free  $Ni^{2+}$  ions are desolvated (**1**  $\rightarrow$  **2** in Figure III.5). Next, in vacuum  $K^+$  ions are exchanged for  $Ni^{2+}$  ions at the second metal binding sites in the *EcNikR*-DNA complex with the associated free energy difference of  $\Delta G_e$  (**2**  $\rightarrow$  **3**). However, the resulting structure has residues in the second metal binding sites arranged in an orientation that is optimal for  $K^+$  not  $Ni^{2+}$ . Therefore we computed the electrostatic energy associated with residues at the second metal binding sites rearranging to adopt a conformation that is favorable for  $Ni^{2+}$  binding (**3**  $\rightarrow$  **4**). In the last step of the thermodynamic path we calculated the energy associated with solvating the relaxed  $Ni^{2+}$ -bound *EcNikR*-DNA complex and two free  $K^+$  ions (**4**  $\rightarrow$  **5**). Each contribution is calculated from a set of 10 structures taken from a 1 ns molecular dynamics simulation in explicit solvent. Values for the various contributions to  $\Delta \Delta G$  are shown in Table 1 and represent the average value obtained from the 10 structures arising from the molecular dynamics simulations.



**Figure III.5.** Thermodynamic cycle for calculating the electrostatic free energy difference associated with replacing potassium with nickel in the second metal binding site. Red rectangles represent the MBD, black triangles the RHH domains, parallel blue lines the DNA, and ions are explicitly shown in blue or orange. Numbers in circles are to delineate each step of the pathway.



The calculated value for  $\Delta\Delta G$  is large – an average of 733 kcal/mol/site, suggesting that *Ec*NikR-DNA binding is preferred when  $K^+$  occupies the secondary site. To put this number into context, we note that the experimentally determined value for  $Ni^{2+}$  desolvation is also quite large at 477 kcal/mole (and similar to the calculated value of 456 kcal/mol) (28). Interestingly, the value of the exchange term,  $\Delta G_e$ , suggests that replacing  $K^+$  with  $Ni^{2+}$  is favorable; i.e.,  $Ni^{2+}$  makes more favorable interactions with the protein and DNA relative to  $K^+$  (Table III.1). However, this favorable contribution is largely offset by the unfavorable  $Ni^{2+}$  desolvation energy. The other major unfavorable contribution arises from the sum of the desolvation and solvation contributions for the protein DNA complex,  $\Delta G_d^{C-K} + \Delta G_s^{C-Ni} = \Delta G_s^{C-Ni} - \Delta G_s^{C-K} = 932$  kcal/mol/site (where  $\Delta G_s^{C-K}$  is the electrostatic energy associated with solvating the DNA bound complex that has  $K^+$  in the second metal binding site). The large positive value of this term suggests that solvating the DNA bound complex is more

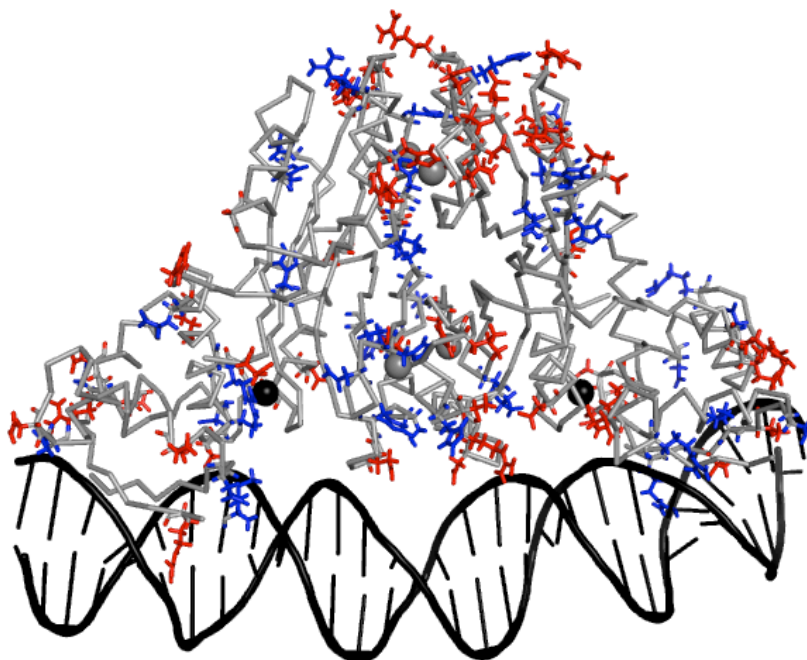
favorable when  $K^+$  is in the second metal binding site. Of note, the complex of *EcNikR*, DNA, and four high affinity  $Ni^{2+}$  ions has a very large overall charge of -84. Addition of two  $K^+$  ions in the second metal binding sites brings the total charge to -82, while the addition of two  $Ni^{2+}$  ions brings the total charge to -80. As the total charge of the system containing  $K^+$  is more negative, it is not surprising that it has a larger negative (i.e., more favorable) solvation energy relative to the complex with  $Ni^{2+}$  bound.

**Table III.I.** Contributions to the electrostatic free energy difference for the path shown in Figure III.5.

<b>Contribution</b>	<b>kcal/mol/site</b>
$\Delta G_d^{C-K} + \Delta G_s^{C-Ni}$	932
$\Delta G_d^{Ni}$	456
$\Delta G_e$	-501
$\Delta G_r$	-61
$\Delta G_s^K$	-93
$\Delta\Delta G$	733

The Poisson-Boltzmann formalism allows us to calculate residue specific contributions to the overall difference in free energy ( $\Delta\Delta G$ ). Figure III.6 highlights the residues with the greatest contribution, positive (blue) or negative (red), to the overall difference in free energy. It is noteworthy that residues which are distant from the secondary site make significant contributions to the overall free energy change. That is, the relative preference for  $K^+$  in the secondary site cannot be explained using an analysis of the structure of the protein in the vicinity of the second metal binding site alone.

**Figure III.6.** *EcNikR*-DNA structure with residues with the most extreme contributions to  $\Delta\Delta G$  colored in red and blue. Red residues contribute  $\leq -10$  kcal/mole to  $\Delta\Delta G$  and prefer  $\text{Ni}^{2+}$  ions in the second metal binding sites (black spheres). Residues in blue contribute  $\geq 10$  kcal/mole to  $\Delta\Delta G$  and prefer  $\text{K}^+$  ions in the second metal binding sites. All backbone atoms are shown in ribbon form and are colored grey. Residues that contribute between -10 and 10 kcal/mole to the  $\Delta\Delta G$  are not shown in stick form.

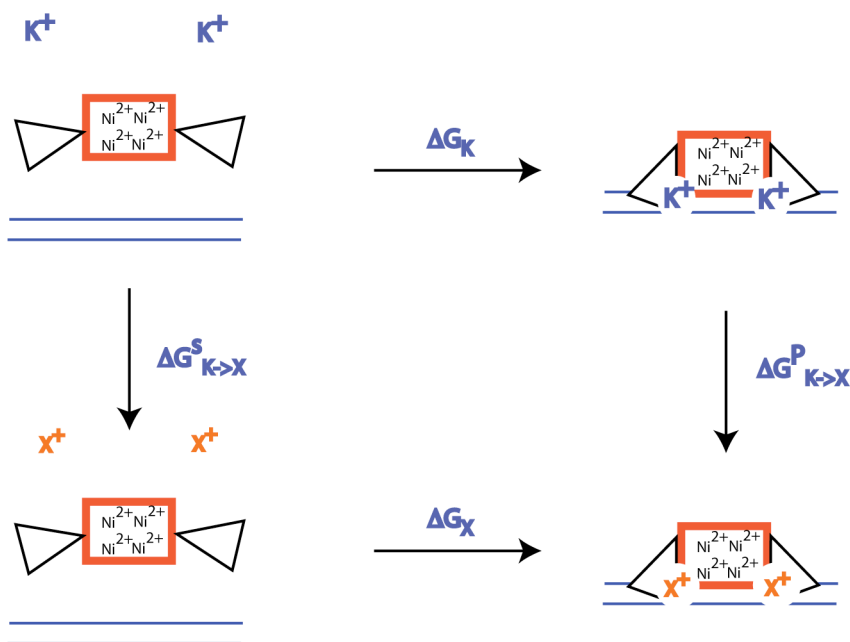


#### *III.C.4. The Effect of Ion Size on DNA Binding*

The electrostatic calculations suggest that *EcNikR*-DNA association is more favorable when  $\text{K}^+$ , and not the divalent ion  $\text{Ni}^{2+}$ , occupies the second metal binding site. This large difference is due, in part, to the fact that  $\text{Ni}^{2+}$  has a relatively large desolvation penalty. This raises the possibility that *EcNikR* DNA binding may be afforded by another monovalent cation in the second metal binding site. In particular we are interested in how the affinity of *EcNikR* for DNA changes when ions of different sizes occupy the second metal binding site. For these studies we focus on  $\text{Na}^+$ , which is considerably smaller than  $\text{K}^+$  and  $\text{Cs}^+$ , which is larger than  $\text{K}^+$ .

The thermodynamic cycle for these calculations is shown in Figure III.7. We are interested in the difference between the binding free energy of two binding reactions. In the first reaction, *EcNikR* binds DNA with  $K^+$  in the second metal binding site, and the associated free energy difference is  $(\Delta G_K)$ . In the second reaction *EcNikR* binds DNA with a monovalent ion denoted by  $X^+$ , and again the associated free energy difference is given by  $(\Delta G_X)$ . The relative binding free energy is  $\Delta\Delta G_{K\rightarrow X} \equiv \Delta G_K - \Delta G_X = \Delta G_{K\rightarrow X}^P - \Delta G_{K\rightarrow X}^S$ . The overall  $\Delta\Delta G$  can therefore be calculated using the contributions along the alchemical paths,  $\Delta G_{K\rightarrow X}^P, \Delta G_{K\rightarrow X}^S$ .

**Figure III.7.** Thermodynamic cycle for calculating the free energy difference associated with replacing a monovalent cation with the radius of potassium with a larger or smaller radius. NikR representations are the same as in Figure III.2 and “X<sup>+</sup>” represents an ion having different Lennard Jones parameters than  $K^+$ .



Ions can be characterized by a distinct van der Waals radius,  $\sigma$ , which determines the equilibrium interatomic distance, and the well-depth,  $\epsilon$ . In Figure III.7,  $X^+$  represents a monovalent ion having a van der Waals radius and well-depth different from  $K^+$ . Therefore, we calculate  $\Delta G_{K\rightarrow X}^P$  and  $\Delta G_{K\rightarrow X}^S$  in a stepwise fashion where first we calculate the effect of changing  $\sigma$  and

then we compute the effect of changing the well-depth,  $\epsilon$ . For example, we express the free energy differences along the alchemical paths associated with transforming  $K^+$  to  $Na^+$  as:

$$\Delta G_{K \rightarrow Na}^S = \Delta G_{K(\sigma_{K^+}, \epsilon_{K^+}) \rightarrow Y(\sigma_{Na^+}, \epsilon_{K^+})}^S + \Delta G_{Y(\sigma_{Na^+}, \epsilon_{K^+}) \rightarrow Na(\sigma_{Na^+}, \epsilon_{Na^+})}^S \quad (3)$$

$$\Delta G_{K \rightarrow Na}^P = \Delta G_{K(\sigma_{K^+}, \epsilon_{K^+}) \rightarrow Y(\sigma_{Na^+}, \epsilon_{K^+})}^P + \Delta G_{Y(\sigma_{Na^+}, \epsilon_{K^+}) \rightarrow Na(\sigma_{Na^+}, \epsilon_{Na^+})}^P \quad (4)$$

While the individual contributions to the total free energy change are not state functions, the total free energy change is (29). Therefore, the precise path chosen to calculate the overall free energy will not, in principle, affect the final result. Each term on the right hand side of equations (3) and (4) is computed using thermodynamic integration with a linear alchemical path. The overall free energy differences are listed in Table III.2. For both  $Na^+$  and  $Cs^+$ , the relative binding affinities are positive, suggesting that DNA binding is more favorable when the second site contains  $K^+$ .

**Table III.2.** Free energy differences between *EcNikR*-DNA complex with  $K^+$  and other monovalent ions bound in the second metal binding site. Energies given in kcal/mole.

	$Na^+$	$Cs^+$
$\Delta\Delta G_{vdW}$	4.02	0.41
$\Delta\Delta G_s$	1.05	0.45
$\Delta\Delta G_{tot}$	5.07	0.86

### III.D. Discussion

The metal binding sites of the transcriptional repressor *EcNikR* have been the subject of much attention (8-11, 16-18, 30). While the role of high affinity  $Ni^{2+}$  binding site as the main regulator of *EcNikR*'s affinity for DNA has not been in question, the function of the second metal site has been less clear. Possibilities include that this second site is an additional regulatory site to which excess  $Ni^{2+}$  ions can bind, yielding a tighter *EcNikR*-DNA complex. Alternatively, this second site could be non-regulatory, binding the abundant cellular  $K^+$  ion to further stabilize the *EcNikR*-DNA interaction. Here we consider whether both  $K^+$  and  $Ni^{2+}$  can stably bind this second site. Using unconstrained MD simulations of the *EcNikR*-DNA complex with either  $K^+$

or  $\text{Ni}^{2+}$  in the second metal site, we show that either of these metals is a reasonably good fit for the site. The overall backbone average RMS deviations of the *EcNikR*-DNA complex with either metal bound at the second metal site are very similar and in both cases, the second metal binding site adopts realistic ion-ligand geometries. In light of these observations, we explored the effect of having either  $\text{Ni}^{2+}$  or  $\text{K}^+$  in the second metal binding site on *EcNikR*-DNA association. Electrostatic free energy calculations suggest that while the Coulombic interactions between  $\text{Ni}^{2+}$  and the *EcNikR*-DNA complex are more favorable relative to  $\text{K}^+$ , this favorable contribution is counterbalanced by the unfavorable terms associated with the desolvation penalty of  $\text{Ni}^{2+}$  and the *EcNikR*-DNA complex. An analysis of the individual residue contributions to the overall binding free energies suggest that the preference for  $\text{K}^+$  at the second metal binding site cannot be explained from an analysis of the local conformation of the protein in the vicinity of the second metal binding site. Residues that are distant from the second metal binding site have a significant effect on the identity of the ion in this site (Figure III.6). These data raise the interesting possibility that mutations at sites that are distant from the second metal binding site can affect the ion that is present in the bound complex.

As the high desolvation penalty of  $\text{Ni}^{2+}$  is partially responsible for the  $\text{K}^+$  being preferred in the second metal binding site, *EcNikR* DNA binding may be possible with any monovalent ion in the second metal binding site since these ions have much smaller desolvation penalties (28, 31). Additional free energy simulations that examine the effect of having other monovalent ions at the secondary site on *EcNikR*-DNA association suggest that the affinity of *EcNikR* for DNA is significantly reduced when the second metal binding site contains  $\text{Na}^+$ , a common monovalent cation in the cellular milieu (Table III.2).

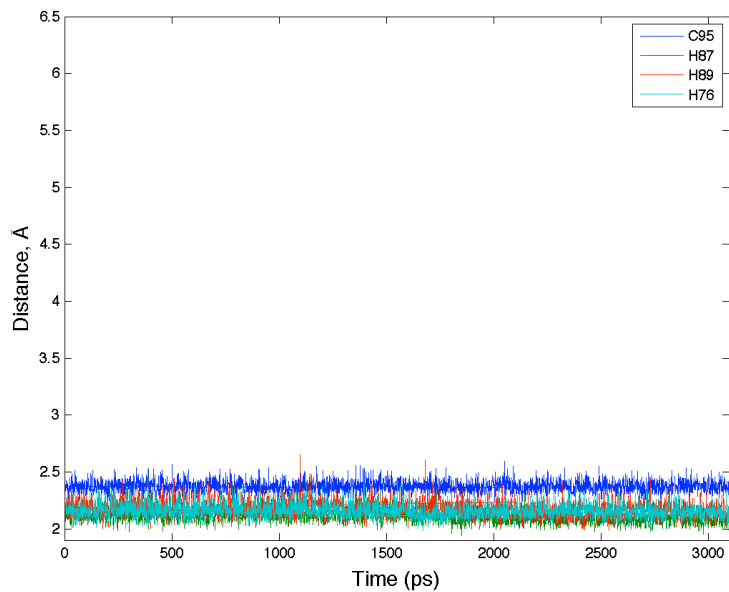
With the finding that desolvation is the main source of preference for  $\text{K}^+$  over  $\text{Ni}^{2+}$  in the second metal site, it is important to understand why the high affinity site binds  $\text{Ni}^{2+}$  and not  $\text{K}^+$ , especially given the high concentration of  $\text{K}^+$  compared to  $\text{Ni}^{2+}$  in *E. coli*. We found that the second metal site can rearrange to stably bind both metals, raising the question if the same is true for the high affinity sites. Replacing  $\text{Ni}^{2+}$  with  $\text{K}^+$  at high affinity sites, followed by energy minimization, however, does not lead to ion-ligand geometries that are consistent with what one

would expect for  $K^+$ . Energy minimized high affinity sites that contain  $K^+$  do not form an octahedral geometry – the preferred binding geometry for  $K^+$  (19). Moreover, the coordination number for  $K^+$  at these sites is 4, whereas the minimum coordination number for  $K^+$  in both small molecular and protein crystal structures is 5 (19). Additional molecular dynamics simulations of *EcNikR* with  $K^+$  at high affinity sites suggest that realistic coordination geometries for  $K^+$  cannot be achieved with moieties that arise solely from the protein. That is, an octahedral geometry is only achieved when the protein undergoes significant conformational changes that cause the high affinity sites to become solvent exposed. These data suggest that the *EcNikR* structure cannot accommodate  $K^+$  at the high affinity sites.

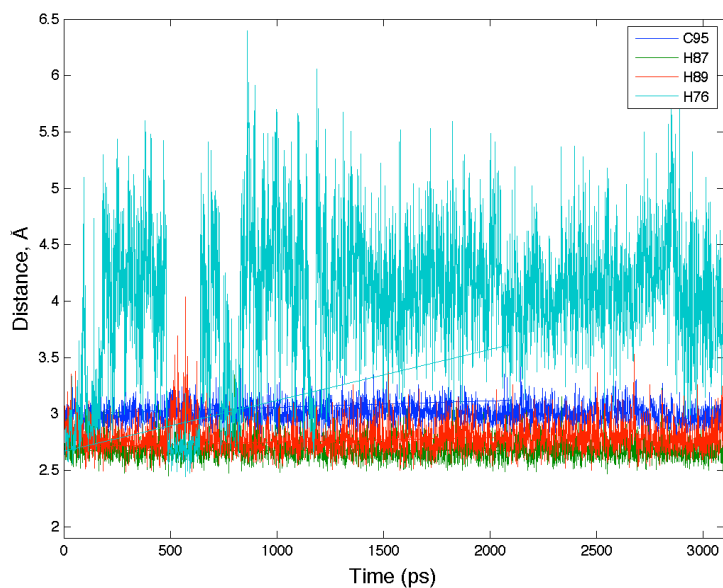
Additional insights into the effect of  $K^+$  on the *EcNikR* structure are obtained from an analysis of its coordinating species in the molecular dynamics simulations. After 3 ns of molecular dynamics,  $K^+$  achieves an octahedral geometry where two of the ligands are water molecules. The side chain of H76, which normally participates in ion coordination, shifts to a position where it can no longer coordinate the ion in the site (Figure III.2c, III.8). This observation is of interest because structural studies have linked ion ligation at high affinity sites by residue H76 with ordering of the  $\alpha 3$  helix in the MBD, which contains residue H76 (9, 18). The ordering of the  $\alpha 3$  helix upon  $Ni^{2+}$  binding has been implicated in the mechanism of *EcNikR*-DNA binding and solution studies suggest that metals that are capable of ordering the  $\alpha 3$  helix are those that induce *EcNikR*-DNA binding (9, 11, 12, 18, 30). Metals that do use H76 as a ligand, such as  $Ni^{2+}$  and  $Cu^{2+}$ , have well-ordered  $\alpha 3$  helices (8, 18). However, when no metal or a metal like  $Zn^{2+}$  that does not induce strong DNA binding is bound at the high affinity site, H76 is not utilized as a ligand and the  $\alpha 3$  helix is relatively disordered (18). Although the time scale of our simulations is not sufficiently long to reliably examine helix stability in the presence of  $K^+$ , these data suggest that  $K^+$  does not induce the proper ligand ordering at the high affinity site, and may not support  $\alpha 3$ -helix stability or, in turn, proper DNA binding.

**Figure III.8.** Representative graphs of metal-ligand distances for the four known metal ligands of the high affinity site with either (a)  $\text{Ni}^{2+}$  or (b)  $\text{K}^{+}$  bound plotted over the period of the MD simulations. The graphs are from a one of the four high affinity sites in the protein, but all sites look have similar graphs.

**a**



**b**





Overall our data explain why  $\text{Ni}^{2+}$  is preferred over  $\text{K}^+$  at high affinity sites and suggest that *EcNikR* binding to DNA is more favorable when  $\text{K}^+$  is present at the second metal binding site. Recent studies have explored the effect of  $\text{K}^+$  on *EcNikR*-DNA binding using DNase footprinting and gel mobility shift assays. These results are consistent with our findings in that they demonstrate that  $\text{K}^+$  is required for *EcNikR*-DNA association *in vitro* (13).

In conclusion, *EcNikR* is exquisitely designed with a number of metal binding sites of varying metal preferences. The central high affinity  $\text{Ni}^{2+}$ -binding sites are sensory sites that specifically bind the scarce cellular  $\text{Ni}^{2+}$  ion, enabling binding to the *nik* promoter. The second metal binding sites are located at the interface of the MBD and RHH domains and are composed solely of oxygen ligands from each domain. This conserved second metal binding site is a structural site that prefers the cellularly abundant  $\text{K}^+$  ion to help stabilize the *EcNikR*-DNA interaction. By utilizing two different metals in each of these sites, *EcNikR* optimizes its specificity and strength of DNA binding.

### III.E. Methods

#### III.E.1. Structure Preparation and Solvation

Structures of  $\text{Ni}^{2+}$ -bound *EcNikR* and *EcNikR*-DNA were obtained from the PDB (PDB IDs 2HZA and 2HZV, respectively) (9, 32). Missing protein residues were added with only backbone and  $\text{C}_\beta$  atoms in approximate positions in COOT (33). Missing heavy atoms and all hydrogen atoms were built with ICBuild and HBuild functions in CHARMM version 33b2 using the all-atom (CHARMM27) parameters for proteins, nucleic acids and potassium ions (34). Nickel parameters (van der Waals radius of 1.4125 Å and epsilon of -0.010) were obtained from Dr. Johan Bredenberg (personal communication) and thiolate parameters from published studies (35). Histidines were modeled as  $\delta$ - or  $\epsilon$ -protonated depending on the likely hydrogen bonding pattern; i.e., heavy atoms of hydrogen bonding residues that were within 3.5 Å of one another suggest that the corresponding nitrogen on His should be protonated. The high affinity nickel ligand C95 was modeled as a deprotonated thiolate. Following these modifications to the protein-DNA complex, 100 steps of steepest decent minimization were run in vacuum to remove bad

contacts. For all simulations the SHAKE command was used to restrain bonds involving hydrogen atoms near their equilibrium values and the non-bonded cutoff was set to 13.0 Å (36).

### *III.E.2. Minimization and Molecular Dynamics of the High Affinity Site in EcNikR*

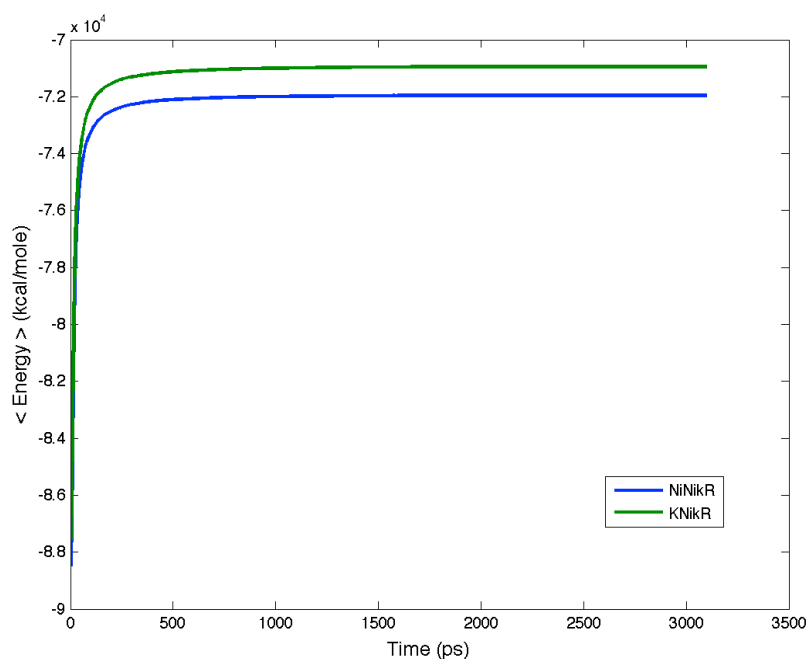
The EcNikR protein was prepared as described above with either 4 Ni<sup>2+</sup> or 4 K<sup>+</sup> ions filling the high affinity metal binding sites. Simulations with either Ni<sup>2+</sup> or K<sup>+</sup> ions in the high affinity sites were performed in explicit solvent using a stochastic boundary approach (37). The system was solvated using TIP3P water molecules with a sphere of radius 39 Å centered around the metal binding domain and a stochastic boundary potential was used to maintain the water sphere around the system (38, 39). This water sphere allowed for a buffer of ~15 Å between the protein exterior and the boundary of the water sphere. There were a total of 5900 water molecules in the simulation, which were minimized using 500 steps of steepest decent, holding the protein portion fixed. Each of the high affinity metal sites in both Ni<sup>2+</sup>-EcNikR and K<sup>+</sup>-EcNikR structures were minimized within 5 Å of each site using 500 steps of conjugate gradient and holding the rest of the protein and water fixed. Minimizations that employed a larger cutoff did not significantly change our results.

Following the minimization studies, the system was partitioned for the MD simulations in the following way. All solvent molecules, and all protein atoms and ions within 39 Å of the center of the protein were in the reaction region and underwent full MD simulation. The protein molecules outside the sphere were constrained by force constants derived from the B-factors of the atoms in the X-ray crystal structure. The B-factors for atoms that were built into the structure and thus did not have crystallographic B-factors were set to the average B-factor depending on that type of atom and its location in the main chain or side chain. B-factors were converted to force constants as previously described (37).

Molecular dynamics simulations were run using CHARMM (34). First, the protein was gently heated from 0 K to 300 K at a rate of 5 K/ps using a Nosé-Hoover heat bath (40). Dynamical simulations then ran at 300 K until the system had been allowed to fully equilibrate (Figure III.9). The total run time was 3.1 ns. Structures were saved every 10 ps. From the final 600 ps of

the simulation an average structure was calculated and briefly minimized to remove bad contacts using 100 steps of steepest descent.

**Figure III.9.** The average energy of the system over the time of the simulation with either  $K^+$  or  $Ni^{2+}$  bound in the high affinity site.



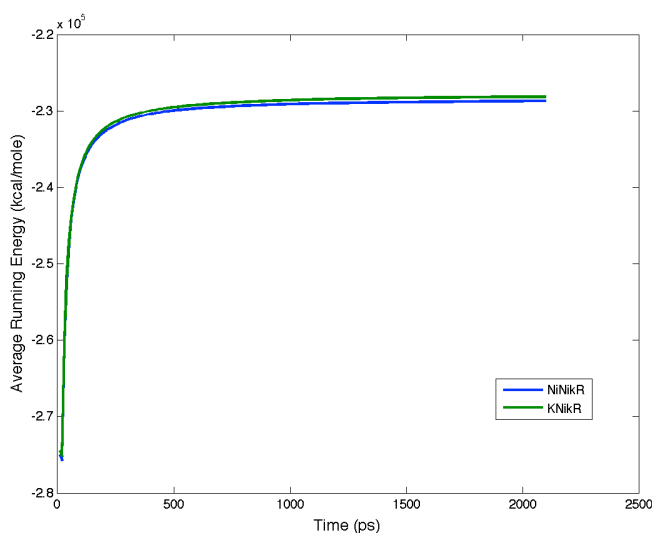
### III.E.3. Minimization and Molecular Dynamics of the Second Metal Binding Site in the *EcNikR*-DNA Complex

For the studies of the second metal binding site the  $Ni^{2+}$ -*EcNikR*-DNA structure was prepared as described above with either  $K^+$  or  $Ni^{2+}$  in the second metal binding site and always with  $Ni^{2+}$  at all 4 high affinity sites. The protein was solvated using a 57 Å sphere of water (with a total of 21,331 water molecules) in order to fully solvate each second metal binding site with a ~15 Å water buffer. In general, simulations with DNA require explicit solvent and counterions to achieve realistic geometries (38). However, the inclusion of specific counterions can lead to relatively long convergence times for systems of modest size (41). Therefore, we again employed a stochastic boundary approach where the DNA is restrained using the crystallographically determined B-factors and no explicit counter-ions are used in the dynamic simulations (42). This

represents a compromise between computational efficiency and accuracy and helps to ensure that the DNA does not sample unrealistic conformations.

Minimization studies of the second metal binding sites were performed as described for the high affinity binding sites. For dynamics simulations the system was partitioned such that all solvent, protein, and ions underwent full dynamics, but the DNA was constrained using harmonic restraints derived from B-factors. The same heating, equilibration, and production procedure described above was used (Figure III.10). The total MD run time was 2.1 ns with the last 600 ps being used to construct the average structure.

**Figure III.10.** The average energy the system over the time of the simulation with either  $K^+$  or  $Ni^{2+}$  bound in the second metal binding site.



#### III.E.4. MMPB Studies

For the Poisson-Boltzmann (PB) studies we first conducted additional dynamical simulations to obtain representative structures that could be used for electrostatic calculations. In these calculations the four atoms directly coordinating each nickel ion at the high affinity metal binding sites were constrained using an improper dihedral angle of  $0^\circ$  with force constant of  $100 \text{ kcal}/\text{\AA}^2$  to ensure that optimal square-planar  $Ni^{2+}$  coordination geometry was maintained. The second metal sites were minimized as described above with either  $K^+$  or  $Ni^{2+}$  in the sites. After

this minimization, the second metal sites were examined and then the final minimized geometry and distances noted (Figure III.3). The second metal binding sites were constrained to the distances defined in Figure III.3 using the `resdistance` command with a force constant of 1.0 kcal/Å<sup>2</sup>. Similar approaches have been employed in other studies of protein complexes that contain metal binding sites (43-45).

The protein-DNA complex was solvated in a water sphere of 35 Å centered around the MBD portion of the structure and fully solvating both second metal binding sites. A total of 3062 water molecules were added and the system was partitioned and heated as previously described. Given the restraints at the high affinity and second metal binding sites only 80 ps of equilibration was needed followed by 1 ns of production dynamics. Ten structures were taken from the 1 ns production trajectory, 1 every 100 ps. At this point the water molecules were deleted and the 10 representative structures were ready for Poisson-Boltzmann calculations.

The program Delphi was used to solve the non-linear Poisson-Boltzmann equation for each of the complexes. The initial grid size was 250 Å square with a grid spacing of 1 Å, which was then focused to a grid size of 125 Å with a grid spacing of 0.5 Å. The interior dielectric of the protein was set to 4 for all calculations. For the vacuum calculations, the exterior dielectric was set to 1 and for calculations in water the exterior dielectric was set to 80 with a salt concentration of 140 mM. The energies for all 10 structures in each of the five states along the pathway in Figure III.5 were then averaged and the electrostatic free energy differences were then computed.

### III.E.5. Thermodynamic Integration

We calculated the free energy difference between the *EcNikR*-DNA complex structure with K<sup>+</sup> bound and the structure with an ion, X<sup>+</sup>, where X<sup>+</sup> is either Na<sup>+</sup> or Cs<sup>+</sup>. The thermodynamic paths of interest are depicted as the horizontal legs of the thermodynamic cycle in Figure III.7; *EcNikR* binding to DNA with potassium ( $\Delta G_K$ ) or a monovalent ion with a larger or smaller radius than that of potassium ( $\Delta G_X$ ). We are interested in the difference of these energies or  $\Delta\Delta G$  where  $\Delta\Delta G_{K \rightarrow X} \equiv \Delta G_K - \Delta G_X = \Delta G_{K \rightarrow X}^P - \Delta G_{K \rightarrow X}^S$ . We note that for an exact calculation of  $\Delta G_{K \rightarrow X}^S$  and

$\Delta G_{\mathbf{K} \rightarrow \mathbf{X}}^P$  we must account for both the radius of the atom,  $\sigma$ , and the well-depth,  $\varepsilon$ . From equations 3 and 4,  $\Delta G_{\mathbf{K} \rightarrow \mathbf{X}}^S$  and  $\Delta G_{\mathbf{K} \rightarrow \mathbf{X}}^P$  can be decomposed into two steps, a  $\Delta G_{\mathbf{K} \rightarrow \mathbf{Y}}$  step where only the ionic radius is changed ( $\Delta G_{\mathbf{K}(\sigma_{\mathbf{K}^+} \varepsilon_{\mathbf{K}^+}) \rightarrow \mathbf{Y}(\sigma_{\mathbf{X}^+} \varepsilon_{\mathbf{K}^+})}^S$ ,  $\Delta G_{\mathbf{K}(\sigma_{\mathbf{K}^+} \varepsilon_{\mathbf{K}^+}) \rightarrow \mathbf{Y}(\sigma_{\mathbf{X}^+} \varepsilon_{\mathbf{K}^+})}^P$ ), and a  $\Delta G_{\mathbf{Y} \rightarrow \mathbf{X}}$  step where the well-depth is changed ( $\Delta G_{\mathbf{Y}(\sigma_{\mathbf{X}^+} \varepsilon_{\mathbf{K}^+}) \rightarrow \mathbf{X}(\sigma_{\mathbf{X}^+} \varepsilon_{\mathbf{X}^+})}^S$ ,  $\Delta G_{\mathbf{Y}(\sigma_{\mathbf{X}^+} \varepsilon_{\mathbf{K}^+}) \rightarrow \mathbf{X}(\sigma_{\mathbf{X}^+} \varepsilon_{\mathbf{X}^+})}^P$ ).

$\Delta G_{\mathbf{K}(\sigma_{\mathbf{K}^+} \varepsilon_{\mathbf{K}^+}) \rightarrow \mathbf{Y}(\sigma_{\mathbf{X}^+} \varepsilon_{\mathbf{K}^+})}^S$  from equation 3 and  $\Delta G_{\mathbf{K}(\sigma_{\mathbf{K}^+} \varepsilon_{\mathbf{K}^+}) \rightarrow \mathbf{Y}(\sigma_{\mathbf{X}^+} \varepsilon_{\mathbf{K}^+})}^P$  from equation 4 correspond to the free energies associated with mutating the  $\mathbf{K}^+$  atom to an atom  $\mathbf{Y}^+$  with the van der Waals radius of  $\mathbf{X}^+$  but the  $\varepsilon$  of  $\mathbf{K}^+$  ( $-0.087$ ) in solvent or in the *EcNikR*-DNA complex, respectively. To calculate  $\Delta G_{\mathbf{K}(\sigma_{\mathbf{K}^+} \varepsilon_{\mathbf{K}^+}) \rightarrow \mathbf{Y}(\sigma_{\mathbf{X}^+} \varepsilon_{\mathbf{K}^+})}^S$  a single ion in a 20 Å radius sphere of TIP3P water was equilibrated for 100 ps. For  $\Delta G_{\mathbf{K}(\sigma_{\mathbf{K}^+} \varepsilon_{\mathbf{K}^+}) \rightarrow \mathbf{Y}(\sigma_{\mathbf{X}^+} \varepsilon_{\mathbf{K}^+})}^P$  the *EcNikR*-DNA complex with  $\mathbf{K}^+$  bound was solvated as described above with a 35 Å radius sphere centered around one of the two second metal binding sites and equilibrated for 100, 200, or 500 ps. These structures were used as starting points for two separate alchemical transformation experiments described below.

The potential energy used for the alchemical transformation is given by  $V(\lambda) = V_{\mathbf{K}} + \lambda(V_{\mathbf{Y}} - V_{\mathbf{K}})$  where  $V_{\mathbf{K}}$  or  $V_{\mathbf{Y}}$  denote the potential energy of the *EcNikR*-DNA complex with either  $\mathbf{K}^+$  or an ion  $\mathbf{Y}^+$  bound or the ion free in solution. The free energy difference between the states of *EcNikR*-DNA with  $\mathbf{K}^+$  or  $\mathbf{Y}^+$  bound is given by  $\Delta G_{\mathbf{K}(\sigma_{\mathbf{K}^+} \varepsilon_{\mathbf{K}^+}) \rightarrow \mathbf{Y}(\sigma_{\mathbf{X}^+} \varepsilon_{\mathbf{K}^+})}^P = \int_0^1 \langle \Delta V \rangle_{\lambda} d\lambda$ , where  $\Delta V = V_{\mathbf{Y}} - V_{\mathbf{K}}$ . Simulations were performed for both the solvated *EcNikR*-DNA complex and the solvated free ions at  $\lambda = 0.02, 0.1, 0.2, 0.3, 0.4, 0.5, 0.6, 0.7, 0.8, 0.9$ , and 0.98. At each  $\lambda$  value, 50 ps of equilibration were followed by 50 ps of production dynamics. The final free energy differences were computed using a standard quadrature. Electrostatic and non-electrostatic contributions to the free energy change were calculated separately as previously described (46). To determine the contribution of the well-depth to the difference in free energy, we ran a similar experiment to that described above, but in this case we calculated the difference in free energy between having an atom the size and well-depth of  $\mathbf{K}^+$  and an atom  $\mathbf{Y}^+$  with the size of  $\mathbf{K}^+$  but well-depth of  $\mathbf{X}^+$ .

### **III.F. Acknowledgements**

The authors would like to thank Deborah Zamble and Sheila Wang for helpful discussions.

### III.G. References

1. Davis, G. S., Flannery, E. L., and Mobley, H. L. T. (2006) *Helicobacter pylori* HP1512 is a nickel-responsive NikR-regulated outer membrane protein, *Infection and Immunity* 74, 6811-6820.
2. Mulrooney, S. B., and Hausinger, R. P. (2003) Nickel uptake and utilization by microorganisms, *FEMS Microbiology Reviews* 27, 239-261.
3. Uden, G., and Bongaerts, J. (1997) Alternative respiratory pathways of *Escherichia coli*: energetics and transcriptional regulation in response to electron acceptors, *Biochimica et Biophysica Acta* 1320, 217-234.
4. Wu, L. F., Navarro, C., de Pina, K., Quenard, M., and Mandrand, M. A. (1994) Antagonistic Effect of Nickel on the Fermentative Growth of *Escherichia coli* K-12 and Comparison of Nickel and Cobalt Toxicity on the Aerobic and Anaerobic Growth, *Environmental Health Perspectives* 102, 297-300.
5. Dosanjh, N. S., and Michel, S. L. J. (2006) Microbial nickel metalloregulation: NikRs for nickel ions, *Current Opinion in Chemical Biology* 10, 123-130.
6. Chivers, P. T., and Tahirov, T. H. (2005) Structure of *Pyrococcus horikoshii* NikR: Nickel Sensing and Implications for the Regulation of DNA Recognition, *Journal of Molecular Biology* 348, 597-607.
7. Dian, C., Schauer, K., Kapp, U., McSweeney, S. M., Labigne, A., and Terradot, L. (2006) Structural Basis of the Nickel Response in *Helicobacter pylori*: Crystal Structures of HpNikR in Apo and Nickel-bound States, *Journal of Molecular Biology* 361, 715-730.
8. Schreiter, E. R., Sintchak, M. D., Guo, Y., Chivers, P. T., Sauer, R. T., and Drennan, C. L. (2003) Crystal structure of nickel-responsive transcription factor NikR, *Nature Structural Biology* 10, 794-799.
9. Schreiter, E. R., Wang, S. C., Zamble, D. B., and Drennan, C. L. (2006) NikR-operator complex structure and the mechanism of repressor activation by metal ions, *Proceedings of the National Academy of Sciences of the United States of America* 103, 13676-13681.
10. Chivers, P. T., and Sauer, R. T. (2000) Regulation of high affinity nickel uptake in bacteria. Ni<sup>2+</sup>-Dependent interaction of NikR with wild-type and mutant operator sites, *Journal of Biological Chemistry* 275, 19735-19741.
11. Chivers, P. T., and Sauer, R. T. (2002) NikR Repressor: High-Affinity Nickel Binding to the C-Terminal Domain Regulates Binding to Operator DNA, *Chemistry & Biology* 9, 1141-1148.
12. Bloom, S. L., and Zamble, D. B. (2004) Metal-Selective DNA-Binding Response of *Escherichia coli* NikR, *Biochemistry* 43, 10029-10038.



13. Wang, S. C., and Zamble, D. B. (2010) Potassium is Critical for the Ni(II)-Responsive DNA-Binding Activity of *Escherichia coli* NikR, *J. Am. Chem. Soc.* *132*, 1506-1507.
14. Epstein, W., and Schultz, S. G. (1966) Cation transport in *Escherichia coli*. VI. K exchange, *J Gen Physiol* *49*, 469-481.
15. Kollman, P. A., Massova, I., Reyes, C., Kuhn, B., Huo, S., Chong, L., Lee, M., Lee, T., Duan, Y., Wang, W., Donini, O., Cieplak, P., Srinivasan, J., Case, D. A., and Cheatham, T. E., 3rd. (2000) Calculating structures and free energies of complex molecules: combining molecular mechanics and continuum models, *Acc Chem Res* *33*, 889-897.
16. Carrington, P. E., Chivers, P. T., Al-Mjeni, F., Sauer, R. T., and Maroney, M. J. (2003) Nickel coordination is regulated by the DNA-bound state of NikR, *Nature Structural Biology* *10*, 126-130.
17. Leitch, S., Bradley, M. J., Rowe, J. L., Chivers, P. T., and Maroney, M. J. (2007) Nickel-Specific Response in the Transcriptional Regulator, *Escherichia coli* NikR, *Journal of the American Chemical Society* *129*, 5085-5095.
18. Phillips, C. M., Schreiter, E. R., Guo, Y., Wang, S. C., Zamble, D. B., and Drennan, C. L. (2008) Structural Basis of the Metal Specificity for Nickel Regulatory Protein NikR, *Biochemistry* *47*, 1938-1946.
19. Harding, M. M. (2002) Metal-ligand geometry relevant to proteins and in proteins: sodium and potassium, *Acta Crystallogr D Biol Crystallogr* *58*, 872-874.
20. Rulisek, L., and Vondrasek, J. (1998) Coordination geometries of selected transition metal ions ( $\text{Co}^{2+}$ ,  $\text{Ni}^{2+}$ ,  $\text{Cu}^{2+}$ ,  $\text{Zn}^{2+}$ ,  $\text{Cd}^{2+}$ , and  $\text{Hg}^{2+}$ ) in metalloproteins, *Journal of Inorganic Biochemistry* *71*, 115-127.
21. Ray, W. J., Post, C. B., Liu, Y., and Rhyu, G. I. (1993) Structural-Changes at the Metal-Ion Binding-Site during the Phosphoglucosyltransferase Reaction, *Biochemistry* *32*, 48-57.
22. Tsai, L. C., Sjolín, L., Langer, V., Bonander, N., Karlsson, B. G., Vanngard, T., Hammann, C., and Nar, H. (1995) Structure of the Azurin Mutant Nickel-Trp48met from *Pseudomonas-Aeruginosa* at 2.2-Angstrom Resolution, *Acta Crystallographica Section D-Biological Crystallography* *51*, 711-717.
23. Nicholls, A., Sharp, K. A., and Honig, B. (1991) Protein Folding and Association - Insights from the Interfacial and Thermodynamic Properties of Hydrocarbons, *Proteins-Structure Function and Genetics* *11*, 281-296.
24. Sharp, K. A., Nicholls, A., Friedman, R., and Honig, B. (1991) Extracting Hydrophobic Free-Energies from Experimental-Data - Relationship to Protein Folding and Theoretical-Models, *Biochemistry* *30*, 9686-9697.

25. Stultz, C. M., and Karplus, M. (2000) Dynamic ligand design and combinatorial optimization: Designing inhibitors to endothiapepsin, *Proteins-Structure Function and Genetics* 40, 258-289.
26. Moreira, I. S., Fernandes, P. A., and Ramos, M. J. (2006) Detailed Microscopic Study of the Full ZipA:FtsZ Interface, *Proteins: Structure, Function, and Bioinformatics* 63, 811-821.
27. Spector, S., Sauer, R. T., and Tidor, B. (2004) Computational and experimental probes of symmetry mismatches in the arc repressor-DNA complex, *Journal of Molecular Biology* 340, 253-261.
28. Floris, F., Persico, M., Tani, A., and Tomasi, J. (1995) Free energies and structures of hydrated cations, based on effective pair potentials, *Chemical Physics* 195, 207-220.
29. Boresch, S., Archontis, G., and Karplus, M. (1994) FREE-ENERGY SIMULATIONS - THE MEANING OF THE INDIVIDUAL CONTRIBUTIONS FROM A COMPONENT ANALYSIS, *Proteins-Structure Function and Genetics* 20, 25-33.
30. Wang, S. C., Dias, A. V., Bloom, S. L., and Zamble, D. B. (2004) Selectivity of Metal Binding and Metal-Induced Stability of *Escherichia coli* NikR, *Biochemistry* 43, 10018-10028.
31. Gomer, R., and Tryson, G. (1977) An experimental determination of absolute half-cell emf's and single ion free energies of solvation, *The Journal of Chemical Physics* 66, 4413-4424.
32. Berman, H., Henrick, K., and Nakamura, H. (2003) Announcing the worldwide Protein Data Bank, *Nature Structural Biology* 10, 980.
33. Emsley, P., and Cowtan, K. (2004) Coot: model-building tools for molecular graphics., *Acta Crystallogr. D* 60, 2126-2132.
34. Brooks, B. R., Bruccoleri, R. E., Olafson, B. D., States, D. J., Swaminathan, S., and Karplus, M. (1983) CHARMM: A Program for Macromolecular Energy, Minimization, and Dynamics Calculations, *J Comput Chem* 4, 187-217.
35. Foloppe, N., Sagemark, J., Nordstrand, K., Berndt, K. D., and Nilsson, L. (2001) Stabilization of the Catalytic Thiolate in a Mammalian Glutaredoxin: Structure, Dynamics and Electrostatics of Reduced Pig Glutaredoxin and its Mutants, *Journal of Molecular Biology* 310, 449-470.
36. Ryckaert, J.-P., Ciccotti, G., and Berendsen, H. J. C. (1977) Numerical integration of the cartesian equations of motion of a system with constraints: molecular dynamics of n-alkanes, *Journal of Computational Physics* 23, 327-341.

37. Brooks, C. L., Brunger, A., and Karplus, M. (1985) Active-Site Dynamics in Protein Molecules - a Stochastic Boundary Molecular-Dynamics Approach, *Biopolymers* 24, 843-865.
38. MacKerell, A., and Nilsson, L. (2001) Nucleic Acid Simulations, In *Computational Biochemistry and Biophysics* (Becker, O., MacKerell, A., Roux, B., and Wantanabe, M., Eds.), pp 441-464, Marcel Dekker, Inc., New York.
39. Brooks, C. L., and Karplus, M. (1983) Deformable Stochastic Boundaries in Molecular-Dynamics, *Journal of Chemical Physics* 79, 6312-6325.
40. Hoover, W. G. (1985) Canonical Dynamics - Equilibrium Phase-Space Distributions, *Physical Review A* 31, 1695-1697.
41. Young, M. A., Ravishanker, G., and Beveridge, D. L. (1997) A 5-nanosecond molecular dynamics trajectory for B-DNA: Analysis of structure, motions, and solvation, *Biophysical Journal* 73, 2313-2336.
42. Beglov, D., and Roux, B. (1994) Finite Representation of an Infinite Bulk System - Solvent Boundary Potential for Computer-Simulations, *Journal of Chemical Physics* 100, 9050-9063.
43. Tsui, V., Radhakrishnan, I., Wright, P. E., and Case, D. A. (2000) NMR and molecular dynamics studies of the hydration of a zinc finger-DNA complex, *Journal of Molecular Biology* 302, 1101-1117.
44. Stote, R. H., and Karplus, M. (1995) Zinc-Binding in Proteins and Solution - a Simple but Accurate Nonbonded Representation, *Proteins-Structure Function and Genetics* 23, 12-31.
45. Grottesi, A., Ceruso, M. A., Colosimo, A., and Di Nola, A. (2002) Molecular dynamics study of a hyperthermophilic and a mesophilic rubredoxin, *Proteins-Structure Function and Genetics* 46, 287-294.
46. Stultz, C. M., and Edelman, E. R. (2003) A structural model that explains the effects of hyperglycemia on collagenolysis, *Biophysical Journal* 85, 2198-2204.



## Chapter IV: Examining the Low Affinity Nickel Binding Sites of *Escherichia coli* NikR

### IV.A. Abstract

*Escherichia coli* NikR regulates cellular nickel uptake by binding to DNA in the presence of nickel and blocking transcription of genes encoding the nickel uptake transporter, NikABCDE. Early work on the NikR system revealed that NikR has two binding affinities for the *nik* operon (1, 2). When stoichiometric Ni<sup>2+</sup> binds NikR, the protein has an affinity for DNA in the nM range; however, when excess nickel ions are present NikR has a pM affinity for DNA (1, 2). While it is known that the stoichiometric nickel ions bind at the NikR tetrameric interface and order the  $\alpha$ 3 helix (3, 4), details of where excess nickel ions bind and how these nickel ions enhance NikR's affinity for DNA are unknown. We have solved the crystal structure of NikR in the presence of excess nickel to 2.6 Å resolution and have obtained nickel anomalous data in the presence of excess nickel for both NikR and the NikR structure co-crystallized with a 30 nucleotide piece of double stranded DNA containing the *nik* operon binding site for NikR. Anomalous maps calculated using data collected at the nickel peak (1.4845 Å) allow us to locate where the excess nickel ions bind on both NikR alone and the NikR-DNA complex. In the NikR alone structure, excess nickel ions bind on the surface of the protein with one to three protein ligands and at least two water molecules coordinating each site and induce no significant conformational change to the protein. To better define the coordination and geometry of each excess nickel site in the NikR-DNA complex structure, molecular dynamics simulations of the complex with 10 nickel ions bound at low affinity sites were conducted. These data suggest that low affinity nickel ions utilize between three and five water molecules and prefer an octahedral geometry. Given the lack of large conformational changes in the protein and the addition of more positive charge provided by the nickel ions to NikR, it seems likely that these sites play an electrostatic role in enhancing NikR's affinity for DNA. The work presented here completes the description of the metal binding sites on NikR and begins to describe how additional low affinity nickel binding sites on the surface of the protein could modulate NikR's affinity for the *nik* operon.

## IV.B. Introduction

Regulatory proteins play key roles within the cell, maintaining a crucial balance of nutrients and preventing the overload of any element or compound that could prove lethal to the cell at higher concentrations. One class of regulatory proteins is the ligand-binding transcription factor, which is often described as controlling gene expression in a strictly on/off manner. However, if a protein is able to fine tune the degree of gene repression or induction - rather than inducing a strictly on/off response - this would make for a highly efficient transcription factor. *Escherichia coli* NikR, the nickel-regulatory transcription factor, has been shown to have two distinct DNA binding affinities for its operon; nanomolar when stoichiometric nickel is bound and picomolar when excess nickel is present (1, 2). Understanding NikR's ability to maintain this model of multi-level regulation has been a point of interest in this system. One key unanswered question is how the low affinity nickel sites are coordinated on the protein-DNA complex and how they enhance NikR's affinity for DNA.

NikR is a homotetrameric protein composed of two types of domains: a central tetrameric metal binding domain (MBD) and two flanking dimeric ribbon-helix-helix (RHH) or DNA-binding domains (5). NikR has multiple types of metal binding sites: high affinity nickel binding sites for stoichiometric nickel (low picomolar affinity) (2, 6), potassium binding sites (4, 7), and low affinity nickel binding sites (30  $\mu$ M to 30 nM affinity) (1, 2). The four identical square-planar high affinity nickel binding sites are located at the central tetrameric interface in the MBD (5). These sites have been well characterized to prefer nickel over other metals available in the cell (1, 3, 6-8). When nickel ions bind to the high affinity sites, they order the helix  $\alpha$ 3 and the preceding loop, which then makes contacts to DNA, thereby initiating NikR-DNA binding (3, 4).

Upon DNA binding, two identical octahedral metal binding sites are formed between the MBD and RHH domains (4). Although nickel was not bound in this site in the NikR-DNA complex crystal structure (4), it was thought that this location could be the experimentally observed low affinity nickel binding site responsible for enhancing

NikR's affinity for DNA when excess nickel is present (8, 9). However, recent calculations examining metal stability, charge, and size preference suggest that these second metal binding sites are optimized for potassium binding and that potassium is required at the secondary site for high affinity binding to DNA (7). Recent biochemical studies confirm these observations in that they suggest that NikR cannot bind DNA in the absence of potassium (10). Thus, there is an emerging consensus that  $K^+$  is responsible for stabilizing the RHH domains in a "down" DNA-binding conformation.

The third type of metal binding sites on NikR are the low affinity nickel binding sites where excess nickel ions bind, enhancing NikR's affinity for the DNA operon from nanomolar to picomolar (1, 2). In this paper we locate and describe these sites and begin to understand how they can account for NikR's enhanced DNA affinity. Using X-ray crystallography and nickel anomalous maps, potential low affinity nickel sites on NikR were identified. To visualize these sites on the NikR-DNA complex, we utilized a combination of the low-resolution X-ray anomalous data and molecular modeling. Through this work, one can begin to consider the relevance of these sites towards tuning NikR's DNA affinity more precisely than a simple on/off mode for transcriptional regulation.

#### **IV.C. Results**

##### *IV.C.1. Crystal structure of NikR in the absence of DNA soaked with 8 mM NiCl<sub>2</sub>*

To visualize the low affinity nickel binding sites, we soaked stoichiometric  $Ni^{2+}$ -NikR crystals with excess nickel chloride and collected data at the nickel peak wavelength (1.4845 Å). We were not able to co-crystallize NikR or the NikR-DNA complex with excess nickel due to precipitation of the protein under these conditions. Similar to the stoichiometric  $Ni^{2+}$ -bound full-length NikR, the excess nickel soaked NikR data indicated a dimer, or half of the full NikR tetramer, in the same asymmetric unit (asu) and in the P3<sub>1</sub>21 space group. Data collection and processing statistics are listed in Table IV.1. The overall fold of NikR did not change upon soaking with excess  $Ni^{2+}$ , with an all-atom root

mean square (rms) deviation of 0.50 Å between the stoichiometric and excess Ni<sup>2+</sup> soaked structures.

**Table IV.1.** Data refinement and processing statistics for NikR and NikR-DNA complex with low affinity nickel sites filled and data processing statistics for NikR with low affinity sites filled. Both data sets were scaled anomalously.

Crystal	NikR soaked with 8 mM NiCl <sub>2</sub>	NikR-DNA soaked with 5 mM NiCl <sub>2</sub>
Space Group	P3 <sub>1</sub> 21	C2
<b>Cell Dimensions</b>		
A (Å)	50.73	199.62
B (Å)	50.73	82.29
C (Å)	183.07	125.73
A (°)	90	90
β (°)	90	104.74
γ (°)	120	90
Wavelength (Å)	1.4845	1.4862
Temperature (K)	100	100
Resolution Range (Å) <sup>1</sup>	50-2.6 (2.69-2.60)	20-3.6 (3.73-3.60)
Unique Reflections <sup>1</sup>	8682 (649)	43937 (3843)
Average Redundancy	9.3	3.3
Completeness (%) <sup>1</sup>	98.3 (89.3)	97.5 (85.6)
I / σ(I) <sup>1</sup>	16.3 (4.5)	14.3 (1.6)
R <sub>sym</sub> (%) <sup>1,2</sup>	8.9 (28.8)	10.6 (47.1)
# NikR monomers per asu	2	8
R <sub>cryst</sub> (R <sub>free</sub> ) (%) <sup>3</sup>	23.1 (28.7)	
<b>Average B-factor (Å<sup>2</sup>)<sup>4</sup></b>		
overall	71.7 (2105)	
protein	70.0 (199)	
high affinity nicks	70.5 (2)	
excess nicks	138 (9)	
waters	59.7 (63)	
detergent molecule	154.6 (32)	
<b>rms deviations</b>		
bond lengths (Å)	0.011	
bond angles (°)	1.2	
<b>Ramachandran plot (%)</b>		
most favored	84.2	
additionally allowed	14.6	
generously allowed	0.8	
disallowed	0.4	

<sup>1</sup>The number in parentheses is for the highest resolution shell.

<sup>2</sup> $R_{\text{sym}} = \sum_{hkl} |I_{(hkl)}^i - \langle I_{(hkl)} \rangle| / \sum_{hkl} \langle I_{(hkl)} \rangle$ , where  $I_{(hkl)}^i$  is the  $i^{\text{th}}$  measured diffraction intensity and  $\langle I_{(hkl)} \rangle$  is the mean of the intensity for the miller index (hkl).

<sup>3</sup> $R_{\text{cryst}} = \sum_{hkl} ||F_o(hkl)| - |F_c(hkl)|| / \sum_{hkl} |F_o(hkl)|$ .  $R_{\text{free}} = R_{\text{cryst}}$  for a test set of reflections (5%) not included in refinement.

<sup>4</sup>Numbers in parentheses are the number of atoms in each category.



The nickel anomalous maps generated from the structure following the soaking experiment indicate nine potential low affinity nickel-binding sites on the surface of the NikR protein (Figure IV.1a). Due to the symmetry of the dimer, the nine sites can be categorized into five site types on NikR. The site types are numbered on Figure IV.1a and correspond to the descriptions in Table IV.2. After refining the NikR structure, we were able to estimate the occupancies of each of the low affinity sites as described in the Methods section. Nickel ions in the stoichiometric or high affinity sites (site type 0) refine to nearly 100 % occupancy while the nickels in the potential low affinity nickel sites have varying occupancies (47-99 %) (Table IV.2). These sites are described in detail in IV.C.3.

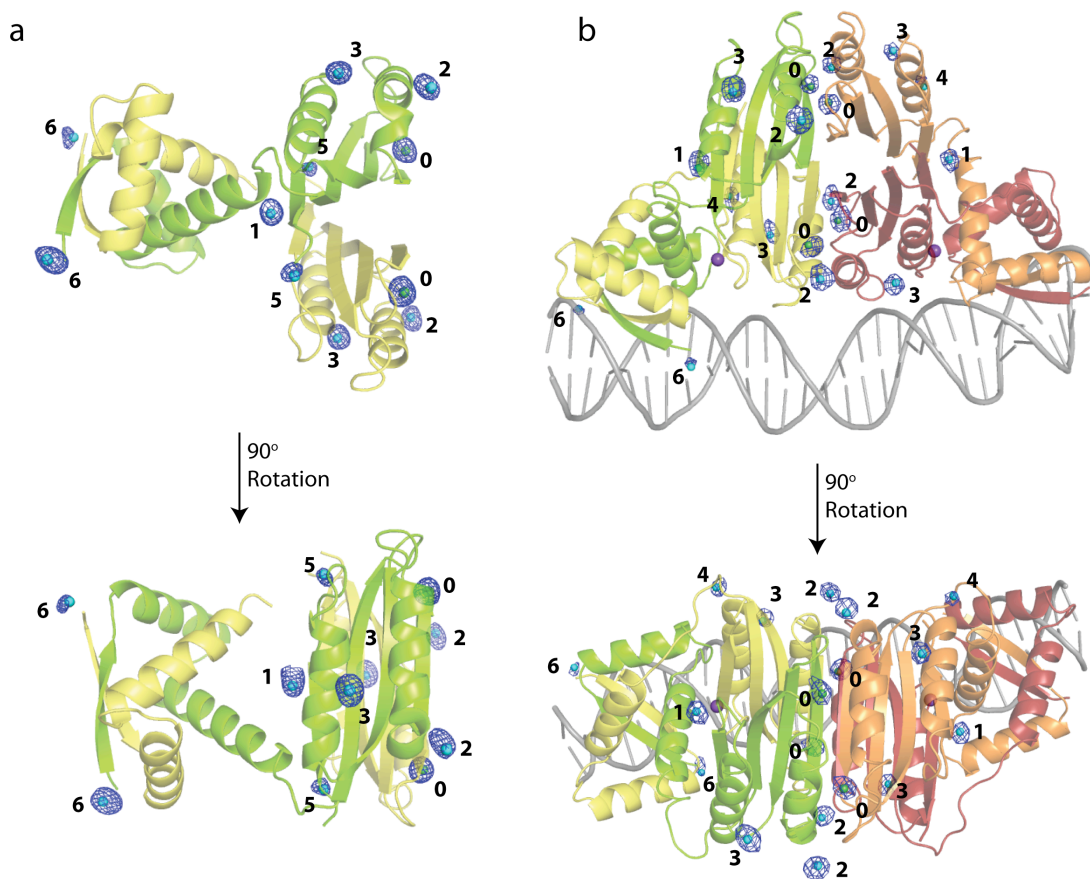
**Table IV.2.** Descriptions of the types of low affinity nickel sites seen in the NikR and NikR-DNA complex structures. Site type numbers correspond to sites in Figure IV.1. Site types 0-3 and site type 6 are in both structures, site type 4 is only in the NikR-DNA complex structure and site type 5 is only in the structure of NikR alone.

Site Type Number	Description	# sites per NikR dimer <sup>1</sup>	# sites per NikR-DNA tetramer <sup>1</sup>	Protein ligands from crystal structure	Average Occupancy	Average anomalous signal <sup>2</sup>	
0	High Affinity Site	2 (2)	4 (4)	H87, H89, C95, H76'	0.99	22	7
1	Low Affinity site 1	1 (1)	2 (2)	H125, H125'	0.79	20	7
2	Low Affinity site 2	2 (2)	4 (4)	H79, H92'	0.67	15	7
3	Low Affinity site 3	2 (2)	4 (4)	H110, D114, H78	0.87	22	7
4	NikR-DNA only site	0 (2)	2 (4)	H48	N/A	0	3
5	NikR only site	2 (2)	0 (4)	H123	0.47	7	0
6	N-terminal site	2 (2)	2 (4)	M1	0.57	19	2

<sup>1</sup>The number in parentheses is the total possible number of each type of site on the NikR dimer or NikR-DNA tetrameric complex.

<sup>2</sup>Average anomalous signal refers to the average maximum  $\sigma$  level of the nickel anomalous map at which density for a given ion disappears. Sigma levels determined from the nickel anomalous map for the NikR structure with excess nickel ions (maximum sigma = 25  $\sigma$ ) are listed in the left column and sigma levels from the nickel anomalous map for the NikR-DNA complex structure with excess nickel ions (maximum sigma = 10  $\sigma$ ) are listed in the right column. For site types 4, 5, and 6, which have at least one potential site empty in either the NikR alone or NikR-DNA structure, 0 was averaged in for each empty site.

**Figure IV.1.** Nickel anomalous density maps of excess nickel soaked NikR and NikR-DNA complex. (a) Dimer found in the asymmetric unit of the NikR structure with excess nickel ions. (b) NikR-DNA complex structure with excess nickel ions. Nickel anomalous density is shown in blue mesh at  $3.5 \sigma$ . Excess nickel ions are indicated as cyan spheres, high affinity nickel ions in green spheres, and potassium ions in purple spheres. Each monomer chain is colored uniquely. Nickel sites are numbered corresponding to the site types in Table IV.2.



#### IV.C.2. Nickel anomalous density in the NikR-DNA structure soaked with 5 mM $\text{NiCl}_2$

The excess nickel soaked NikR-DNA crystals indexed in the same space group, C2, as the published NikR-DNA complex, yet with sufficiently different cell parameters such that simple rigid body refinement was not possible to solve the phase problem (4). Thus, the phases were determined with molecular replacement using a single copy of the

published NikR-DNA complex as the search model (4). Data collection statistics are listed in Table IV.1. The low resolution of this crystal structure (3.6 Å) and poor data quality did not warrant refinement past the initial molecular replacement solution. However, phases found using molecular replacement were used to calculate a nickel anomalous map, which indicated the location of the excess nickel ions (Figure IV.1b). Comparing the low affinity sites from the NikR-DNA complex structure with the structure of NikR alone, we find that most sites are conserved (site types 1-3 and site type 6 described in Figure IV.1 and Table IV.2).

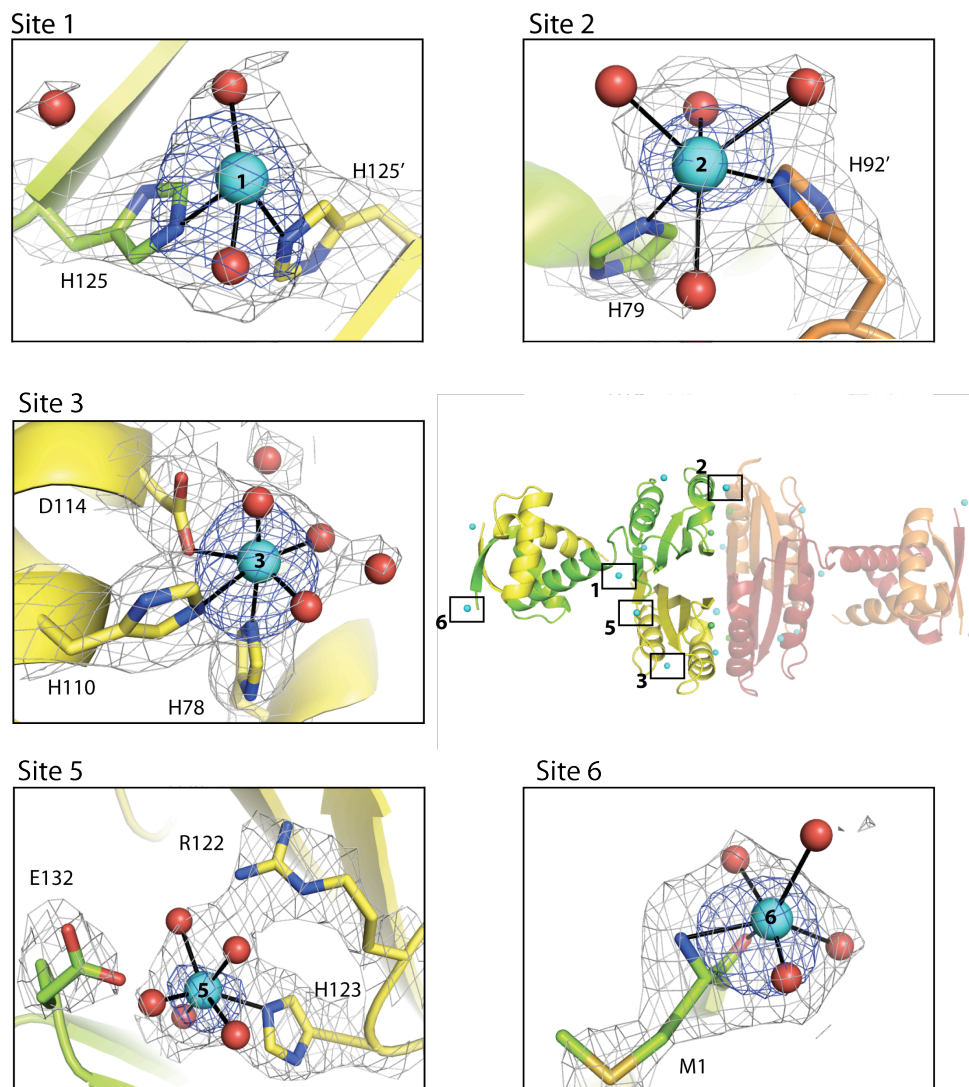
#### *IV.C.3. Low affinity Ni<sup>2+</sup> sites from the crystal structures*

From an analysis of both the NikR alone and NikR-DNA complex structures with excess nickel ions, there are a total of six types of low affinity nickel sites, five of which have clear  $2F_o - F_c$  electron density for coordinating ligands because these sites are present in the 2.6 Å NikR structure in the absence of DNA (Figure IV.1a, site types 1-3 and 5,6). Site type 1 is present in both structures and corresponds to a nickel ion coordinated by two H125 ligands, one from each of the monomers composing the NikR dimer (Figure IV.1, IV.2). There is  $2F_o - F_c$  electron density for two water molecules acting as additional ligands to the nickel (Figure IV.2). While these sites are solvent accessible, they are the most buried of all the observed excess nickel binding sites. Site type 1 is well-coordinated with four ligands to the nickel ion and has an average occupancy of 0.79 in the NikR structure with strong nickel anomalous electron density peaks in both the NikR and NikR-DNA complex structure (Figure IV.1, Table IV.2).

Site type 2 is located in a central region of the structure near the tetrameric interface. Each site is coordinated by H79 of one monomer and H92 from the monomer across the tetrameric interface (Figure IV.2). Four water molecules visible in the electron density maps complete an octahedral geometry around the nickel ion (Figure IV.2). The occupancies of the type 2 sites refine to an average of 0.67, indicating that the site is filled about 2/3 of the time in the NikR structure (Table IV.2). Although the occupancy is

somewhat lower than site types 1 and 3, there is nickel anomalous density at every potential site type 2 location in both the NikR and NikR-DNA complex (Figure IV.1).

**Figure IV.2.** Low affinity nickel sites 1-3, 5 and 6 from the crystal structure of NikR without DNA.  $2F_o - F_c$  electron density maps at  $1.0 \sigma$  are shown in grey around the coordinating protein ligands, water molecules, and metal ions. Nickel anomalous density maps at  $3.5 \sigma$  are shown in blue. Coloring is the same as in Figure IV.1. The low affinity nickel sites are numbered and correspond to the sites numbered in the NikR model (middle right) as well as the sites in Figure IV.1 and Table IV.2.



Coordinated by H110, H78, and D114 from the same monomer, site type 3 also has nickel anomalous density to at least 20  $\sigma$  in both monomers of the NikR dimer (max signal at 25  $\sigma$ ) and at least 6  $\sigma$  in all four monomers of the NikR-DNA complex (max signal at 10  $\sigma$ ) (Figure IV.1; Table IV.2). This site utilizes three amino acid ligands and three water ligands, creating a common octahedral geometry for the nickel ion (Figure IV.2). This excess nickel binding site appears to be filled in the majority of NikR monomers within the crystal, with an average occupancy of 0.87.

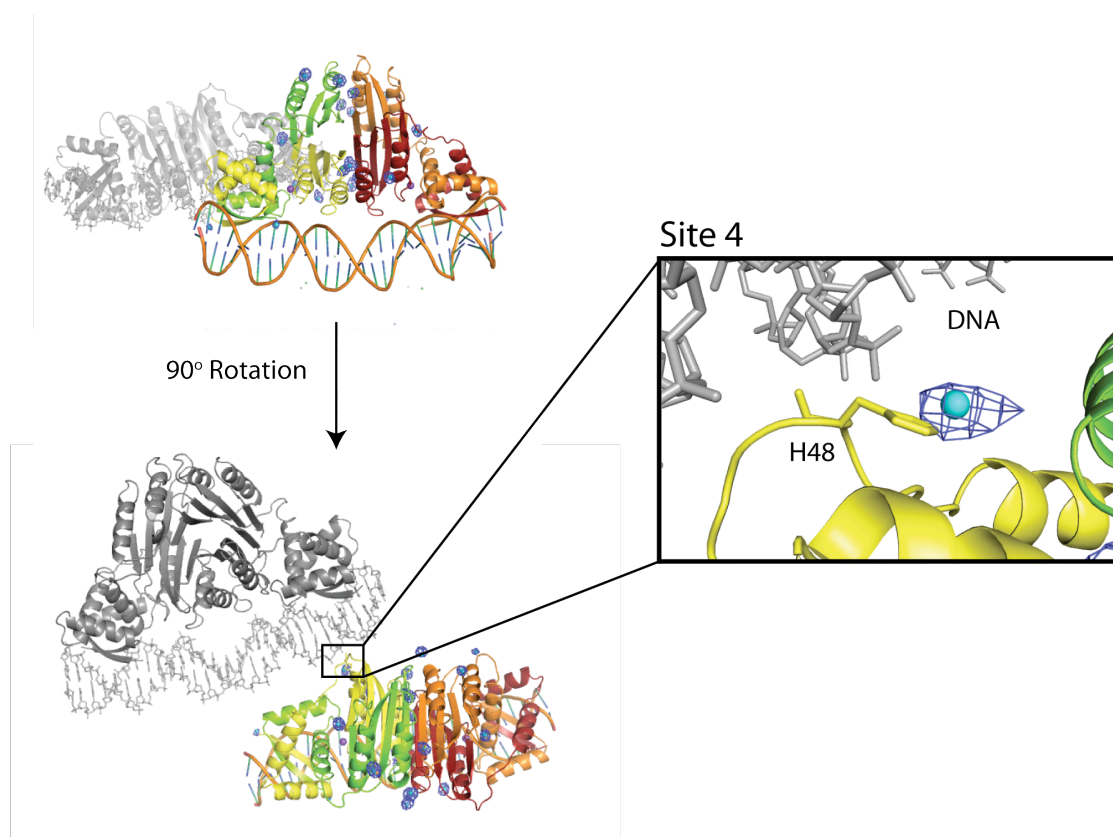
Since site type 4 is only visualized in the nickel anomalous maps of the NikR-DNA complex, the exact coordination of this site is undetermined. However, nickel is likely to be coordinated by nearby H48. This site is stabilized by crystal contacts with a symmetry-related DNA molecule (Figure IV.3). Such stabilizing contacts could explain why this site is only occupied in the NikR-DNA complex crystal structure and suggest that this site may not be a true low affinity nickel binding site. In addition, only two of the four H48 residues in the molecule have associated nickel anomalous density (Figure IV.1), and intensities of the nickel anomalous signal, when present, are weak (Table IV.2). The average nickel anomalous level of site type 4 is 3  $\sigma$ , in comparison to site types 1-3 that have peaks visible to 7  $\sigma$ . Because this site is not present in the NikR structure, it was not possible to refine the occupancy of a nickel ion in this site.

The low affinity nickel site present only in the NikR structure without DNA, site type 5, is also coordinated by a histidine, specifically H123. An octahedral geometry is completed at this site by five water molecules, which are stabilized by R122 and other nearby residues (Figure IV.2). This site is occupied in less than half of the NikR monomers in the crystal with a refined average occupancy of 0.47 (Table IV.2).

Site type 6 is located at the N-terminus of the protein and is the only excess nickel binding site not coordinated by a histidine residue. Instead, the N-terminal amine and carbonyl from M1 and water molecules coordinate site type 6 in an octahedral geometry (Figure IV.2). While this site is present in both structures, the anomalous density for it is

very weak in the NikR-DNA structure with an average nickel anomalous density of  $2 \sigma$  (Table IV.2) and is empty in two of the four possible locations (Figure IV.1b).

**Figure IV.3.** Low affinity nickel site 4 is stabilized by a crystallographically-related DNA molecule. NikR-DNA crystal structure shown in Figure IV.1 is again shown in color with nickel anomalous maps for orientation. The grey NikR-DNA molecule is a crystallographically related molecule whose DNA helps stabilize site 4 on the neighboring NikR-DNA complex. DNA and H48 are in stick form for reference (inset), the rest of the structure is represented in cartoon form.

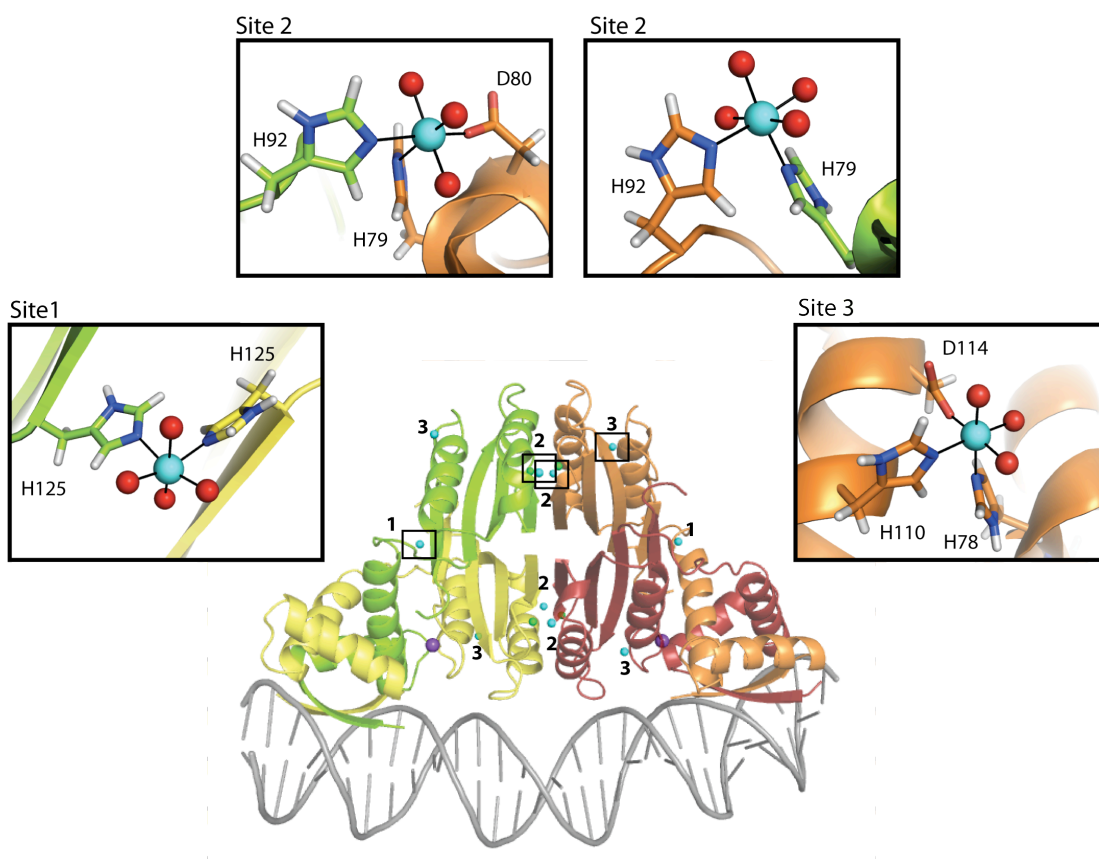


#### IV.C.4. Molecular dynamics simulations of site types 1-3 on the NikR-DNA complex

A 1 ns molecular dynamics trajectory of the solvated NikR-DNA complex yielded representative structures of the complex when nickel ions were bound at the three most highly occupied low affinity nickel sites (site types 1-3). Throughout the dynamical trajectory, all low affinity sites (10 sites were modeled based on the 3 site types)

maintained an octahedral geometry (Figure IV.4). Type 1 sites maintained the two H125 ligands and the two water molecules seen in the crystal structure and gained two additional water ligands (Figure IV.4). Type 2 sites maintained the original protein ligands, H92 and H79, with either four water molecules or three water molecules and a sixth coordination ligand to complete the octahedral geometry. The third coordinating protein ligand (D80) was not present in the crystal structure (Figure IV.4). Finally, type 3 sites maintained a nearly identical geometry to what was seen in the crystal structure with the same protein ligands and same number of water molecules (Figures IV.2 and IV.4).

**Figure IV.4.** Representative structures following 1 ns molecular dynamics simulation of three types of low affinity nickel binding sites. Simulations resulted in two types of ligand arrangements for site 2. Site types correspond to numbers in Figure IV.1 and Table IV.2.



#### IV.D. Discussion

Playing a crucial role in metal homeostasis in the cell, metalloregulatory transcription factors have proven to be much more complex than one may originally have imagined. *E. coli* NikR, for example, has three types of metal binding sites: high affinity nickel binding sites, potassium binding sites, and low affinity nickel binding sites. While prior work has outlined the location and role of the stoichiometric or high affinity nickel sites (2-6, 8) and the second, K<sup>+</sup> containing metal binding sites (4, 7, 10), until now, the exact locations, coordination states, and mechanism of action of the third type of metal binding site on NikR—the low affinity sites where excess nickel ions bind to enhance NikR's affinity for DNA—have not been thoroughly described. This work therefore serves to complete the description of NikR's metal binding sites.

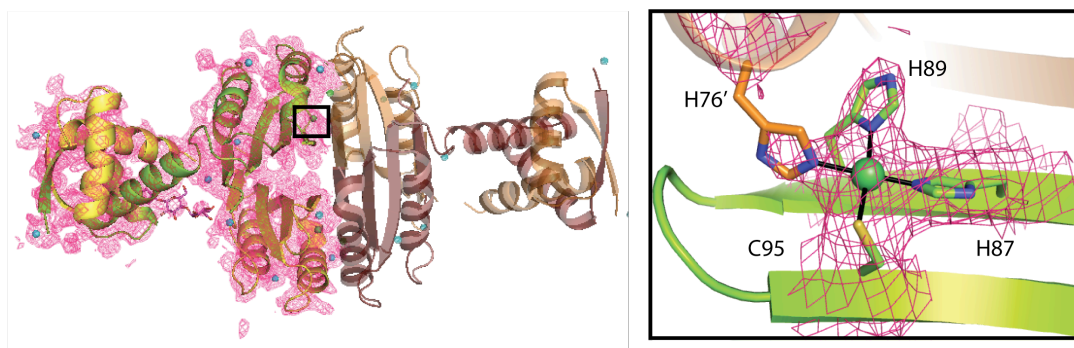
Nickel anomalous maps for NikR and the NikR-DNA complex soaked with excess nickel indicate six types of potential low affinity nickel sites on NikR. These sites are all on the surface of the protein and five of the six site types have at least one histidine ligand (Table IV.2), and all nickels are coordinated by oxygen containing ligands, typically water molecules. Most sites in the crystal structures are six-coordinate, consistent with XAS data on the low affinity nickel sites which is best fit with a model where the low affinity sites are 6-coordinate with N and O donors as ligands (8). There are data that support the low affinity sites on NikR being nickel-specific binding sites (1), and although our work here does not directly address the question of specificity, it is important to note that histidine is a common nickel ligand (11). Located across the surface of NikR, one can envision a variety of roles for these sites. Since site type 1 is located near the RHH-MBD interface, it is important to consider whether this site could play a role in stabilizing these domains in a DNA-bound conformation. Comparison of site type 1 in the NikR alone (“out” orientation) and NikR-DNA complex structure (“down” orientation), however, shows that this site does not change when the RHH domains are in the two different orientations (Figure IV.1), suggesting that this site does not play a role in stabilizing a DNA-bound form of NikR. Previous work has indicated that ordering of the  $\alpha$ 3 helix (residues 65-78) is important for NikR binding to DNA and



both low affinity site types 2 and 3 utilize residues from the  $\alpha 3$  helix or the following loop (3, 4). A possible mechanism explaining how the binding of excess nickel ions stabilizes the NikR-DNA complex could be their ability to further stabilize the  $\alpha 3$  helix. However, stoichiometric nickel alone does not order the  $\alpha 3$  helices as indicated by circular dichroism spectroscopy and B-factor comparison (3, 5, 6). In the apo crystal form of NikR the B-factors of the  $\alpha 3$  helical residues are significantly greater than the rest of the protein ( $88 \text{ \AA}^2$  vs.  $62 \text{ \AA}^2$ ), whereas in the stoichiometric  $\text{Ni}^{2+}$ -bound forms the B-factors of the  $\alpha 3$  helical residues are very similar to the average B-factor of the protein ( $33 \text{ \AA}^2$  vs.  $28 \text{ \AA}^2$ ) (12). Moreover, the lack of significant conformational changes when nickel ions bind at the low affinity sites is consistent with the notion that the enhanced DNA affinity afforded by these nickel ions can largely be attributed to an electrostatic effect where the positively charged nickel ions increase NikR's affinity for the negatively charged DNA.

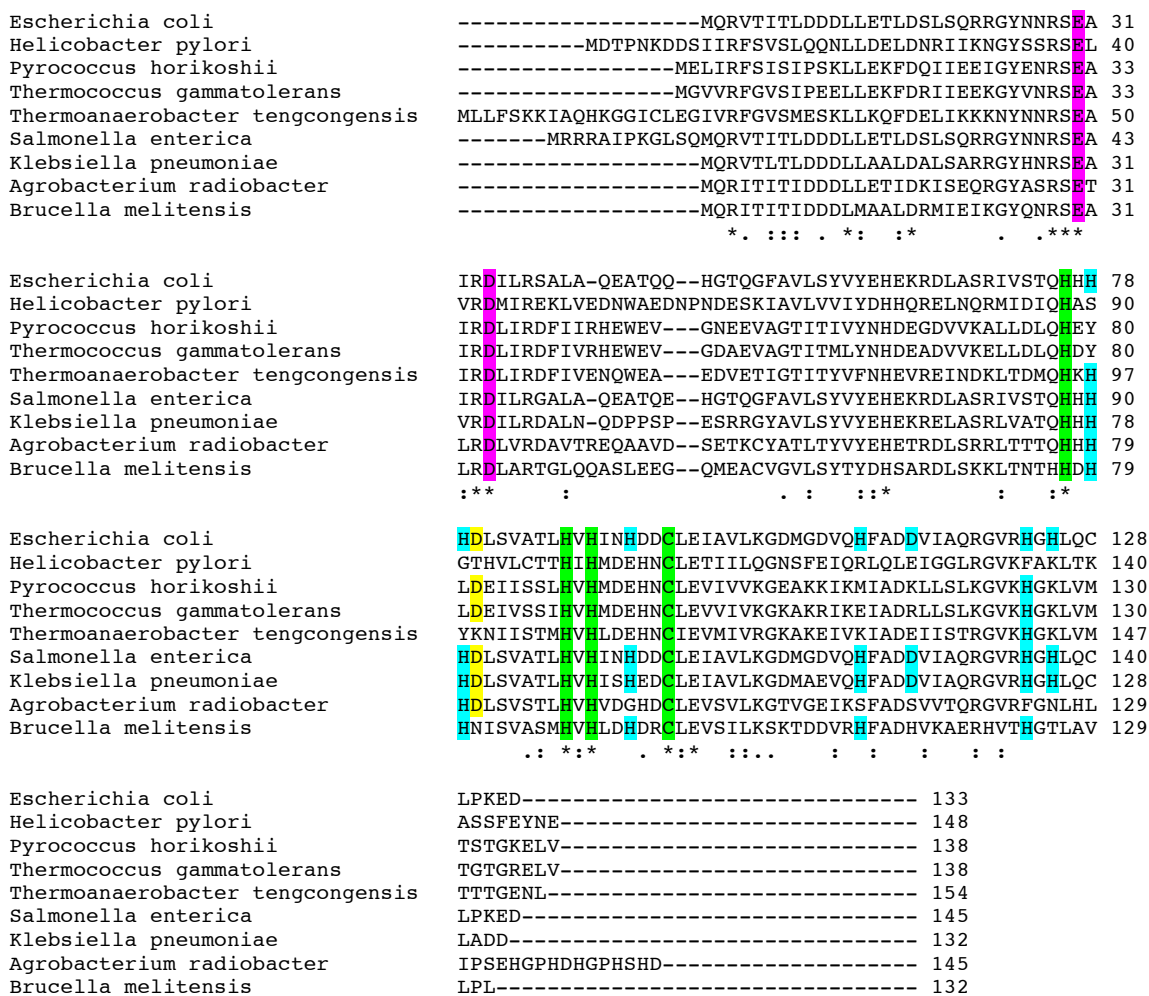
Our structural data are consistent with these surface nickel sites being low affinity sites. The refined occupancies for these nickel binding sites, and in some cases the weak nickel anomalous density (peaks disappear at relatively low sigma levels), suggest that these sites are not filled 100% of the time (Figure IV.1 and Table IV.2). The incomplete occupancies are consistent with all sites being solvent exposed and not maintaining a coordination sphere of exclusively protein ligands. The greatest number of protein ligands used by any given site is three as is seen in site type 3, which also has the highest occupancy of nickel out of all the low affinity sites (0.87), consistent with the notion that a larger number of coordinating protein ligands correlates with increased site stability (Figure IV.2 and Table IV.2). However, no low affinity site has an occupancy for nickel as high as at the high affinity sites, which utilize only protein ligands (Figure IV.5 and Table IV.2). One can imagine that the weaker affinity of these surface nickel sites enables them to act as a 'sink' for extra nickel ions in the cell, allowing  $\text{Ni}^{2+}$  to easily dissociate in case more nickel is required for use by other nickel proteins.

**Figure IV.5.** Representative composite omit density in the NikR structure with excess nickel. The NikR structure with excess nickel ions is shown on the left and a close up of one of the four high affinity nickel sites is shown on the right. The dimer from the asu is shown in green and yellow with the composite omit map contoured at  $1.0 \sigma$  in pink. The crystallographically related dimer in orange and red is shown for orientation. The composite omit map around the high affinity nickel site and four coordinating ligands is also contoured at  $1.0 \sigma$  (inset). Coloring is the same as in Figures IV.1 and IV.2 with the detergent molecule shown in stick form with magenta bonds (left).



The crystallographic data described here suggest that there is not a single low affinity nickel site on NikR, but rather a number of low affinity nickel binding sites. Interestingly, a comparison of the results from gel shift assays studying the excess nickel binding effect on *Helicobacter pylori* NikR and *E. coli* NikR, indicates that *H. pylori* NikR does not exhibit an enhanced DNA binding affinity in the presence of excess nickel ions (1, 2, 13). A sequence alignment of a variety of NikR proteins including *H. pylori* and *E. coli* NikR illustrates that while the ligands to the high affinity nickel site and the potassium binding site are conserved between all species, the histidine residues that act as ligands to the low affinity nickel sites in *E. coli* NikR are not present in *H. pylori* NikR and a number of other NikR proteins (Figure IV.6). Therefore, it is likely that *H. pylori* NikR does not respond to excess nickel because, unlike *E. coli* NikR, it does not possess low affinity nickel sites.

**Figure IV.6.** Sequence alignment of NikR from a variety of bacteria, including *Escherichia coli* and *Helicobacter pylori*. High affinity nickel ligands are highlighted in green, potassium ligands in purple and low affinity nickel site ligands from crystal structures in cyan, and the ligand added to site type 2 during molecular dynamics simulations (D80) in yellow (refer to Figure IV.4).



While the lack of sequence conservation of the histidine residues composing these sites could indicate that the “low affinity nickel” is not physiologically relevant (Figure IV.6), it is interesting to consider possible reasons for a species dependent “low affinity nickel” effect. In *E. coli*, where NikR’s only known function is to repress the transcription of a

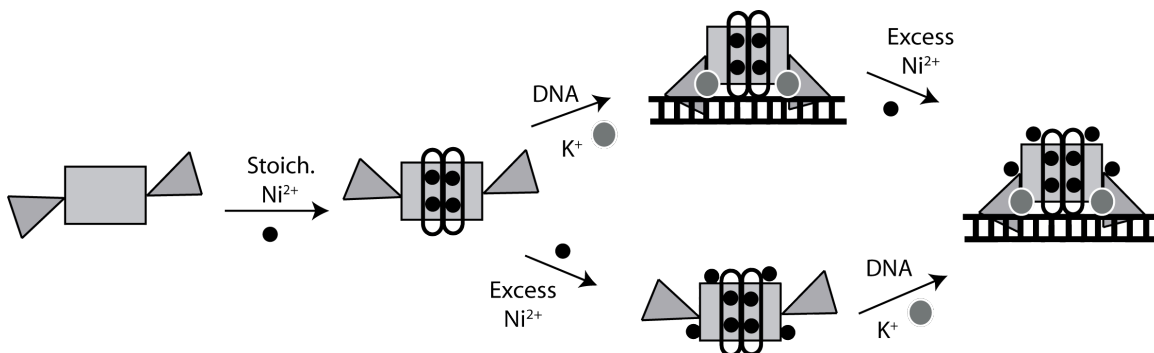
nickel-uptake transporter, NikR's affinity for its DNA target upstream of the *nik* operon can be tuned from nM to pM depending on the concentration of nickel in the cell. In *H. pylori*, NikR plays a variety of roles, down-regulating a nickel uptake protein, NixA, while also being responsible for inducing the transcription of a number of nickel-utilization genes (14-18). Given this difference in function between NikR from *E. coli* and *H. pylori*, the lack of conservation does not necessarily tell us about the importance of these sites in *E. coli*.

Although our data suggest potential locations for the low affinity nickel sites described by *in vitro* experiments, they do not directly address whether this “low affinity nickel” phenomenon is physiologically relevant. The issue of whether this “low affinity nickel” effect is relevant *in vivo* is complicated by the fact that it has not been possible to measure the levels of *nikABCDE* transcription as a function of cellular nickel concentration. In addition, values for the affinity of excess nickel for NikR differ widely depending on the technique used (apparent  $K_d$ 's of 30  $\mu$ M and 30 nM have both been measured (1, 2)). Finally, we do not know how these apparent  $K_d$ 's relate to the specific sites that we observe. The apparent  $K_d$  may represent an average of all sites or just some sites; thus it is difficult to predict how any one “low affinity nickel” site would compete for a nickel ion against other nickel binding proteins or other empty NikR high affinity sites (which have a pM affinity for  $\text{Ni}^{2+}$ ) (2, 6). It is unlikely that the nickel concentration in an *E. coli* cell would ever be high enough that one NikR tetramer could compete with all other nickel proteins such that the structure depicted in Figure 1V.1b, with fourteen surface nickels, would ever be realized. However, any one nickel site on the NikR surface with a  $K_d$  for nickel in the nM or  $\mu$ M range could be physiologically relevant. The sites identified here are easily accessible to excess nickel ions in the cell, even if NikR is already bound to DNA. Also, our studies show that many of these sites can be occupied by a nickel ion either when NikR is free or bound to DNA, suggesting that these sites can either increase NikR's affinity for DNA by facilitating the binding interaction of NikR for its operon or by stabilizing the bound NikR-DNA complex. In this sense, it seems

feasible that these sites could be physiologically relevant, helping NikR tune its affinity for the *nik* operon with respect to the level of nickel in the cell.

In conclusion, our data show that excess nickel ions bind to the surface of NikR in sites that are in agreement with the observed low affinity nickel binding. The binding of nickel ions to these sites does not induce significant conformational changes in the protein. These data are consistent with the notion that nickel binding at low affinity sites enhances NikR's affinity for DNA primarily through an electrostatic effect. Hence, NikR appears to use three distinct ion binding sites to regulate its affinity to its operator (Figure IV.7). Stoichiometric or high affinity nickel ions assist in stabilizing the folded state of the  $\alpha 3$  helix and preceding loops which are disordered when no metal or the incorrect metal is bound (Figure IV.7) (3, 5). The ordered helices and preceding loops can then make non-specific hydrogen bonding contacts with the phosphate backbone, localize NikR on DNA (3, 4). The  $K^+$  binding to the octahedral sites at the interface of the MBD/RHH domains helps to stabilize the RHH domains in a "down" DNA-binding conformation (4, 7) (Figure IV.7). Low affinity nickel sites on the exterior of the protein further enhance the affinity of the protein to the operator, potentially through an electrostatic mechanism (Figure IV.7). By considering the final series of metal binding sites on NikR, we now present a detailed mechanism of action for this metal responsive transcription factor, assisting in our understanding of cellular metalloregulation.

**Figure IV.7.** Proposed scheme for NikR binding DNA considering all three types of metal binding sites. Nickel ions are represented by black circles, potassium ions by grey circles, DNA as a ladder, the RHH domains as triangles, and the central MBD as a rectangle. Open ovals represent ordered  $\alpha 3$  helices. Stoichiometric amounts of  $\text{Ni}^{2+}$  binding at the high affinity sites are responsible for ordering the central  $\alpha 3$  helices and the preceding loops (open ovals). Ordered loops make hydrogen-bonding contacts with the DNA phosphate backbone and residues in the ribbons of the RHH domains make site-specific contacts with nucleotides at the DNA binding sites. The DNA-binding conformation of NikR creates  $\text{K}^+$  binding sites, which help stabilize NikR in the DNA-binding orientation. Finally, any excess nickel ions in the cell can bind to the surface of the protein, enhancing NikR's affinity for the *nik* operon. It is unclear if the excess nickel ions bind to the protein before or after DNA binding—but both possibilities are accounted for in this figure.



## IV.E. Methods

### IV.E.1. Refinement of crystal structure of *NikR* soaked with 8 mM $\text{NiCl}_2$ and identification of nickel sites

Full-length selenomethionine-labeled *E. coli* NikR with stoichiometric  $\text{Ni}^{2+}$  bound was purified and crystallized as previously described (4, 5). NikR crystals were soaked in precipitation solution (200 mM  $\text{MgCl}_2$ , 100 mM HEPES, 30% vol/vol polyethylene glycol (PEG 400), 0.5 ml of 345 mM of detergent molecule cyclohexyl-propyl-b-D-maltoside

(CYMAL-3)) supplemented with 8 mM NiCl<sub>2</sub> at room temperature for 70 min and then cryo-cooled to 100 K in a gaseous N<sub>2</sub> stream. Co-crystallization was not a possibility because of protein precipitation under high nickel concentrations. A dataset was collected on this crystal at the nickel peak wavelength (1.4845 Å) at beamline 5.0.2 of the ALS and processed keeping Friedel mates separate using DENZO/SCALEPACK (19).

The unit cell did not change significantly between the structure of stoichiometric Ni<sup>2+</sup>-NikR (PDB 2HZA) and the structure of NikR soaked with excess nickel. Thus, the stoichiometric Ni<sup>2+</sup>-bound NikR structure with waters removed was refined against this dataset using CNS (4, 20). Rigid body refinement of the whole structure and individual domains was followed by simulated annealing, positional, and individual B-factor refinement for a final R<sub>work</sub>/R<sub>free</sub> of 23.1/28.7 with no sigma cutoff. Data collection and refinement statistics are given in Table IV.1. The final model contains two protein chains, both missing the last C-terminal residue and one chain missing residues 46-48, which lie on a loop region connecting the RHH and MBD and are also disordered in the stoichiometric Ni<sup>2+</sup>-bound NikR structure (4). The model also contains a total of 11 nickel ions—2 bound at the high affinity sites and 9 bound at low affinity sites, one copy of the detergent molecule CYMAL-3, and 63 water molecules. Phases from the refined model were used to calculate an anomalous difference Fourier map in CNS to locate the positions of all nickel ions in the structure. A 3.5  $\sigma$  contour of this map with the two crystallographically unique NikR subunits is shown in Figure IV.1a. Following positional and B-factor refinement of the structure, each nickel ion was assigned a B-factor corresponding to the average B-factor of the structure at that point of refinement (70 Å<sup>2</sup>) and the occupancies of the nickel ions were sequentially refined (Table IV.2). Composite omit, 2F<sub>o</sub>-F<sub>c</sub>, and F<sub>o</sub>-F<sub>c</sub> difference maps were used throughout refinement to verify the structure (an example of the composite omit map density is shown in Figure IV.5). Figure IV.2 shows the low affinity sites in the NikR alone structure with 2F<sub>o</sub>-F<sub>c</sub> electron density and anomalous nickel density, illustrating the quality of density that was used to model the nickel ligands.

#### *IV.E.2. Identifying nickel sites on a NikR-DNA complex using anomalous scattering from low resolution X-ray data*

While it was not possible to obtain a high resolution structure of NikR bound to DNA with excess nickel ions, the low resolution structural information and nickel anomalous maps were used to locate nickel sites on the NikR-DNA complex. Crystals of NikR-DNA with stoichiometric Ni<sup>2+</sup> bound were grown as described previously (4). One such crystal was soaked in precipitant solution (200 mM KCl, 50 mM MgCl<sub>2</sub>, 50 mM Tris at pH 7.5, 10% wt/vol PEG 4,000) supplemented with 5 mM NiCl<sub>2</sub> at room temperature for 60 min before cryoprotection with 25% ethylene glycol and cryo-cooling in a gaseous N<sub>2</sub> stream at 100 K. A dataset was collected on this crystal at the nickel peak wavelength (1.4862 Å) at beamline X29A of the NSLS and processed anomalously using DENZO/SCALEPACK (19). Data processing statistics are listed in Table IV.1.

There was a significant change in the unit cell upon soaking with excess nickel, so simple rigid body refinement with the previous NikR-DNA structure (PDB 2HZV) was not successful. Thus, we used molecular replacement in Phaser with a single copy of the NikR-DNA complex structure (PDB 2HZV) and with waters removed as the search model (4, 21). Two copies of the NikR-DNA complex were found in the asymmetric unit (asu), resulting in a Z-score of 27. Further refinement of the structure was attempted in CNS, but poor data quality, likely due to the change in cell dimensions resulting from the nickel soaking, prevented full refinement of the structure. However, when phase information from molecular replacement is combined with the anomalous data, the resulting nickel anomalous map illustrates the approximate location of the nickel ions (Figure IV.1b). Many of these sites are also observed in the NikR alone structure (Table IV.2, Figure IV.1a). Only one site (site 4) was present in the NikR-DNA complex but not in the NikR alone structure and this site has comparatively low anomalous signal and occupancy and appears to be stabilized by crystal contacts (Table IV.2, Figure IV.1).

#### *IV.E.3. Modeling ligands to potential low affinity nickel sites on the NikR-DNA complex*



The higher resolution electron density maps of the NikR alone structure allowed us to model the protein ligands and potential water ligands to each of the excess nickel sites. While anomalous scattering indicates the approximate positions, low resolution electron density prevented modeling of ligands in the NikR-DNA structure. Therefore, we modeled low affinity nickel ion site types 1-3 on the NikR-DNA complex. These low affinity nickel sites are filled at least 2/3 of the time, or have occupancies greater than 66% (Table IV.2). In addition, site types 1-3 were found in both the NikR alone and NikR-DNA complex nickel anomalous maps at all potential sites, suggesting that these sites are the most preferred low affinity nickel sites.

To model these sites, the NikR-DNA complex structure with stoichiometric nickel was aligned to the NikR structure with excess nickel ions in COOT (22). The low affinity nickel ions (site types 1, 2, and 3) were modeled onto the NikR-DNA complex structure using the NikR structure with low affinity nickel ions as a guide. To ensure correct metal coordination, the amino acid side chains in the NikR-DNA complex responsible for metal ligation were reoriented to match the geometries observed in the NikR structure and water molecules seen in the NikR structure were saved in the NikR-DNA complex structure.

Water molecules refined in the crystal structure (Figure IV.2) were included in the minimization studies and molecular dynamics simulations. The structure was then minimized using 200 steps of steepest decent in CHARMM to remove bad contacts (23). After solvating the structure in a 57 Å radius water sphere, a total of 21,276 TIP3P water molecules (including the 32 crystallographic waters) were explicitly modeled in our system and the water boundary maintained using a spherical stochastic boundary potential (24). Finally, to allow the low affinity sites to rearrange before dynamics, all water molecules and protein residues within 5 Å of each low affinity nickel site were minimized using 500 steps of conjugate gradient minimization.

Molecular dynamics simulations were run using CHARMM to obtain a sampling of different conformations of each low affinity nickel site (23). To maintain the histidine ligands seen in the crystal structure, nickel-histidine distances were restrained with a strong force constant of  $100 \text{ kcal/mole} \cdot \text{\AA}^2$ , using the distances measured in the crystal structure as a guide (23). All protein atoms were held fixed except atoms in residues within  $5 \text{ \AA}$  of each low affinity site. In addition, water molecules and low affinity nickel ions underwent full molecular dynamics. The protein was first gently heated from 0 K to 300 K at a rate of 5 K/ps and the temperature maintained using a Nosé-Hoover heat bath (25). Dynamical simulations were then run at 300 K until the system was fully equilibrated. The total run time was 1.1 ns and structures were saved every 10 ps. All calculations in CHARMM were performed with an atom-based cutoff where the electrostatic interactions were brought to zero between 8 and  $12 \text{ \AA}$ , van der Waals interactions turned off at  $12 \text{ \AA}$ , and the non-bonded list cutoff at  $13 \text{ \AA}$ . In addition, the SHAKE command was used to restrain bonds involving hydrogen atoms near their equilibrium values (26).

#### **IV.F. Acknowledgements**

Dr. Eric Schreiter grew the crystals, collected X-ray data, and performed initial rounds of refinement on the structures. Portions of this research were carried out at Advanced Light Source (Contract No. DE-AC02-05CH11231) and the National Synchrotron Light Source at Brookhaven National Laboratory (Contract No. DE-AC02-98CH10886) was supported by the U.S. Department of Energy, Office of Science, and Office of Basic Energy Sciences.

#### IV.G. References

1. Bloom, S. L., and Zamble, D. B. (2004) Metal-Selective DNA-Binding Response of *Escherichia coli* NikR, *Biochemistry* 43, 10029-10038.
2. Chivers, P. T., and Sauer, R. T. (2002) NikR Repressor: High-Affinity Nickel Binding to the C-Terminal Domain Regulates Binding to Operator DNA, *Chem. Biol.* 9, 1141-1148.
3. Phillips, C. M., Schreiter, E. R., Guo, Y., Wang, S. C., Zamble, D. B., and Drennan, C. L. (2008) Structural Basis of the Metal Specificity for Nickel Regulatory Protein NikR, *Biochemistry* 47, 1938-1946.
4. Schreiter, E. R., Wang, S. C., Zamble, D. B., and Drennan, C. L. (2006) NikR-operator complex structure and the mechanism of repressor activation by metal ions, *Proc. Natl. Acad. Sci. U. S. A.* 103, 13676-13681.
5. Schreiter, E. R., Sintchak, M. D., Guo, Y., Chivers, P. T., Sauer, R. T., and Drennan, C. L. (2003) Crystal structure of nickel-responsive transcription factor NikR, *Nat. Struct. Bio.* 10, 794-799.
6. Wang, S. C., Dias, A. V., Bloom, S. L., and Zamble, D. B. (2004) Selectivity of Metal Binding and Metal-Induced Stability of *Escherichia coli* NikR, *Biochemistry* 43, 10018-10028.
7. Phillips, C. M., Nerenberg, P. S., Drennan, C. L., and Stultz, C. M. (2009) Physical Basis of Metal-Binding Specificity in *Escherichia coli* NikR, *J Am Chem Soc* 131, 10220-10228.
8. Leitch, S., Bradley, M. J., Rowe, J. L., Chivers, P. T., and Maroney, M. J. (2007) Nickel-Specific Response in the Transcriptional Regulator, *Escherichia coli* NikR, *J. Am. Chem. Soc.* 129, 5085-5095.
9. Chivers, P. T., and Tahirov, T. H. (2005) Structure of *Pyrococcus horikoshii* NikR: Nickel Sensing and Implications for the Regulation of DNA Recognition, *J. Mol. Bio.* 348, 597-607.
10. Wang, S. C., and Zamble, D. B. (2010) Potassium is Critical for the Ni(II)-Responsive DNA-Binding Activity of *Escherichia coli* NikR, *J. Am. Chem. Soc.* 132, 1506-1507.
11. Rulisek, L., and Vondrasek, J. (1998) Coordination geometries of selected transition metal ions ( $\text{Co}^{2+}$ ,  $\text{Ni}^{2+}$ ,  $\text{Cu}^{2+}$ ,  $\text{Zn}^{2+}$ ,  $\text{Cd}^{2+}$ , and  $\text{Hg}^{2+}$ ) in metalloproteins, *J. Inorg. Biochem.* 71, 115-127.

12. Phillips, C. M., and Drennan, C. L. (2008) Nickel Regulatory Transcription Factor, NikR., *Handbook of Metalloproteins*.
13. Abraham, L. O., Li, Y., and Zamble, D. B. (2006) The metal- and DNA-binding activities of *Helicobacter pylori* NikR, *J. Inorg. Biochem.* 100, 1005-1014.
14. Davis, G. S., Flannery, E. L., and Mobley, H. L. T. (2006) *Helicobacter pylori* HP1512 is a nickel-responsive NikR-regulated outer membrane protein, *Infect. Immun.* 74, 6811-6820.
15. Delany, I., Ieva, R., Soragni, A., Hilleringmann, M., Rappuoli, R., and Scarlato, V. (2005) In Vitro Analysis of Protein-Operator Interactions of the NikR and Fur Metal-Responsive Regulators of Coregulated Genes in *Helicobacter pylori*, *J. Bacteriol.* 187, 7703-7715.
16. Ernst, F. D., Kuipers, E. J., Heijens, A., Sarwari, R., Stoof, J., Penn, C. W., Kusters, J. G., and van Vliet, A. H. M. (2005) The Nickel-Responsive Regulator NikR controls Activation and Repression of Gene Transcription in *Helicobacter pylori*, *Infect. Immun.* 73, 7252-7258.
17. Ernst, F. D., Stoof, J., Horrevoets, W. M., Kuipers, E. J., Kusters, J. G., and van Vliet, A. H. M. (2006) NikR Mediates Nickel-Responsive Transcriptional Repression of the *Helicobacter pylori* Outer Membrane Proteins FecA3 (HP1400) and FrpB4 (HP1512), *Infect. Immun.* 74, 6821-6828.
18. Wolfram, L., Haas, E., and Bauerfeind, P. (2006) Nickel Represses the Synthesis of the Nickel Permease NixA of *Helicobacter pylori*, *J. Bacteriol.* 188, 1245-1250.
19. Otwinowski, Z., and Minor, W. (1997) Processing of X-ray Diffraction Data Collected in Oscillation Mode, *Methods Enzymol.* 276: *Macromolecular Crystallography, part A*, 307-326.
20. Brünger, A. T., Adams, P. D., Clore, G. M., DeLano, W. L., Gros, P., Grosse-Kunstleve, R. W., Jiang, J. S., Kuszewski, J., Nilges, M., Pannu, N. S., Read, R. J., Rice, L. M., Simonson, T., and Warren, G. L. (1998) Crystallography & NMR system (CNS): A new software suite for macromolecular structure determination, *Acta Crystallogr.* D54, 905-921.
21. Storoni, L. C., McCoy, A. J., and Read, R. J. (2004) Likelihood-enhanced fast rotation functions, *Acta Crystallogr.* D60, 432-438.
22. Emsley, P., and Cowtan, K. (2004) Coot: model-building tools for molecular graphics., *Acta Crystallogr.* D60, 2126-2132.

23. Brooks, B. R., Bruccoleri, R. E., Olafson, B. D., States, D. J., Swaminathan, S., and Karplus, M. (1983) CHARMM: A Program for Macromolecular Energy, Minimization, and Dynamics Calculations, *J Comput Chem* 4, 187-217.
24. Jorgensen, W. L., Chandrasekhar, J., Madura, J. D., Impey, R. W., and Klein, M. L. (1983) Comparison of Simple Potential Functions for Simulating Liquid Water, *J. Chem. Phys.* 79, 926-935.
25. Hoover, W. G. (1985) Canonical Dynamics - Equilibrium Phase-Space Distributions, *Physical Review A* 31, 1695-1697.
26. Ryckaert, J. P., Ciccotti, G., and Berendsen, H. J. C. (1977) Numerical-Integration of Cartesian Equations of Motion of a System with Constraints - Molecular-Dynamics of N-Alkanes, *J. Comput. Phys.* 23, 327-341.

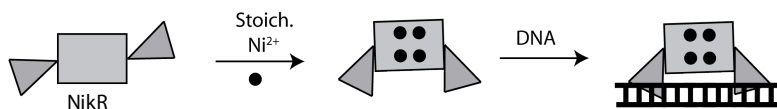


## Chapter V: Searching for the *nik* Operon

### Relating the mechanism for NikR binding DNA to current theories of how transcription factors find their DNA binding sites

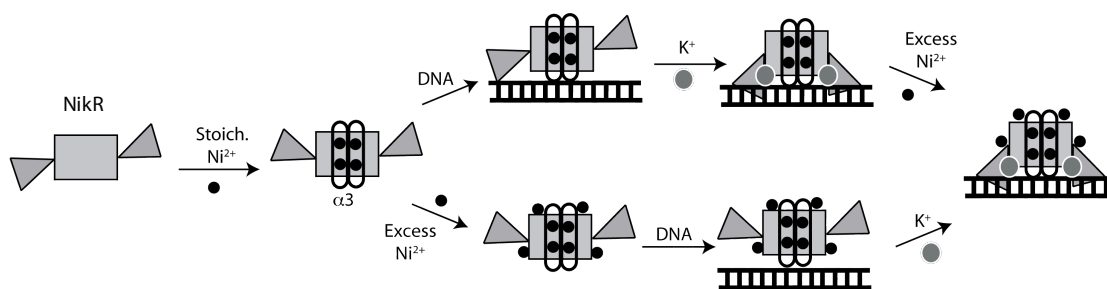
The work described in this thesis has examined the different types of metal binding sites of NikR and how metals binding at these sites influence DNA binding. A very simple and elegant model for ligand-mediated protein-DNA binding events is outlined in Scheme V.1. In this scheme, ligand (nickel) binding would induce a simple conformational change or an alteration in the electrostatic potential of the protein (NikR), causing the protein to bind DNA.

(Scheme V.1)



A conclusion that can be drawn from this thesis is that the involvement of metal ions in the regulation of NikR binding to DNA is considerably more complicated than the mechanism outlined in Scheme V.1. The mechanism we propose in Scheme V.2 arises from a variety of crystal structures of NikR that are now available (apo,  $\text{Ni}^{2+}$ -bound, DNA-bound, with excess nickel, and with various transition metals bound) in conjunction with biochemical and computational work carried out during this thesis and by others (*I-II*).

(Scheme V.2)



The work described in earlier chapters of this thesis supports a complex mechanism of NikR response to cellular metal ion concentrations (Scheme V.2). Crystal structures of various metals bound to the high affinity metal binding sites illustrate that when Ni<sup>2+</sup> binds at the high affinity site its main role is to order the central  $\alpha$ 3 helices and the preceding loops ( $\alpha$ 3 helices and associated loops are represented by open ovals in Scheme V.2) (8, 9). These ordered loops make non-specific hydrogen-bonding contacts with the DNA phosphate backbone, helping to localize NikR on DNA (Figure V.1) (10). The RHH domains, which remain flexible, can continuously sample the DNA sequence, while the non-specific hydrogen bonding interactions between the  $\alpha$ 3 helix/loop and DNA phosphate backbone stabilize a DNA-associated conformation (Figure V.1). Once the ribbons in the RHH domains make site-specific contacts with nucleotides in the major grooves at the DNA binding sites, the DNA-binding conformation of NikR is stabilized, creating the K<sup>+</sup> binding sites, which helps stabilize NikR in the DNA-binding orientation (Figures V.1c and V.2) (7, 10). Finally, any excess nickel ions in the cell can bind to the surface of the protein, enhancing NikR's affinity for the *nik* operon.

While our mechanism addresses the conformational changes that must occur for NikR to bind DNA, we have not yet considered how this mechanism relates to the “search” NikR would have to undertake to find the *nik* operon. It is interesting to consider how our mechanism shown in Scheme V.2 relates to current theories of how transcription factors find their binding sites on DNA. It was noted as early as 1970 by Riggs and coworkers, that transcription factors can find their binding sites extraordinarily fast *in vivo* (12). Specifically, it was documented that the LacI repressor could find its binding site on DNA at a rate of  $\sim 10^{10} \text{ M}^{-1}\text{s}^{-1}$ , faster than the rate limit of three-dimensional diffusion,  $10^8 \text{ M}^{-1}\text{s}^{-1}$  (12). To explain such a fast search rate it was proposed that the dimensionality of the search varied in time. It was hypothesized that this variation in search dimensionality could be achieved if the protein spent some amount of time performing a one-dimensional search by sliding along the DNA in addition to some amount of time diffusing around the cell in a three-dimensional search (12-15). This model has been supported with a variety of biochemical and single-molecule experiments (16-26).



**Figure V.1.** Crystal structures of full-length *E. coli* NikR. (a) Apo-NikR structure with disordered  $\alpha 3$  helices. (b)  $\text{Ni}^{2+}$ -bound NikR in an “open” conformation with ordered  $\alpha 3$  helices and a close-up of the high affinity nickel binding site. (c) NikR-DNA complex with NikR in a “down cis” conformation.  $\text{Ni}^{2+}$  and  $\text{K}^{+}$  in green and purple spheres, respectively. Surface representation is shown to illustrate contacts between NikR and DNA.

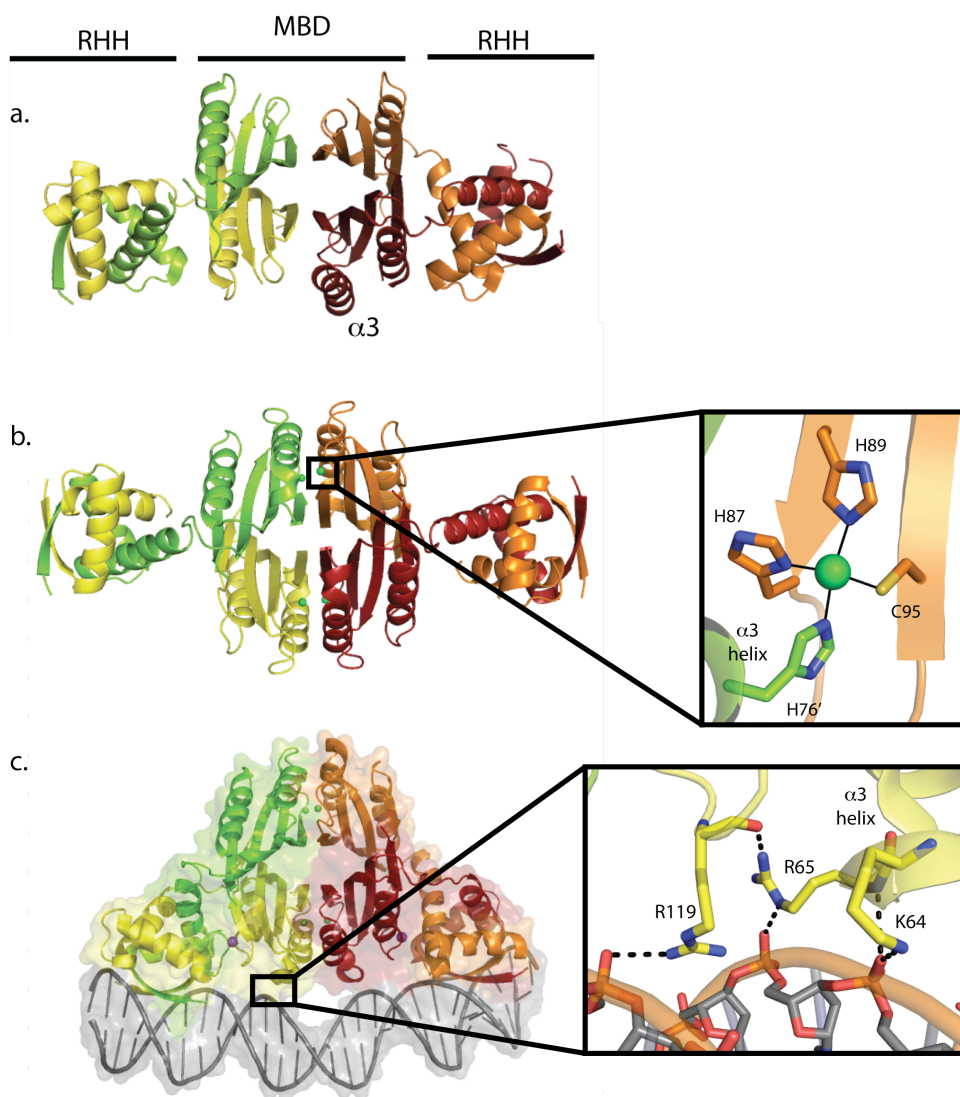
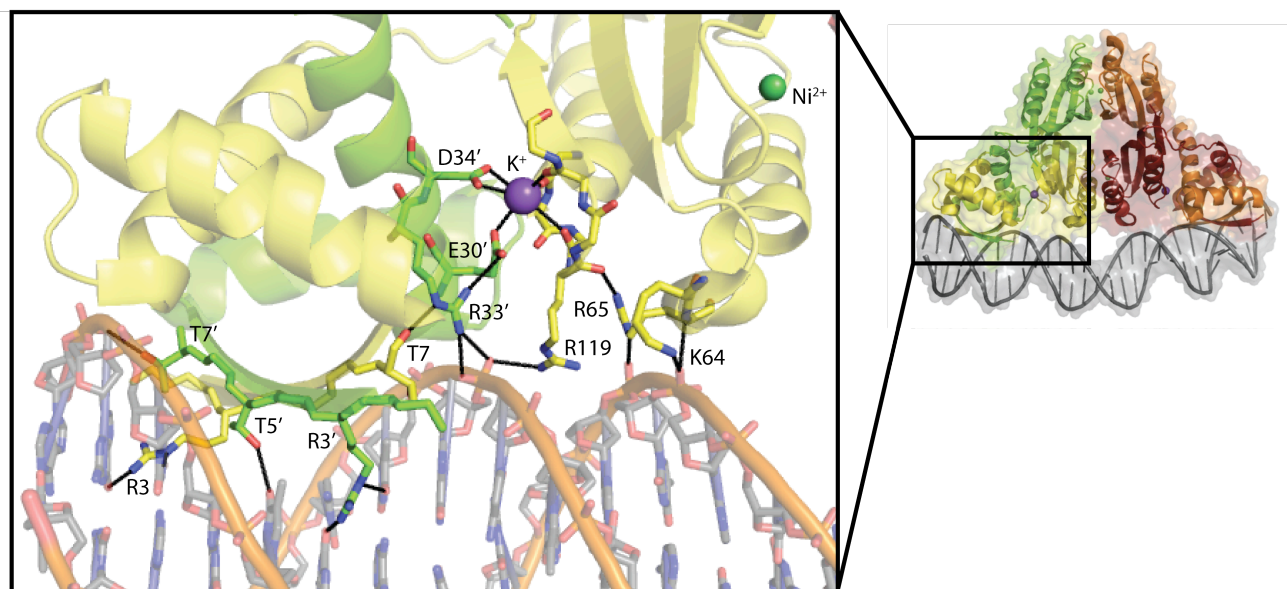


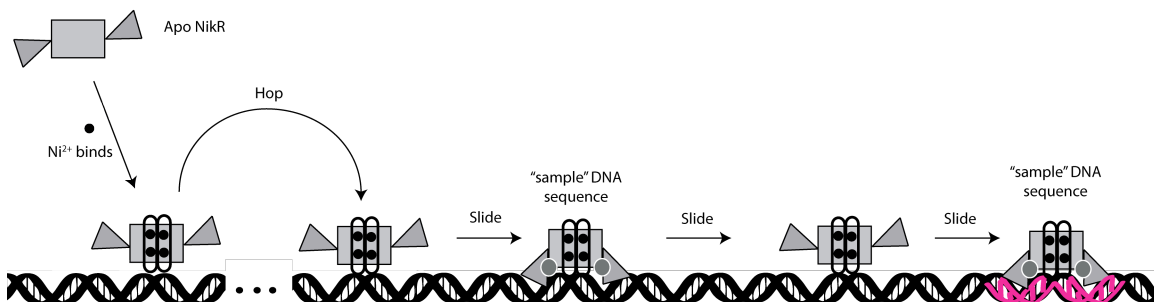
**Figure V.2.** The  $K^+$  site links an extended H-bonding network between the NikR and DNA. Specific contacts between NikR and DNA are shown on the left between the ribbons of the RHH domains and nucleotide residues in black lines. Important hydrogen bonding contacts requiring  $Ni^{2+}$ ,  $K^+$ , and the correct DNA binding site are shown in black lines. Important residues are shown in stick form and are labeled.



Recently it has been suggested that unless the sliding DNA-bound event incurs little energetic penalty (less than  $k_B T$  or about 0.6 kcal/mole at room temperature), then this sliding/diffusion mechanism would not be able to account for the biologically observed rates at which transcription factors can find their appropriate binding sites on DNA (27). Oftentimes, the known stable DNA binding conformation of a transcription factor involves insertion into the major or minor grooves and the formation of specific hydrogen bonds between the protein and DNA nucleotides. Such a DNA-bound form would likely have hydrogen bonds that needed to be broken if it were to attempt sliding along DNA, incurring an energetic penalty greater than  $k_B T$ . While a weak DNA affinity must be obtained to allow for sliding, a tight binding is crucial for forming a protein-DNA with strong affinity. A possible mechanism to account for the paradox of both weak and strong DNA binding is that the protein must have two distinct conformational states that can

bind DNA, but with different affinities (Figure V.3) (27). The weakly bound or “non-specific” conformation could be considered impartial to the DNA sequence it is binding, while the second, “specific” binding conformation is considerate of the surrounding DNA sequence. In this model the protein constantly transitions between the two DNA binding states, “sampling” the DNA sequence for binding sites as it slides along the DNA (Figure V.3).

**Figure V.3.** A proposed model for NikR’s search for the *nik* operon on DNA. The RHH domains are represented in grey triangles, MBD in rectangles,  $\alpha 3$  helices in open ovals, nickel ions in black circles, potassium ions in grey circles, and DNA in a black double-helix. The DNA site highlighted in pink represents the site just upstream of the *nik* operon that NikR specifically binds to in the cell to repress the transcription of *nikABCDE*, thus indicating the site where NikR has the highest affinity for DNA.



Our proposed mechanism in Scheme V.2 for NikR binding to DNA is consistent with these observations (27). When no metal is bound to NikR, the protein can freely diffuse with no or little affinity (less than  $\mu\text{M}$  affinity) for DNA (4). That is, the “search” for the DNA binding site does not begin until nickel ions bind at the high affinity sites. Once nickel ions bind to NikR and promote the ordering of the  $\alpha 3$  helices and loops preceding them, these loops have a weak affinity for DNA via hydrogen bonds with the phosphate backbone (Figure V.1c). These interactions create a “non-specific” binding conformation of NikR, whose localization on DNA is sequence-independent. This “non-specific”

conformation may allow for some “hopping” along the DNA, thereby continuing a 3D search (Figure V.3). The flexible RHH domains then continuously “sample” the DNA, creating a “specific” DNA binding conformation that considers the nucleotide sequence. Once the correct sequence is found, the “specific” binding conformation becomes very energetically favorable, stabilizing the protein at the DNA recognition site. The downward conformation of NikR is itself stabilized by the binding of  $K^+$  to the octahedral sites located at the RHH/MBD interface. Given the high concentration of  $K^+$  in the cell (~250 mM) (28), it is likely that  $K^+$  is bound at this site whenever the RHH domains are in a “down” conformation. While the  $K^+$  site may be occupied, it is likely not fully stable until the correct DNA binding site is found and the full hydrogen bonding network indicated in Figure V.2 is realized. Thus the site would not prohibit the RHH domains from remaining flexible until the correct site is found. The hydrogen bonding network organized by  $K^+$  ion binding does contain a number of fully conserved residues, including E30, D34, and R33, any of whose mutagenesis abrogates DNA binding (10, 29). Aspartic acid 34 coordinates the  $K^+$  ion in a bidentate fashion, while E34 has a monodentate coordination to  $K^+$  and the second oxygen participates in a hydrogen bonding network with conserved R33 (Figure V.2). Arginine 33 then makes hydrogen bonds to the DNA phosphate backbone and participates in ordering the hydrogen bonding networks contacting DNA in both the MBD and RHH regions (Figure V.2). Thus, not only is this potassium site well conserved, but it also appears to play a key role in organizing the complex hydrogen bonding network between the NikR protein and DNA.

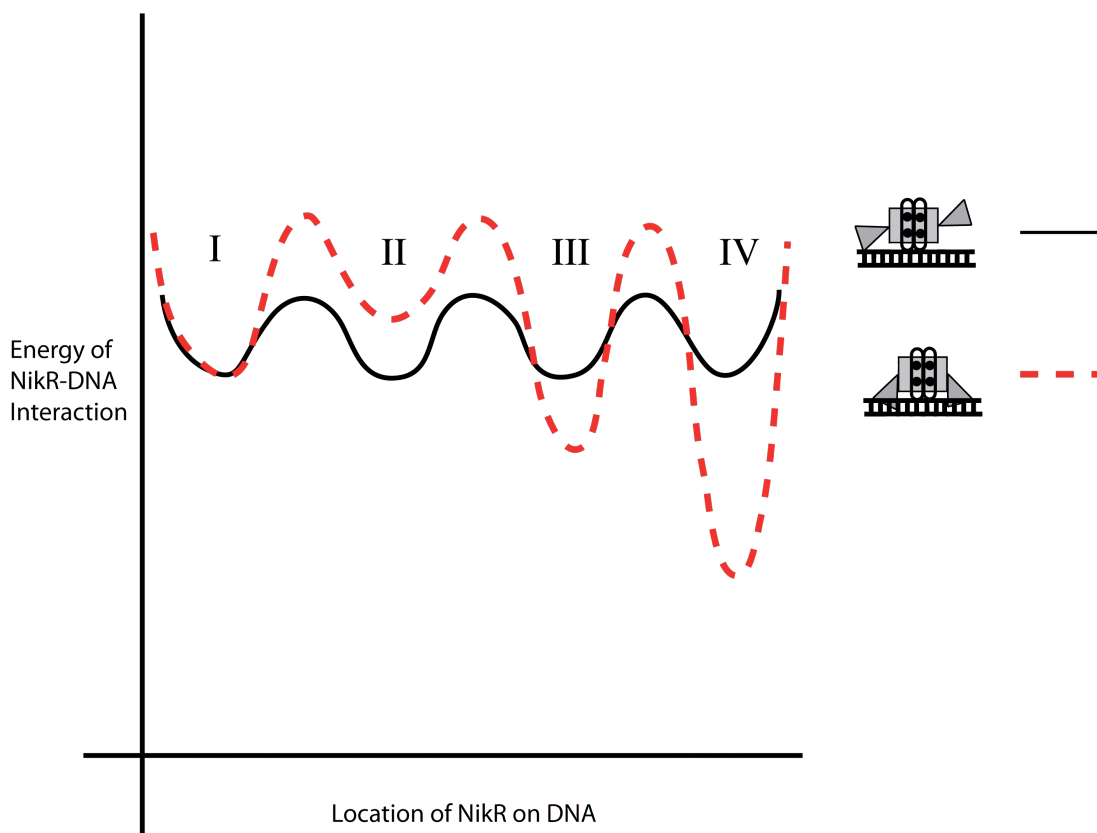
In light of these data, we can construct an energy landscape that describes the different states of NikR on DNA during the “sliding” phase (Figure V.3). The two energy landscapes illustrate the states sampled by the “non-specific” DNA binding conformation in which NikR is bound to the DNA using just the  $\alpha 3$  helices and associated loops (Figure V.4, solid line) and the “specific” DNA binding conformation in which RHH domains are in a down conformation, sampling the DNA sequence (Figure V.4, dashed red line). Four energy minima are shown for the two DNA binding modes and represent four different DNA sequences. The “non-specific” DNA binding mode is indifferent to the DNA sequence around it and thus experiences the same energy minima any time

NikR is associated to DNA. Site I represents a DNA sequence to which the RHH domains are “indifferent”, that is, the “specific” DNA binding conformation is no more energetically favorable than the “non-specific” DNA binding conformation (Figure V.4). Site II is a site where the “specific” DNA binding conformation of NikR has a weakened DNA affinity, possibly due to bad contacts with the base pairs. Site III represents a site on DNA with a similar but not identical DNA sequence to that at the actual binding site, thus imparting some favorable energy on the “specific” NikR conformation. Site IV represents the energy landscape at the correct DNA binding site, where the enthalpic gain of favorable interactions between the RHHs and DNA substantially outweighs the entropic penalty of locking the RHHs in the “specific” NikR conformation.

When considering the effect that excess nickel ions have on NikR’s affinity for DNA, we may consider an energy landscape where all minima are lower in energy. Our observation that a number of the low affinity nickel sites are present in both the NikR-DNA complex structure and NikR alone suggest that these sites could be filled before NikR finds its correct DNA binding site. If this is the case, then we could imagine excess nickel ions could stabilize both the “non-specific” and “specific” conformations of the NikR-DNA complex via favorable electrostatic interactions between the more positively charged NikR molecule and the negatively charged DNA.

The comparison presented in this chapter between our proposed mechanism and the sliding/diffusion theory regarding how transcription factors find their DNA binding sites is an example of how this work can be extrapolated to more general theories. Although the model we propose for NikR binding to DNA in Scheme V.2 may not include all caveats of the NikR system, work from this thesis has brought us much closer to understanding the variety of intricacies the small NikR protein holds.

**Figure V.4.** Putative energy landscape for NikR when bound to DNA in two different conformations. The two energy landscapes represent the “non-specific” (black solid line) and “specific” (red dashed line) DNA binding states of NikR. The four energy wells labeled I-IV illustrate potential different binding sites on the DNA. Site I would describe a site that has no preference for either the “specific” or “non-specific” NikR-DNA binding state. Site II is a site where the “specific” DNA binding conformation of NikR has a weakened DNA affinity, possibly due to bad contacts with the base pairs. Site III represents a site on DNA with a similar but not identical DNA sequence to that at the actual binding site, thus imparting some favorable energy on the “specific” NikR conformation. Site IV represents the energy landscape at the correct DNA binding site, where the enthalpic gain of favorable interactions between the RHHs and DNA substantially outweighs the entropic penalty of locking the RHHs in the “specific” NikR conformation.



## References

1. Bloom, S. L., and Zamble, D. B. (2004) Metal-Selective DNA-Binding Response of *Escherichia coli* NikR, *Biochemistry* 43, 10029-10038.
2. Chivers, P. T., and Sauer, R. T. (1999) NikR is a ribbon-helix-helix DNA-binding protein, *Protein Sci.* 8, 2494-2500.
3. Chivers, P. T., and Sauer, R. T. (2000) Regulation of high affinity nickel uptake in bacteria. Ni<sup>2+</sup>-Dependent interaction of NikR with wild-type and mutant operator sites, *J. Biol. Chem.* 275, 19735-19741.
4. Chivers, P. T., and Sauer, R. T. (2002) NikR Repressor: High-Affinity Nickel Binding to the C-Terminal Domain Regulates Binding to Operator DNA, *Chem. Biol.* 9, 1141-1148.
5. de Pina, K., Desjardin, V., Mandrand-Berthelot, M.-A., Giordano, G., and Wu, L. F. (1999) Isolation and Characterization of the *nikR* Gene Encoding a Nickel-Responsive Regulator in *Escherichia coli*, *J. Bacteriol.* 181, 670-674.
6. Leitch, S., Bradley, M. J., Rowe, J. L., Chivers, P. T., and Maroney, M. J. (2007) Nickel-Specific Response in the Transcriptional Regulator, *Escherichia coli* NikR, *J. Am. Chem. Soc.* 129, 5085-5095.
7. Phillips, C. M., Nerenberg, P. S., Drennan, C. L., and Stultz, C. M. (2009) Physical Basis of Metal-Binding Specificity in *Escherichia coli* NikR, *J Am Chem Soc* 131, 10220-10228.
8. Phillips, C. M., Schreiter, E. R., Guo, Y., Wang, S. C., Zamble, D. B., and Drennan, C. L. (2008) Structural Basis of the Metal Specificity for Nickel Regulatory Protein NikR, *Biochemistry* 47, 1938-1946.
9. Schreiter, E. R., Sintchak, M. D., Guo, Y., Chivers, P. T., Sauer, R. T., and Drennan, C. L. (2003) Crystal structure of nickel-responsive transcription factor NikR, *Nat. Struct. Bio.* 10, 794-799.
10. Schreiter, E. R., Wang, S. C., Zamble, D. B., and Drennan, C. L. (2006) NikR-operator complex structure and the mechanism of repressor activation by metal ions, *Proc. Natl. Acad. Sci. U. S. A.* 103, 13676-13681.
11. Wang, S. C., Dias, A. V., Bloom, S. L., and Zamble, D. B. (2004) Selectivity of Metal Binding and Metal-Induced Stability of *Escherichia coli* NikR, *Biochemistry* 43, 10018-10028.
12. Riggs, A. D., Bourgeois, S., and Cohn, M. (1970) Lac Repressor-Operator Interaction .3. Kinetic Studies, *J. Mol. Bio.* 53, 401-&.

13. Berg, O. G., and Blomberg, C. (1976) Association Kinetics with Coupled Diffusional Flows - Special Application to Lac Repressor-Operator System, *Biophys Chem* 4, 367-381.
14. Berg, O. G., Winter, R. B., and Vonhippel, P. H. (1981) Diffusion-Driven Mechanisms of Protein Translocation on Nucleic-Acids .1. Models and Theory, *Biochemistry* 20, 6929-6948.
15. Richter, P. H., and Eigen, M. (1974) Diffusion Controlled Reaction-Rates in Spheroidal Geometry - Application to Repressor-Operator Association and Membrane-Bound Enzymes, *Biophys Chem* 2, 255-263.
16. Blainey, P. C., van Oijent, A. M., Banerjee, A., Verdine, G. L., and Xie, X. S. (2006) A base-excision DNA-repair protein finds intrahelical lesion bases by fast sliding in contact with DNA, *Proc. Natl. Acad. Sci. U. S. A.* 103, 5752-5757.
17. Elf, J., Li, G. W., and Xie, X. S. (2007) Probing transcription factor dynamics at the single-molecule level in a living cell, *Science* 316, 1191-1194.
18. Gorman, J., Chowdhury, A., Surtees, J. A., Shimada, J., Reichman, D. R., Alani, E., and Greene, E. C. (2007) Dynamic basis for one-dimensional DNA scanning by the mismatch repair complex Msh2-Msh6, *Mol Cell* 28, 359-370.
19. Gorman, J., and Greene, E. C. (2008) Visualizing one-dimensional diffusion of proteins along DNA, *Nat Struct Mol Biol* 15, 768-774.
20. Gowers, D. M., Wilson, G. G., and Halford, S. E. (2005) Measurement of the contributions of 1D and 3D pathways to the translocation of a protein along DNA, *Proc. Natl. Acad. Sci. U. S. A.* 102, 15883-15888.
21. Kim, J. G., Takeda, Y., Matthews, B. W., and Anderson, W. F. (1987) Kinetic-Studies on Cro Repressor Operator DNA Interaction, *J. Mol. Bio.* 196, 149-158.
22. McKinney, K., Mattia, M., Gottifredi, V., and Prives, C. (2004) p53 linear diffusion along DNA requires its C terminus, *Mol Cell* 16, 413-424.
23. Winter, R. B., Berg, O. G., and Vonhippel, P. H. (1981) Diffusion-Driven Mechanisms of Protein Translocation on Nucleic-Acids .3. The Escherichia-Coli-Lac Repressor-Operator Interaction - Kinetic Measurements and Conclusions, *Biochemistry* 20, 6961-6977.
24. Graneli, A., Yeykal, C. C., Robertson, R. B., and Greene, E. C. (2006) Long-distance lateral diffusion of human Rad51 on double-stranded DNA, *Proc. Natl. Acad. Sci. U. S. A.* 103, 1221-1226.
25. Wang, Y. M., Austin, R. H., and Cox, E. C. (2006) Single molecule measurements of repressor protein 1D diffusion on DNA, *Phys. Rev. Lett.* 97, -.



26. Tafvizi, A., Huang, F., Leith, J. S., Fersht, A. R., Mirny, L. A., and van Oijen, A. M. (2008) Tumor suppressor p53 slides on DNA with low friction and high stability, *Biophys. J.* 95, L1-L3.
27. Slutsky, M., and Mirny, L. A. (2004) Kinetics of protein-DNA interaction: Facilitated target location in sequence-dependent potential, *Biophys. J.* 87, 4021-4035.
28. Epstein, W., and Schultz, S. G. (1966) Cation transport in *Escherichia coli*. VI. K exchange, *J Gen Physiol* 49, 469-481.
29. Wang, S. C., and Zamble, D. B. (2010) Potassium is Critical for the Ni(II)-Responsive DNA-Binding Activity of *Escherichia coli* NikR, *J. Am. Chem. Soc.* 132, 1506-1507.



DEPARTMENT OF CHEMISTRY  
MASSACHUSETTS INSTITUTE OF TECHNOLOGY  
77 MASSACHUSETTS AVE. BLDG. 68-688D  
CAMBRIDGE, MA 02139  
(617) 258-7021  
EMAIL: CMP\_CHEM@MIT.EDU

## CHRISTINE MARIE PHILLIPS

---

### EDUCATION

---

2004 – Present	<b>Massachusetts Institute of Technology</b> <i>Ph.D. Candidate, Biological Chemistry</i>	Cambridge, MA
2000 – 2004	<b>Vassar College</b> <i>B.A. with honors, Chemistry and Mathematics</i>	Poughkeepsie, NY

### RESEARCH EXPERIENCE

---

2004 – Present	<b>Massachusetts Institute of Technology</b> Graduate Research Assistant, Department of Chemistry <i>Advisors: Catherine L. Drennan, Ph.D. and Collin M. Stultz, M.D., Ph.D.</i>	Cambridge, MA
----------------	--	---------------

- Thesis work centers on structural and computational analysis of the nickel transcription factor NikR. Solved a number of crystal structures of *E. coli* NikR to elucidate the DNA binding mechanism for NikR and improve our understanding of how NikR functions in the cell. From structures of different metal-bound forms of *E. coli* NikR we have proposed a unique role for the  $\alpha 3$  helix of NikR in DNA binding. Using a combined molecular mechanics Poisson-Boltzmann approach illustrated that the preferred metal at the second metal binding site in NikR is  $K^+$ , not  $Ni^{2+}$ . Now we are examining the importance and location of the excess nickel binding sites on the NikR protein using a combined crystallographic and computational approach. General laboratory skills included: protein expression and purification, crystallization, crystal diffraction and data collection, data reduction and analysis, and structure determination using molecular replacement. In addition, I have gained a level of expertise with a number of computer programs for crystallographic analysis: MOSFLM, Scala, HKL package, CCP4, COOT, PyMOL, Xtalview; and for computational studies: MATLAB, Charmm, and Delphi.

2000 – 2004	<b>Vassar College</b> Undergraduate Research Assistant, Department of Chemistry <i>Advisor: Miriam Rossi, Ph.D.</i>	Poughkeepsie, NY
-------------	---	------------------

- Studied small biologically active (mostly inorganic) compounds using crystallography, including a number of possible anti-cancer agents. In addition to crystallography, I worked on developing a set of rules to describe the favorable conformation of different ligands when bound to tin. To support the structural work, I also utilized computational programs to assess the ideal conformations of given compounds of interest.

## PUBLICATIONS

---

- Phillips, C. M.**, Nerenberg, P. S., Drennan, C. L., Stultz, C. M. (2009) The Physical Basis for Metal Selectivity in *Escherichia coli* NikR. *JACS*, 131, 10220-10228.
- Phillips, C. M.** and Drennan, C. L. (2008) Nickel Regulatory Transcription Factor, NikR. *Handbook of Metalloproteins*.
- Bohon, J., Jennings, L. D., **Phillips, C. M.**, Licht, S., Chance, M. R. (2008) The Conformation of Functional Domains in the ClpA Hexamer : A Synchrotron Footprinting Study. *Structure* 16, 1157-1165.
- Phillips, C. M.**, Schreiter, E. R., Guo, Y., Wang, S. C., Zamble, D. B., Drennan, C. L. (2008) Structural Basis of the Metal Specificity for Nickel Regulatory Protein NikR. *Biochemistry* 47 (7), 1938-1946.
- Caruso, F., Pettinari, C., Marchetti, F., Natanti, P., **Phillips, C.**, Tanski, J., Rossi, M. (2007) Synthesis, Molecular Structure (X-ray and DFT), and Solution Behavior of Titanium 4-Acyl-5-pyrazolonates. Correlations with Related Antitumor  $\beta$ -Diketonato Derivatives. *Inorganic Chemistry* 46, 7553-7560.
- Pettinari, C., Caruso, F., Zaffaroni, N., Villa, R., Marchetti, F., Pettinari, R., **Phillips, C.**, Tanski, J., Rossi, M. (2006) Synthesis, Spectroscopy (IR, multinuclear NMR, ESI-MS), Diffraction, Density Functional Study and in vitro Antiproliferative Activity of Pyrazole-beta-diketone Dihalotin(IV) Compounds on 5 Melanoma Cell Lines. *Journal of Inorganic Biochemistry* 100, 58-69.
- Pettinari, C., Marchetti, F., Pettinari, R., Cingolani, A., Rivarola, E., **Phillips, C.**, Tanski, J., Rossi, M., Caruso, F. (2004) Tin(II) and Lead(II) 4-Acyl-5-pyrazolonates: Synthesis, Spectroscopy (IR,  $^1\text{H}$ ,  $^{13}\text{C}$ , and  $^{119}\text{Sn}$  NMR,  $^{119}\text{Sn}$  Mossbauer and ESI-MS) and X-ray Structural Characterization. *European Journal of Inorganic Chemistry* 17, 3484-3497.

## SELECTED PRESENTATIONS

---

- 2009 *Speaker*, MIT Biology Department Symposium, "Metal Preference in the Nickel Regulatory Protein NikR".
- 2009 *Poster*, Biophysical Society 53<sup>rd</sup> Annual Meeting, "The Physical Basis of Metal Specificity in *E. coli* NikR".
- 2009 *Invited Speaker*, GRC: Graduate Research Seminar in Bioinorganic Chemistry, "Metal Preference at the Second Metal Binding Site of *E. coli* NikR".
- 2009 *Poster*, GRC: Metals in Biology, "The Physical Basis of Metal Specificity in *E. coli* NikR".
- 2008 *Speaker*, MIT Interdepartmental Seminar for Biology, Biological Chemistry, and Systems Biology, "Studies of the Second Metal Binding Sites of NikR".
- 2008 *Poster*, Merck-MIT Symposium, "Metal Preference at the Second Metal Binding Site of *E. coli* NikR".

- 2008 *Speaker*, GRC: Graduate Research Seminar in Bioinorganic Chemistry, "Structural Basis of Metal Specificity for Nickel Regulatory Protein NikR"
- 2007 *Speaker*, MIT Interdepartmental Seminar for Biology, Biological Chemistry, and Systems Biology, "How binding of different transition metals affects the structure of NikR: Elucidating a mechanism for DNA binding"
- 2007 *Speaker*, American Chemical Society 234<sup>th</sup> National Meeting, "How binding of different transition metals affects the structure of NikR"
- 2006 *Poster*, The 25<sup>th</sup> Summer Symposium in Molecular Biology at Penn State: Frontiers in Metallobiochemistry, "Implications of Metal Coordination on NikR Specificity: An Update on the Zn(II)-bound NikR Structure"

## HONORS AND AWARDS

---

- 2009 Elected chair of 2011 Bioinorganic Gordon Graduate Research Seminar, Ventura, CA
- 2008 Biology Department Poster Prize, Massachusetts Institute of Technology
- 2004 Sigma Xi, Vassar College Chapter
- 2004 Chemistry Department Award to Graduating Senior, Vassar College
- 2004 ACS College Recognition Award, Vassar College
- 2003 3<sup>rd</sup> Place at ACS Poster Session, Mid-Hudson Chapter
- 2003 HHMI Summer Research Fellowship, Vassar College
- 2002 URSI Summer Research Fellowship, Vassar College

## TEACHING AND MENTORING EXPERIENCE

---

2005 – Present **Massachusetts Institute of Technology** Cambridge, MA  
*Undergraduate Research Mentor*

- Mentored a total of 6 undergraduates during either a 10 week span over the summer or throughout the school year. The undergraduates worked on independent projects derived from my main research goals. Taught a number of laboratory skills including: protein crystallization, crystallographic data collection and processing, protein expression and purification. Assisted the students in organizing a poster and/or presentation to summarize their research.

2008 **Massachusetts Institute of Technology** Cambridge, MA

*6.582, Intro to Molecular Simulations, Guest Lecturer*

- Taught a lecture in this graduate course entitled: "Structure Determination by X-ray Crystallography". A brief introduction to crystallography and how to evaluate a published crystal structure.

- 2008                    **Massachusetts Institute of Technology**    Cambridge, MA  
*5.111, Principles of Chemical Science, HHMI Teaching Assistant*
- Taught recitations twice a week to approximately 15 students; prepared materials and lecture for each recitation using an interactive technology to get the students more involved in recitation; graded problem sets and exams.
- 2007                    **Massachusetts Institute of Technology**    Cambridge, MA  
*HHMI-MIT Mentoring Training Course*
- Enrolled in a summer-long mentoring course offered through HHMI and MIT to learn effective mentoring strategies and discuss issues that may arise during a mentorship.
- 2005                    **Massachusetts Institute of Technology**    Cambridge, MA  
*5.111 and 5.112, Principles of Chemical Science, Head Teaching Assistant*
- Organized recitations; wrote answers to homework assignments; graded exams; assisted in making the classes run smoothly; maintained class websites.
- 2004                    **Massachusetts Institute of Technology**    Cambridge, MA  
*5.32, Intermediate Chemical Experimentation, Teaching Assistant*
- Taught biochemistry portion of the laboratory course for chemistry majors; gave opening lectures; assisted students with the experiments; prepared and graded quizzes; and administered final oral examinations.
- 2004                    **Massachusetts Institute of Technology**    Cambridge, MA  
*5.111 Principles of Chemical Science, Teaching Assistant*
- Taught recitations twice a week to approximately 25 students; prepared materials and lecture for each recitation; graded problem sets and exams.
- 2004                    **Poughkeepsie High School**                    Poughkeepsie, NY  
*Physical Science, Teaching Assistant*
- Funded through an HHMI grant associated with Vassar College, I spent a semester at the local public high school twice a week in a 9<sup>th</sup> grade Physical Science class. Designed, organized, and executed three class lectures involving hands-on science to help introduce and illuminate a scientific concept.
- 2003-2004            **Vassar College**                                    Poughkeepsie, NY  
*Organic Chemistry, Lab Teaching Assistant*
- Attended all labs and helped set up for each experiment. Assisted students with questions during the lab period. Graded lab reports.